Delft University of Technology

# Application of Sophisticated Models to Conventional Diffusion-Weighted MRI Data

Arkesteijn, Joor

**DOI**
10.4233/uuid:e0116582-fdd0-451f-a81f-c97980116328

**Publication date**
2018

**Document Version**
Final published version

**Citation (APA)**
Arkesteijn, J. (2018). *Application of Sophisticated Models to Conventional Diffusion-Weighted MRI Data*. [Dissertation (TU Delft), Delft University of Technology]. https://doi.org/10.4233/uuid:e0116582-fdd0-451f-a81f-c97980116328

# APPLICATION OF SOPHISTICATED MODELS TO CONVENTIONAL DIFFUSION-WEIGHTED MRI DATA

# APPLICATION OF SOPHISTICATED MODELS TO CONVENTIONAL DIFFUSION-WEIGHTED MRI DATA

## Proefschrift

ter verkrijging van de graad van doctor
aan de Technische Universiteit Delft,
op gezag van de Rector Magnificus Prof. dr. ir. T.H.J.J. van der Hagen,
voorzitter van het College voor Promoties,
in het openbaar te verdedigen op vrijdag 16 februari 2018 om 15:00 uur

door

**Georgius Augustinus Maria ARKESTEIJN**

natuurkundig ingenieur
geboren te Pijnacker.

Dit proefschrift is goedgekeurd door de

promotors: Prof. dr. ir. L.J. van Vliet en Prof. dr. W.J. Niessen
copromotor: Dr. F.M. Vos

Samenstelling promotiecommissie:

| | |
|---|---|
| Rector Magnificus, | voorzitter |
| Prof. dr. ir. L.J. van Vliet, | Technische Universiteit Delft |
| Prof. dr. W.J. Niessen, | Erasmus MC, Rotterdam |
| Dr. F.M. Vos, | Technische Universiteit Delft |
| | |
| *Onafhankelijke leden:* | |
| Dr. E. Farrher, | Forschungszentrum Jülich |
| Prof. dr. ir. F. Maes, | KU Leuven |
| Prof. dr. L. Reneman, | Universiteit van Amsterdam |
| Prof. dr. B. Rieger, | Technische Universiteit Delft |
| Prof. dr. A.M. Vossepoel, | Erasmus MC, Rotterdam, reservelid |

The work in this thesis was conducted at the Quantitative Imaging Group (QI), Faculty of Applied Sciences, Delft University of Technology and at the Biomedical Imaging Group Rotterdam (BIGR), Departments of Radiology and Medical Informatics, Erasmus Medical Center, Rotterdam. This work is part of the research programme Population Imaging Genetics (ImaGene) which is (partly) financed by the Netherlands Organisation for Scientific Research (NWO). This work was carried out in the ASCI graduate school, ASCI dissertation series number 385.

*Printed by:* GVO Drukkers & Vormgevers

*Front & Back:* Image of a downsampled brain with Gaussian noise on background.

ISBN 978-94-6332-315-4

An electronic version of this dissertation is available at
http://repository.tudelft.nl/.

# CONTENTS

# SUMMARY

The brain's white matter mainly consists of (myelinated) axons that connect different parts of the brain. Diffusion-weighted MRI (DW-MRI) is a technique that is particularly suited to image this white matter. The MRI signal in DW-MRI is sensitized to diffusion of water in the microstructure by introducing strong bipolar gradients in the MRI pulse sequence. By measuring the diffusion in different directions, the local diffusion profile of water molecules is obtained which reflects microstructural characteristics of the white matter.

The focus of this thesis is on the analysis of *conventional* DW-MRI data acquired in the context of the Rotterdam Scan Study. This is a prospective population-based cohort study with more than 10.000 participants to investigate causes of neurological disease in elderly people. Conventional DW-MRI is defined as diffusion data acquired with a single diffusion-weighting factor and a small number of diffusion-sensitizing gradient orientations. The objectives of this thesis are (1) to enhance our insight in the relation between tissue structure and the DW-MRI signal from conventional DW-MRI sequences, and (2) to develop methods to quantify diffusion properties in the brain as accurately and precisely as possible based on conventional DW-MRI data.

To gain insight into the relation between tissue structure and the DW-MRI signal, simulated DW-MRI signals based on Monte Carlo simulations of spins between randomly packed cylinders are compared to experimentally acquired data from a hardware phantom. The hardware phantom consists of solid fibers and acts as a model for the extra-axonal diffusion. The simulated DW-MRI signal is in good agreement with the experimentally acquired data. Furthermore, simulations show that the DW-MRI signal from spins between randomly packed cylinders is relatively independent of the cylinder diameter for $b$-values up to 1500 s/mm$^2$. For $b$-values higher than 1500 s/mm$^2$, substrates with a smaller cylinder diameter yield a larger attenuation of the diffusion-weighted signal (chapter 2).

Conventional DW-MRI data is commonly analyzed with a technique known as diffusion tensor imaging. Here, the water diffusion profile is modelled by a 3D Gaussian diffusion profile. However, in white matter structures in close proximity to the cerebrospinal fluid (CSF) the use of the single diffusion tensor model is inappropriate. A novel framework is introduced to analyze white matter structures adjacent to the CSF. In this framework a constrained two-compartment diffusion model is fit to the data in which the CSF is explicitly modeled with a free water diffusion compartment. The proposed diffusion statistics are shown to be relatively independent of partial volume effects with CSF and are applied to study ageing in the fornix, a small white matter structure bordering the CSF (chapter 3).

A significant part of the white matter constitutes of 'crossing fibers', whereby two or more white matter tracts contribute to the DW-MRI signal in a voxel. The single diffusion tensor model cannot adequately describe the data in such voxels. To solve this issue a fiber orientation atlas and a model complexity atlas were used to analyze conventional DW-MRI data with a simple crossing fibers model, namely the ball-and-sticks model. It is shown that the application of a fiber orientation atlas and a model complexity atlas can significantly improve the reproducibility and sensitivity of diffusion statistics in a voxel-based analysis (chapter 4).

Finally, a framework is proposed that aims to specifically improve the analysis of longitudinal DW-MRI data. In this framework the ball-and-sticks model is fit simultaneously to multiple scans of the same subject. The orientations of the sticks are constrained to be the same over different scans, while all other parameters are estimated separately for each scan. The use of this framework is shown to increase the precision of estimated ball-and-sticks model parameters in longitudinal DW-MRI studies (chapter 5).

In conclusion, this thesis describes frameworks to enhance the accuracy or precision of estimated diffusion properties of the white matter by applying sophisticated diffusion models to conventional DW-MRI data. We anticipate that many diffusion MRI studies may benefit from the work described in this thesis.

# SAMENVATTING

De witte stof in de hersenen bestaat voornamelijk uit (gemyeliniseerde) axonen die de verschillende delen van de hersenen met elkaar verbinden. Diffusie-gewogen MRI (DW-MRI) is een techniek die bijzonder geschikt is om deze witte stof te bestuderen. Het MRI-signaal in DW-MRI is gevoelig voor diffusie van water in de microstructuur door de introductie van sterke bipolaire gradiënten in de MRI-pulssequentie. Door de diffusie in verschillende richtingen te meten, kan het lokale diffusieprofiel van watermoleculen worden bepaald. Dit diffusieprofiel geeft inzicht in de microstructurele kenmerken van de witte stof.

De focus van dit proefschrift ligt op de analyse van *conventionele* DW-MRI data die wordt verkregen in het kader van de Rotterdam Scan Studie. Dit is een langlopend bevolkingsonderzoek met meer dan 10.000 deelnemers om de oorzaken van neurologische aandoeningen bij ouderen te onderzoeken. Conventionele DW-MRI data wordt gedefinieerd als data verkregen met een enkele diffusie-weegfactor en een klein aantal diffusie-gradiëntoriëntaties. De doelstellingen van dit proefschrift zijn (1) om het inzicht in de relatie tussen de microstructuur van de witte stof en het DW-MRI signaal uit conventionele DW-MRI-sequenties te vergroten, en (2) om methodes te ontwikkelen om de diffusie-eigenschappen in de hersenen zo accuraat en precies mogelijk te kwantificeren op basis van conventionele DW-MRI data.

Om inzicht te krijgen in de relatie tussen de microstructuur van de witte stof en het DW-MRI signaal, worden gesimuleerde DW-MRI signalen op basis van Monte Carlo-simulaties van spins tussen willekeurig-gepositioneerde cilinders vergeleken met experimenteel verkregen data van een hardware fantoom. Het hardware fantoom bestaat uit solide fibers en fungeert als een model voor de extra-axonale diffusie. Het gesimuleerde DW-MRI signaal is in goede overeenstemming met de experimenteel verkregen data. Bovendien laten simulaties zien dat het DW-MRI signaal van spins tussen willekeurig-gepositioneerde cilinders relatief onafhankelijk is van de cilinderdiameter voor $b$-waarden tot 1500 s/mm$^2$. Voor $b$-waarden hoger dan 1500 s/mm$^2$, geven substraten met een kleinere cilinderdiameter een grotere verzwakking van het DW-MRI signaal (hoofdstuk 2).

Conventionele DW-MRI data wordt vaak geanalyseerd met een techniek die bekend staat als diffusie tensor imaging. Deze techniek modelleert het diffusieprofiel van water met een enkele 3D Gaussische verdeling. In witte stof nabij het hersenvocht, ook wel cerebrospinale vloeistof (CSF) genoemd, is het gebruik van dit enkele diffusietensormodel echter niet geschikt. Een nieuwe methode wordt geïntroduceerd om witte stofstructuren naast de CSF te analyseren. Hierbij wordt gebruik gemaakt van een diffusiemodel met twee compartimenten waarin de bijdrage van de CSF aan het DW-MRI signaal expliciet gemodelleerd wordt. De voorgestelde diffusiestatistieken blijken relatief onafhankelijk te zijn van signaalverstoringen door de CSF en worden toegepast om veroudering in de fornix te bestuderen, een kleine witte stofstructuur die grenst aan de CSF (hoofdstuk 3).

Een aanzienlijk deel van de witte stof bestaat uit 'kruisende fibers', waarbij twee of meer witte stofbanen bijdragen aan het DW-MRI signaal in een voxel. Het enkele diffusietensormodel kan het diffusie-gewogen signaal in dergelijke voxels niet adequaat beschrijven. Om dit probleem op te lossen worden een fiberoriëntatieatlas en een modelcomplexiteitsatlas gebruikt om conventionele DW-MRI data te analyseren met een eenvoudig kruisende fibersmodel, namelijk het *ball-and-sticks* model. Experimenten laten zien dat de toepassing van een fiberoriëntatieatlas en een modelcomplexiteitsatlas de reproduceerbaarheid en gevoeligheid van diffusiestatistieken in een voxel-gebaseerde analyse aanzienlijk kan verbeteren (hoofdstuk 4).

Ten slotte wordt een methode voorgesteld die specifiek gericht is op het verbeteren van de analyse van longitudinale DW-MRI data. In dit kader wordt het *ball-and-sticks* model simultaan geschat van meerdere scans van dezelfde persoon. De oriëntaties van de *sticks* zijn hierbij gelijk over verschillende scans, terwijl alle andere diffusieparameters voor elke scan afzonderlijk worden geschat. Het gebruik van deze methode verhoogt de nauwkeurigheid van geschatte *ball-and-sticks* parameters in longitudinale DW-MRI onderzoeken (hoofdstuk 5).

Concluderend beschrijft dit proefschrift methodes om de nauwkeurigheid of precisie van geschatte diffusie-eigenschappen van de witte stof te verbeteren door verfijnde diffusiemodellen toe te passen op conventionele DW-MRI data. We verwachten dat veel DW-MRI onderzoeken kunnen profiteren van het werk dat in dit proefschrift wordt beschreven.

# 1

# INTRODUCTION

The brain consists of 100 billion neurons that communicate through up to 100 trillion connections [1]. As such it is the most complex organ in the human body.

## 1.1. THE BRAIN

The fundamental building block of the brain are the neurons. Neurons are specialized cells in the nervous systems that receive, process and transmit electric signals to other neurons. A neuron is typically constituted of three parts: a cell body (soma), dendrites, and an axon (figure 1.1A). Dendrites are short extensions of the cell body that are stimulated by impulses from other cells. Axons are relatively long threadlike extensions, which conduct electrical impulses away from the cell body. Axons are arranged in bundles called tracts (in the central nervous system) or nerves (in the peripheral nervous system), and can be up to 1 meter long. Figure 1.1B shows an anatomical drawing of a human brain. The wrinkled and folded outer layer of the brain is known as the cerebral cortex. The cerebral cortex is a thin layer up to 5 mm thick and consists of tightly-packed neurons and glial cells (non-neuronal cells), also known as grey matter (GM).

The inside of the brain primarily consists of bundles of (myelinated) axons: the white matter (WM). Typical cross-sectional images of a white matter bundle (a rat's spinal cord) are shown in figure 1.2. It can be seen that axon diameters in the white matter vary widely. For instance, in the human corpus callosum, a white matter structure connecting the left and right hemisphere, axon diameters range between 0.1 µm to 2 µm [2].

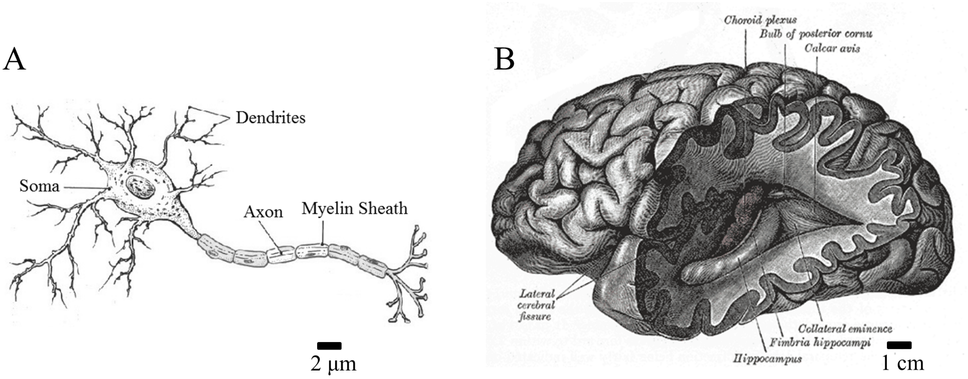

Figure 1.1: A) Illustration of a neuron [3]. B) Drawing of the cerebral cortex of a human brain with the white matter partially exposed [4]

## 1.2. SHORT HISTORY OF NEURO-IMAGING

Until the 19th century, the brain was primarily studied by dissections. Studies of the brain became more sophisticated after the invention of the microscope and subsequently the development of staining techniques in the 19th century. Even nowadays, such ex-vivo approaches are still widely used.

The first non-invasive technique to image the brain was developed by Angelo Mosso

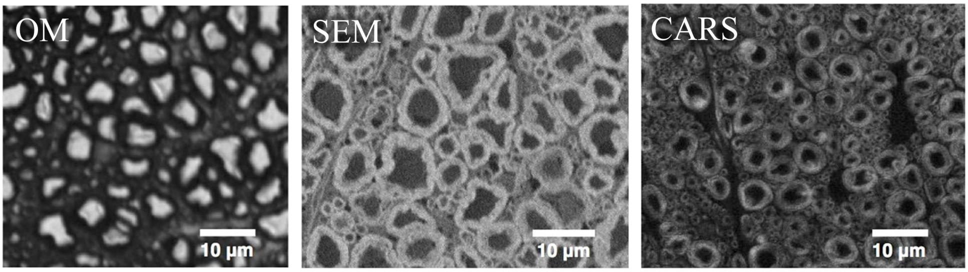

Figure 1.2: Optical microscopy (OM), scanning electron microscopy (SEM) and coherent anti-Stokes Raman scattering (CARS) microscopy images of the spinal cord of a rat [5].

at the end of the 19th century, known as the ’human circulation balance’ [6]. In the early 20th century, X-rays were first used to image the ventricular systems of the brain using injections of air to enhance contrast [7]. Computerized axial tomography (CT scanning) was developed in the early 1970s and used to produce cross-sectional images of the brain.

Later, in the early 1980s, single photon emission computed tomography (SPECT) and positron emission tomography (PET) were introduced. Both modalities provide three-dimensional (tomographic) images of the distribution of injected radioactive tracer molecules, from which brain function and receptor densities can be determined. Magnetic resonance imaging was introduced clinically in the early 1980s. Since then, MRI has become a widely used technique in neuroimaging, particularly due to its soft tissue contrast and zero radiation dose, as opposed to CT, SPECT and PET.

## 1.3. MAGNETIC RESONANCE IMAGING

MAGNETIC resonance imaging (MRI) is an imaging technique, which exploits the interaction between an applied magnetic field and nuclei that possess a nuclear spin. In medical imaging applications, the hydrogen nucleus is frequently used because it is most abundant in the human body and yields a relatively large net magnetic moment.

Hydrogen nuclei, when placed in an external magnetic field, give rise to a net magnetization parallel to the applied magnetic field. Application of a radio-frequency (RF) pulse can flip this magnetization into the orthogonal, transverse plane. After tipping, the transverse component of the magnetization produces an oscillating magnetic field, which induces a (detectable) current in a receiver coil. Gradient coils are used to create approximately linear variations of the external magnetic field to enable spatial localization of the measured MRI signal by means of slice-selection, frequency-encoding and phase-encoding.

A pulse sequence consisting of a configuration of RF and gradient pulses are at the basis of different types of image contrast. For example, pulse sequences can be designed to generate contrast based on differences in the density of protons (PD), the decay rate of the transverse component of the magnetization (T2-relaxation), or the recovery rate of the parallel component of the magnetization (T1-relaxation). Examples of PD-weighted, T1-weighted and T2-weighted images are shown in figure 1.3.

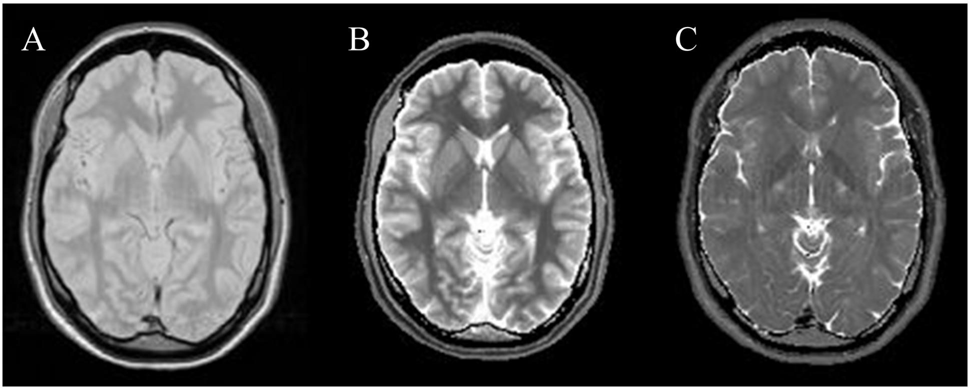

Figure 1.3: Axial slice of A) PD-weighted image, B) T1-weighted image, C) T2-weighted image [8].

## 1.4. DIFFUSION-WEIGHTED MAGNETIC RESONANCE IMAGING

### 1.4.1. DIFFUSION PROCESSES IN TISSUE

Atoms and molecules in fluids at temperatures above absolute zero are in constant motion. Due to collisions with other atoms and molecules, each atom or molecule makes random movements. This is also known as Brownian motion [9]. In case of free diffusion, a Gaussian distribution describes the random displacements after a time $t$. The mean squared displacement is given by Einstein's equation:

$$\langle x^2 \rangle = 2nDt, \tag{1.1}$$

where $n$ is the number of dimensions, $D$ is the diffusion constant, and $t$ is the diffusion time. For free water at body temperature, the diffusion coefficient is approximately 3 $\mu m^2/ms$, so that the root mean squared displacement (in 3D) is 30-42 μm in 50-100 ms.

Diffusion may be hindered or restricted, however, due to presence of diffusion barriers (e.g. cell membranes) (figure 1.4). Effectively, this can result in shorter net displacements compared to free diffusion. In restricted diffusion, water molecules are trapped within an enclosed compartment such that the net displacement is limited.

The degree of hindrance or restriction by diffusion barriers can be orientationally-dependent to yield an anisotropic diffusion pattern. For instance, in white matter primarily the diffusion perpendicular to the axon orientation is hindered or restricted by the myelin sheaths around the axons, whereas diffusion parallel to the axon orientation is relatively free.

### 1.4.2. PULSED GRADIENT SPIN ECHO PULSE SEQUENCE

The effect of diffusion on the MRI signal was first observed by Hahn in 1950 [10]. Subsequently, Torrey modeled the diffusion through a modification of the Bloch equations in 1956 [11]. Stejskal and Tanner introduced strong bipolar gradients in the pulse sequence to measure the diffusion in 1965 [12]. Even nowadays, their pulsed gradient spin echo (PGSE) pulse sequence is still at the basis of most diffusion-weighted MRI techniques.

The PGSE pulse sequence is shown in figure 1.5. It contains a symmetric pair of

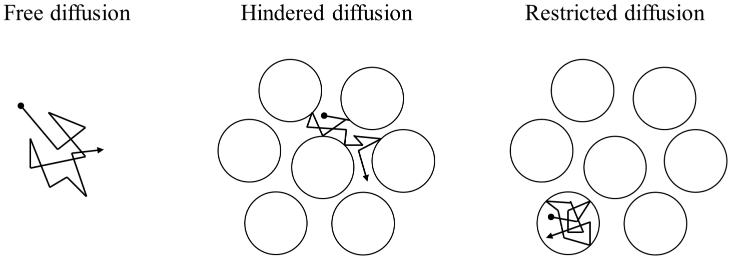

Figure 1.4: Illustration of free diffusion, hindered diffusion and restricted diffusion.

diffusion-sensitizing gradients before and after the 180° RF pulse. The first diffusion-sensitizing gradient will offset the phase of the spins by an amount depending on their position along the gradient orientation. For stationary spins, the second diffusion-sensitizing gradient will result in rephasing of the spins. However, for spins that diffuse along the gradient orientation, no complete rephasing occurs. The larger the diffusion along the gradient orientation, the less perfect the rephasing and the more attenuation of the diffusion-weighted signal is observed.

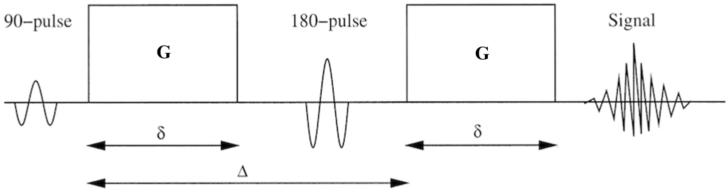

Figure 1.5: The PGSE pulse sequence.

In case of Gaussian diffusion with diffusion constant $D$, the diffusion-weighted signal $S$ can be modeled as:

$$S = S_0 \exp(-bD), \tag{1.2}$$

where $S_0$ is the signal obtained without diffusion-sensitizing gradients, and $b$ (also known as the $b$-value) is a parameter expressing the amount of diffusion-weighting computed as:

$$b = \gamma^2 G^2 \delta^2 (\Delta - \frac{\delta}{3}), \tag{1.3}$$

where $\gamma$ is the gyromagnetic ratio, $G$ is the gradient strength, $\delta$ is the gradient duration, and $\Delta$ the time between the two diffusion-sensitizing gradients.

In figure 1.6 the intensity of the diffusion-weighted MRI signal is shown for different orientations and different diffusion-weightings of the diffusion-sensitizing gradients. In certain brain regions the diffusion-weighted MRI signal is relatively independent of the orientation of the diffusion-sensitizing gradients: particularly in the CSF and the grey matter. In other brain regions, especially the white matter, the diffusion-weighted MRI signal depends strongly on the gradient orientation (white arrows in figure 1.6), indicating an anisotropic diffusion profile.

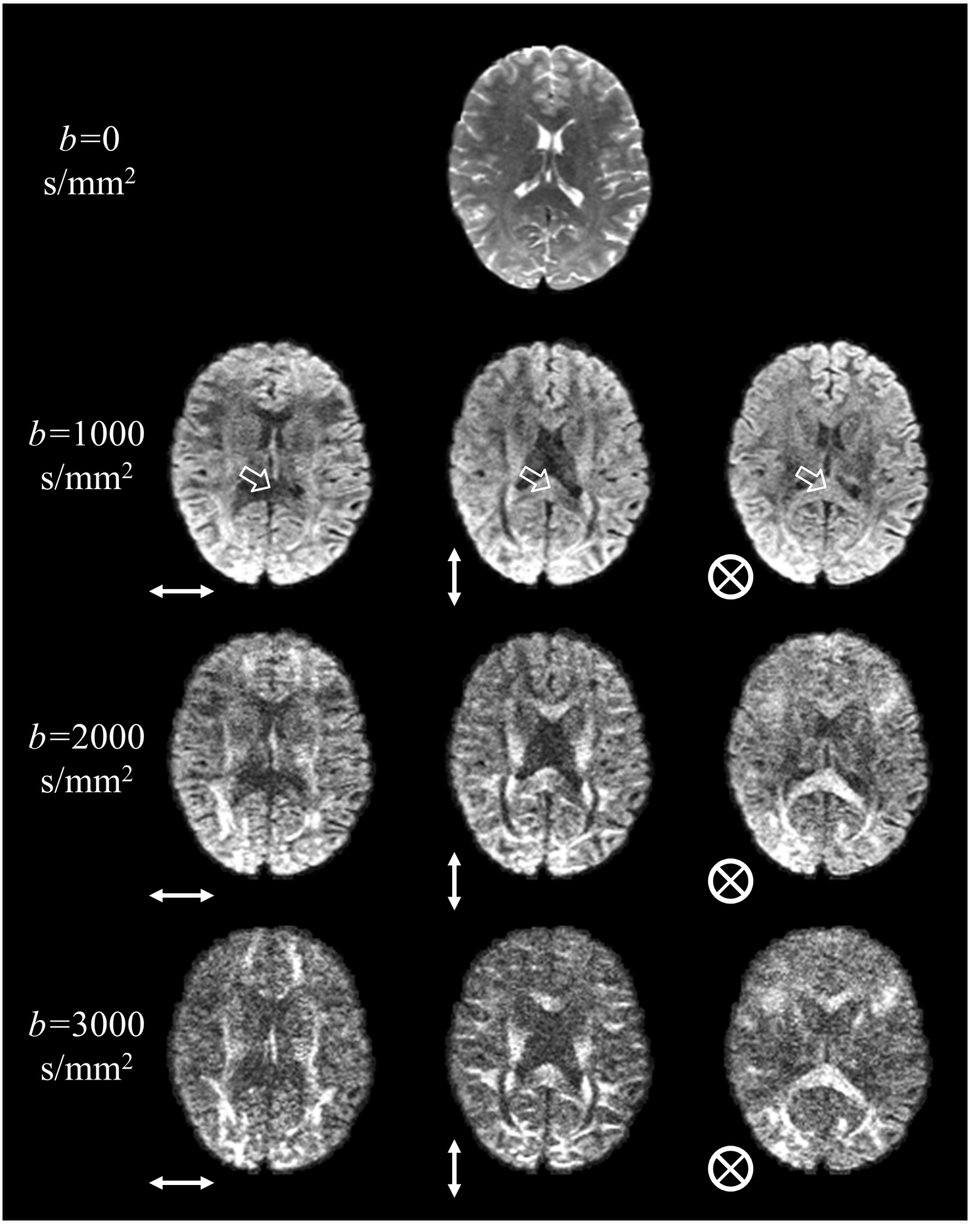

Figure 1.6: Axial slices of diffusion-weighted images with diffusion-sensitizing gradients in different orientations ($x$, $y$ and $z$, from left to right) and different diffusion-weighting ($b$-value = [0, 1000, 2000, 3000] s/mm$^2$). Images based on DW-MRI data from [13].

### 1.4.3. IMAGE QUALITY

A DW-MRI dataset typically contains several images acquired without diffusion-sensitizing gradients and between ten and several hundred diffusion-weighted images (DWIs). Each such DWI is acquired with different settings for the orientation and strength ($b$-value) of the diffusion-sensitizing gradient. In addition to the number of DWIs and their $b$-values, also the spatial resolution, and the signal-to-noise ratio (SNR) of the DWIs are relevant parameters. Taking into account the study goal and available scan time, suitable trade-offs are made between these parameters when designing a DW-MRI protocol.

The strength of the main magnetic field is an important factor affecting image quality. A stronger magnetic fields increases the SNR of the MRI signal. Furthermore, a higher SNR allows the application of stronger diffusion-weightings, but can also be used to increase the spatial resolution or decrease the total scan time. Therefore, acquiring DW-MRI datasets on a 3T MRI-scanner is generally preferred over acquisitions on a 1.5T MRI-scanner. The use of stronger magnetic fields for DW-MRI, e.g. 7T MRI-scanners, is in development [14].

### 1.4.4. ANALYSIS OF DIFFUSION-WEIGHTED MAGNETIC RESONANCE IMAGING

By fitting an appropriate diffusion model to the acquired DWI data, characteristics of the diffusion profile can be obtained that give insight into the tissue microstructure. A common technique to analyze DW-MRI data is diffusion tensor imaging (DTI), in which the water diffusion is modeled by a 3D Gaussian diffusion profile [15]. From the diffusion tensor, quantitative DTI metrics such as the fractional anisotropy (FA), mean diffusivity (MD) and axial diffusivity (AxD) can be derived. Examples of axial slices of the FA, MD and AxD are shown in figure 1.7. These DTI metrics are often used as an imaging biomarker for white matter tract integrity to study, for example, neurodegenerative diseases or brain ageing [16, 17].

Despite its widespread use, the diffusion tensor model is known to have important limitations. White matter voxels may contain intra-axonal, extracellular and free water diffusion compartments [18], or may contain more than one coherently orientated fiber tract [19, 20], which renders the use of the single diffusion tensor model inappropriate. Therefore, the analysis of conventional DTI metrics can have undesirable effects: spurious changes may be detected in the radial and axial diffusivity [21], FA may lack sensitivity to detect changes in the white matter microstructure [22], and FA may seem to be increased merely due to selective degeneration of a fiber population [23].

Many alternative parametric models have been proposed to provide a more adequate description of the diffusion. The most popular ones are summarized in Table 1.1. A common limitation of these approaches is that more complicated DW-MRI protocols are required. Therefore, conventional DW-MRI datasets, especially datasets with a limited number of DWIs and acquired with a single diffusion-weighting, may not support the application of these techniques.

Table 1.1: Different methods to analyze diffusion-weighted MRI data.

| Name | Description | Ref. |
|---|---|---|
| DTI | Diffusion tensor imaging (DTI). The water diffusion profile is modeled using a single (3D) Gaussian distribution. | [15] |
| DSI | Diffusion spectrum imaging (DSI). Diffusion data is acquired on a 3D Cartesian grid in q-space. An inverse Fourier transform of the q-space data yields the ensemble average (diffusion) propagator (EAP). | [24] |
| Q-ball Imaging | Diffusion data is acquired on a single shell in q-space. A Funk-Radon transform of the q-space data is applied to obtain the diffusion orientation distribution function (dODF), i.e. the radial projection of the EAP. | [25] |
| Spherical Deconvolution | Diffusion data is acquired on a single shell in q-space. White matter fiber bundles are assumed to have identical diffusion characteristics, such that the diffusion-weighted signal can be modeled as the convolution over the sphere of a response function with a fiber orientation density function (fODF). | [26, 27] |
| Diffusion Kurtosis Imaging | Diffusion kurtosis imaging is an extension of DTI. The diffusion tensor and kurtosis tensor (related to the fourth standardized moment of the EAP) are estimated from diffusion data acquired on multiple shells in q-space. | [28] |
| Multi-Tensor Models | The water diffusion profile is modeled with multiple Gaussian diffusion compartments. Constraints are typically introduced to decrease the number of free parameter and make estimation feasible. | [20, 29] |
| Ball-and-Sticks Model | The diffusion-weighted signal is modeled as an infinitely anisotropic component for each fiber orientations, and a single isotropic component. | [30] |
| CHARMED | Composite hindered and restricted model of diffusion (CHARMED). The diffusion-weighted signal modeled with a hindered (Gaussian) diffusion compartment and one or more compartments with restricted diffusion within cylinders. | [31, 32] |
| AxCaliber and ActiveAx | Extensions of CHARMED in which the mean (ActiveAx) or full (AxCaliber) axonal diameter distribution are also estimated from the diffusion-weighed signal. | [33, 34] |
| NODDI | Neurite orientation dispersion and density imaging (NODDI). The diffusion-weighted signal is modeled with three diffusion compartments, i.e. an intra-axonal, an extra-cellular and a free diffusion compartment. | [18] |

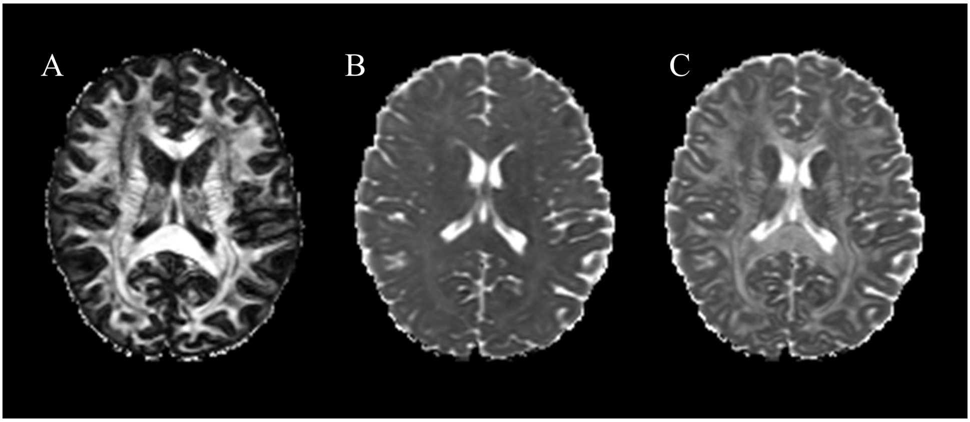

Figure 1.7: Axial slice of A) Fractional anisotropy (FA), B) Mean diffusivity (MD), C) Axial diffusivity (AxD). Images based on DW-MRI data from [13].

## 1.5. ROTTERDAM SCAN STUDY

THE focus of this thesis is on the analysis of the diffusion-weighted data acquired in the context of the Rotterdam Scan Study [35]. The Rotterdam Scan Study is part of the Rotterdam Study, a prospective population-based cohort study with more than 10.000 participants to investigate factors that determine the prevalence of various diseases in elderly people. The Rotterdam Scan Study focuses specifically on neurological diseases by performing neuroimaging. Participants of the Rotterdam Study therefore undergo brain MRI on a 1.5T MRI scanner as part of the protocol since 2005.

Because of the longitudinal setting of the Rotterdam Scan Study, researchers were very conservative with introducing changes in the procedures to acquire the data. Therefore, despite significant advances in hardware and software, there have been limited upgrades to the MRI scanner and imaging protocols. As a result, the diffusion-weighted data in the RSS have been (and still are) acquired with a conventional diffusion-weighted protocol on a 1.5T MRI scanner, i.e. 25 different gradient orientations with a $b$-value of 1000 s/mm$^2$ and a relatively low spatial resolution of 2.2 mm x 3.3 mm x 3.5 mm.

## 1.6. THESIS OBJECTIVES

IN neuroimaging population studies, such as the Rotterdam Scan Study (RSS) [35], image features are related to clinical parameters to study disease processes, quantify disease progression, or identify subjects at risk. An extensive phenotype is typically available for all of the study subjects, including multi-modality imaging data. These image features are ideally as accurate, precise and specific as possible, such that unambiguous conclusions can be drawn.

DW-MRI is an imaging modality used in the RSS to provide diffusion statistics that represent the local tissue microstructure. This is a challenging task as the relation between the DW-MRI signal and the local tissue microstructure is not straightforward.

In particular, simple diffusion models (e.g. DTI) do not capture the complexity of the tissue microstructure adequately and may therefore provide diffusion statistics that are heavily biased. More advanced diffusion models provide a more accurate quantification of the tissue microstructure, but cannot be reliably estimated from a small number of DWIs acquired with a single non-zero $b$-value. Furthermore, the low spatial resolution of conventional DW-MRI data makes estimated diffusion properties very susceptible to partial-volume effects (mixing of the MRI signal originating from different tissues).

The objectives of this thesis are:

- To enhance our insight in the relation between tissue structure and the DW-MRI signal from conventional MRI sequences.
- To develop methods to quantify diffusion properties in the brain as accurately and precisely as possible based on conventional DW-MRI data. Specifically, we aim to:
  - Investigate how we can best analyze brain regions susceptible to partial volume effects with the CSF.
  - Explore how we can best analyze brain regions with crossing fiber-regions.
  - Investigate how longitudinal DW-MRI can be leveraged to increase the precision of computed diffusion statistics.

We will show that the developed techniques are also highly relevant to enhance more advanced DW-MRI studies.

## 1.7. THESIS OUTLINE

The thesis is organized as follows:

- In chapter 2 the relation between the extra-axonal diffusion compartment and the DW-MRI signal is investigated. Experimental data from an anisotropic hardware phantom and Monte Carlo diffusion simulations are applied to determine the sensitivity to substrate parameters (i.e. fiber diameter, fiber packing fraction) and experimental parameters (i.e. diffusion time, diffusion-sensitizing gradient duration and strength).
- In chapter 3 a novel framework is described to analyze white matter structures that are sensitive to partial volume effects with CSF. We explore how a two-compartment diffusion model can be employed with conventional DW-MRI data to estimate diffusion parameters that may be more robust to partial volume effects with CSF than parameters obtained with DTI.
- In chapter 4 and 5 we explore the feasibility of analysing conventional DW-MRI data with a crossing-fiber model. Specifically, in chapter 4, we explore the use of orientation priors and consistent model selection to decrease random variations across subjects. Subsequently, in chapter 5 we introduce a framework to decrease the within-subject variance of diffusion statistics in longitudinal analyses.
- Finally, in chapter 6 the advantages and limitations of the proposed methods will be discussed and an outlook to the future is presented.

## REFERENCES

[1] U. Braun, S. F. Muldoon, and D. S. Bassett, *On human brain networks in health and disease,* eLS (2015).

[2] F. Aboitiz, A. B. Scheibel, R. S. Fisher, and E. Zaidel, *Fiber composition of the human corpus callosum,* Brain Research **598**, 143 (1992).

[3] Newhavenscience.org, *Illustration of a neuron,* [Online; accessed on October 28, 2017].

[4] H. Gray, *Anatomy of the human body* (Lea & Febiger, 1918).

[5] A. Zaimi, T. Duval, A. Gasecka, D. Côté, N. Stikov, and J. Cohen-Adad, *Axonseg: open source software for axon and myelin segmentation and morphometric analysis,* Frontiers in neuroinformatics **10** (2016).

[6] S. Sandrone, M. Bacigaluppi, M. R. Galloni, S. F. Cappa, A. Moro, M. Catani, M. Filippi, M. M. Monti, D. Perani, and G. Martino, *Weighing brain activity with the balance: Angelo mosso's original manuscripts come to light,* Brain **137**, 621 (2013).

[7] W. E. Dandy, *Ventriculography following the injection of air into the cerebral ventricles,* Annals of surgery **68**, 5 (1918).

[8] fmri.mchmi.com, *Axial slice of pd-weighted, t1-weighted and t2-weighted image,* [Online; accessed October 28, 2017].

[9] R. Brown, *Xxvii. a brief account of microscopical observations made in the months of june, july and august 1827, on the particles contained in the pollen of plants; and on the general existence of active molecules in organic and inorganic bodies,* Philosophical Magazine Series 2 **4**, 161 (1828).

[10] E. L. Hahn, *Spin echoes,* Physical review **80**, 580 (1950).

[11] H. C. Torrey, *Bloch equations with diffusion terms,* Physical review **104**, 563 (1956).

[12] E. Stejskal and J. Tanner, *Spin diffusion measurements: spin echoes in the presence of a time-dependent field gradient,* The journal of chemical physics **42**, 288 (1965).

[13] S. N. Sotiropoulos, S. Jbabdi, J. Xu, J. L. Andersson, S. Moeller, E. J. Auerbach, M. F. Glasser, M. Hernandez, G. Sapiro, M. Jenkinson, D. A. Feinberg, E. Yacoub, C. Lenglet, D. C. Van Essen, K. Ugurbil, and T. E. J. Behrens, *Advances in diffusion mri acquisition and processing in the human connectome project,* Neuroimage **80**, 125 (2013).

[14] D. L. Polders, A. Leemans, J. Hendrikse, M. J. Donahue, P. R. Luijten, and J. M. Hoogduin, *Signal to noise ratio and uncertainty in diffusion tensor imaging at 1.5, 3.0, and 7.0 tesla,* Journal of Magnetic Resonance Imaging **33**, 1456 (2011).

[15] P. J. Basser, J. Mattiello, and D. LeBihan, *Mr diffusion tensor spectroscopy and imaging,* Biophysical journal **66**, 259 (1994).

[16] Y. Liu, G. Spulber, K. K. Lehtimäki, M. Könönen, I. Hallikainen, H. Gröhn, M. Kivipelto, M. Hallikainen, R. Vanninen, and H. Soininen, *Diffusion tensor imaging and tract-based spatial statistics in alzheimer's disease and mild cognitive impairment,* Neurobiology of Aging **32**, 1558 (2011).

[17] M. W. Vernooij, M. de Groot, A. van der Lugt, M. A. Ikram, G. P. Krestin, A. Hofman, W. J. Niessen, and M. M. Breteler, *White matter atrophy and lesion formation explain the loss of structural integrity of white matter in aging,* Neuroimage **43**, 470 (2008).

[18] H. Zhang, T. Schneider, C. A. Wheeler-Kingshott, and D. C. Alexander, *Noddi: practical in vivo neurite orientation dispersion and density imaging of the human brain,* Neuroimage **61**, 1000 (2012).

[19] A. L. Alexander, K. M. Hasan, M. Lazar, J. S. Tsuruda, and D. L. Parker, *Analysis of partial volume effects in diffusion-tensor mri,* Magnetic Resonance in Medicine **45**, 770 (2001).

[20] D. S. Tuch, T. G. Reese, M. R. Wiegell, N. Makris, J. W. Belliveau, and V. J. Wedeen, *High angular resolution diffusion imaging reveals intravoxel white matter fiber heterogeneity,* Magnetic Resonance in Medicine **48**, 577 (2002).

[21] C. A. Wheeler-Kingshott and M. Cercignani, *About "axial" and "radial" diffusivities,* Magnetic Resonance in Medicine **61**, 1255 (2009).

[22] C. Pierpaoli, A. Barnett, S. Pajevic, R. Chen, L. Penix, A. Virta, and P. Basser, *Water diffusion changes in wallerian degeneration and their dependence on white matter architecture,* Neuroimage **13**, 1174 (2001).

[23] G. Douaud, S. Jbabdi, T. E. J. Behrens, R. A. Menke, A. Gass, A. U. Monsch, A. Rao, B. Whitcher, G. Kindlmann, P. M. Matthews, and S. Smith, *Dti measures in crossing-fibre areas: Increased diffusion anisotropy reveals early white matter alteration in mci and mild alzheimer's disease,* Neuroimage **55**, 880 (2011).

[24] V. J. Wedeen, P. Hagmann, W. I. Tseng, T. G. Reese, and R. M. Weisskoff, *Mapping complex tissue architecture with diffusion spectrum magnetic resonance imaging,* Magnetic resonance in medicine **54**, 1377 (2005).

[25] D. S. Tuch, *Q-ball imaging,* Magnetic resonance in medicine **52**, 1358 (2004).

[26] J.-D. Tournier, F. Calamante, D. G. Gadian, and A. Connelly, *Direct estimation of the fiber orientation density function from diffusion-weighted mri data using spherical deconvolution,* Neuroimage **23**, 1176 (2004).

[27] J.-D. Tournier, F. Calamante, and A. Connelly, *Robust determination of the fibre orientation distribution in diffusion mri: non-negativity constrained super-resolved spherical deconvolution,* Neuroimage **35**, 1459 (2007).

[28] J. H. Jensen, J. A. Helpern, A. Ramani, H. Lu, and K. Kaczynski, *Diffusional kurtosis imaging: The quantification of non-gaussian water diffusion by means of magnetic resonance imaging,* Magnetic resonance in medicine **53**, 1432 (2005).

[29] M. Caan, G. Khedoe, D. Poot, A. den Dekker, S. Olabarriaga, K. Grimbergen, L. van Vliet, and F. Vos, *Adaptive noise filtering for accurate and precise diffusion estimation in fiber crossings,* in *Medical Image Computing and Computer-Assisted Intervention–MICCAI 2010* (Springer, 2010) pp. 167–174.

[30] T. Behrens, H. J. Berg, S. Jbabdi, M. Rushworth, and M. Woolrich, *Probabilistic diffusion tractography with multiple fibre orientations: What can we gain?* Neuroimage **34**, 144 (2007).

[31] Y. Assaf, R. Z. Freidlin, G. K. Rohde, and P. J. Basser, *New modeling and experimental framework to characterize hindered and restricted water diffusion in brain white matter,* Magnetic Resonance in Medicine **52**, 965 (2004).

[32] Y. Assaf and P. J. Basser, *Composite hindered and restricted model of diffusion (charmed) mr imaging of the human brain,* Neuroimage **27**, 48 (2005).

[33] Y. Assaf, T. Blumenfeld-Katzir, Y. Yovel, and P. J. Basser, *Axcaliber: a method for measuring axon diameter distribution from diffusion mri,* Magnetic resonance in medicine **59**, 1347 (2008).

[34] D. C. Alexander, P. L. Hubbard, M. G. Hall, E. A. Moore, M. Ptito, G. J. Parker, and T. B. Dyrby, *Orientationally invariant indices of axon diameter and density from diffusion mri,* Neuroimage **52**, 1374 (2010).

[35] M. A. Ikram, A. van der Lugt, W. J. Niessen, P. J. Koudstaal, G. P. Krestin, A. Hofman, D. Bos, and M. W. Vernooij, *The rotterdam scan study: design update 2016 and main findings,* European journal of epidemiology **30**, 1299 (2015).

# 2

# MONTE CARLO SIMULATION OF DW-MRI COMPARED TO MEASUREMENTS IN A HARDWARE PHANTOM

*The main purpose of this chapter is to investigate the accuracy of Monte Carlo simulations of spins subject to hindered diffusion in comparison to measurements of a hardware phantom with varying fiber packing fractions. The diffusion of water between randomly packed parallel solid cylinders was modeled using a Monte Carlo diffusion simulator, and subsequently used to simulate diffusion-weighted signals with b-values between 0 and 5000 s/mm*$^2$*. Simulated diffusion-weighted signals were compared to experimentally obtained data from a hardware fiber phantom constructed from Dyneema fiber with a variable fiber packing fraction between 0.45 and 0.75 and a diameter of 16 µm. Furthermore, the dependency of the simulated diffusion-weighted signal on the fiber diameter was studied by simulating diffusion-weighted signals from substrates with different fiber packing fractions (0.45 to 0.75) and different diameters (4 to 20 µm). In both the simulated and experimentally acquired data non-Gaussian diffusion was observed. Furthermore, the simulated signal was in reasonably good agreement with the experimentally acquired data up to a packing fraction of 0.65. The simulated diffusion-weighted signals appeared relatively independent of cylinder diameter up to b=1500 s/mm*$^2$*. Substrates with a smaller cylinder diameter resulted for b-values higher than 1500 s/mm*$^2$ *in a larger attenuation of the diffusion-weighted signal. The Monte Carlo diffusion simulations accurately matches the experimental data from the hardware phantom. It may allow studying the complex link between the diffusion-weighted MRI signal and the underlying microstructure.*

---

G.A.M. Arkesteijn, R. Verweij, D.H.J. Poot, E. Farrher, F. Grinberg, M.W.A. Caan, L.J. van Vliet, and F.M. Vos, manuscript in preparation.

## 2.1. INTRODUCTION

DIFFUSION-WEIGHTED magnetic resonance imaging (DW-MRI) is a non-invasive technique for imaging the diffusion of water molecules [1]. It is frequently used to assess the brain's white matter integrity, because it provides insight into the microstructural organization of neural fibers [2]. A common approach, known as diffusion tensor imaging (DTI) [3], fits a symmetric, positive-definite tensor to the diffusion data in each voxel.

DTI assumes that there is a single Gaussian diffusion compartment in a voxel. However, the microstructure in the brain white matter is known to be much more complex. Accordingly, sophisticated models of the tissue microstructure take the contribution of different diffusion compartments into account [4]. Particularly, intra-axonal diffusion is frequently modeled as diffusion inside parallel impermeable cylinders [5] or as diffusion inside orientation-dispersed sticks [6]. Extra-axonal diffusion is frequently modeled using a Gaussian diffusion compartment [5, 6], or as a spherical convolution of a Gaussian diffusion compartment with a neurite distribution function [7]. Furthermore, a simple tortuosity model [8] that relates the extra-axonal diffusivity to the axon density, has been used to reduce the number of free parameters of this extra-axonal Gaussian diffusion compartment [6, 9]. More complex tortuosity models also take cell size distribution and packing geometry into account [10]. Such sophisticated models may provide new anatomical insights or biomarkers for diseases.

Diffusion phantoms are powerful tools to study the complex link between the tissue microstructure and the acquired DW-MRI signal. Biological diffusion phantoms include plants [11] or animal spinal cords [12]. Synthetic diffusion phantoms exist in the form of isotropic liquids [13], capillary phantoms [14–17] or fiber phantoms [18–21]. The geometry of synthetic diffusion phantoms is typically well known, which is convenient for validation purposes. However, a limitation of synthetic diffusion phantoms is that typically solid fibers are used, so that there is no representation of the intra-axonal diffusion. Furthermore, the diameters of these solid fibers (approximately 16 µm) are much larger than typical axon diameters (0.1 µm to 2 µm) [22].

Numerical diffusion phantoms provide a flexible alternative to hardware diffusion phantoms. Particularly, Monte Carlo simulations can simulate the diffusion in very complex microstructures that cannot be easily analyzed with analytical models or with the aid of a hardware phantom. For example, Monte Carlo simulations have been used to validate theoretical models [8, 23], to validate diffusion phantoms [24, 25], to study cell swelling [26, 27], or to generate synthetic datasets [28, 29].

The main purpose of this chapter is to compare measurements from a hardware phantom in structures with varying fiber packing fraction (packing fraction) to Monte Carlo simulations. The hardware phantom consists of solid fibers, and acts as a model for extra-axonal diffusion [19]. The influence of relevant Monte Carlo simulation parameters (i.e. number of spins, step size, and voxel size), as well as substrate parameters (i.e. the packing fraction, diameter, and type of packing of the fibers) on the diffusion MRI signal for various diffusion weightings is investigated. Furthermore, these simulations are compared to diffusion data from the hardware phantom.

## 2.2. METHODS

### 2.2.1. HARDWARE PHANTOM

The hardware phantom used in this study was constructed by Farrher et al. [19]. A photograph of the phantom is shown in figure 2.1A and a schematic in figure 2.1B. It consists of hydrophobic polyethylene (Dyneema DTX70) fibers with a diameter of approximately 16 µm wound in two different orientations around a Perspex support. As such, the hardware phantom contains different regions including a compressed single fiber region, a (slightly) diverging single fiber region and a crossing-fibers region. This chapter focuses on the diverging, single fiber region denoted by the red squares in figure 2.1, where a range of different fiber packing fractions can be observed, as is shown in figure 2.1C.

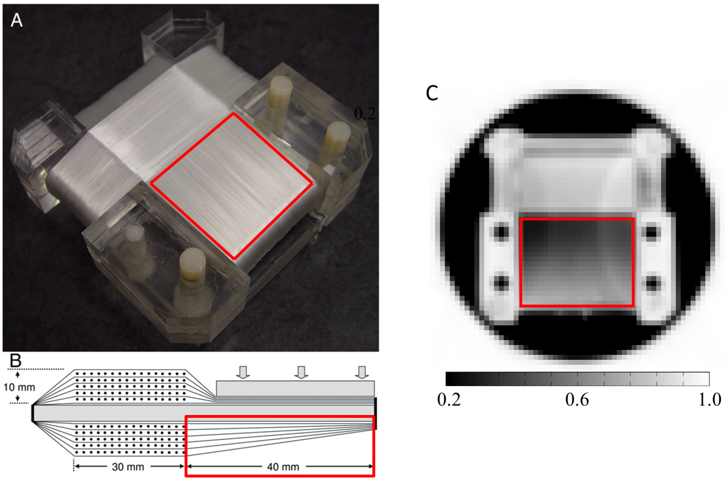

Figure 2.1: A) Photograph of the hardware phantom. B) Schematic of the hardware phantom. C) Estimated fiber packing fraction using Proton Density weighted MRI.

### 2.2.2. HARDWARE PHANTOM MEASUREMENTS AND ANALYSIS

Structural images and diffusion-weighted images of the hardware phantom were acquired on a Philips 3T MRI scanner. To minimize magnetic susceptibility artifacts, the phantom was positioned such that the main magnetic field and the fiber orientation in the compressed single fiber region were aligned.

#### MEASUREMENT OF PROTON DENSITY AND FIBER PACKING FRACTION

We assert that the fiber packing fraction in the region with diverging fibers is reflected in the local proton density (PD). PD was measured from a multi-echo spin-echo sequence: inter-echo time spacing ($\Delta$TE) = 40 ms, repetition time (TR) = 4835 ms, FOV of 160 mm x 160 mm, imaging matrix of 80 x 80, 64 slices with slice thickness of 2.2 mm, and voxel size of 2 mm x 2.2 mm x 2 mm. The intensity bias field was computed from the image with TE of 40 ms using a nonparametric intensity correction (N4ITK) [30]. Subsequently, each multi-echo image was divided by the bias field thus obtained, after which $T_2$ and PD were estimated by fitting the following model to the data using nonlinear least squares (Levenberg-Marquardt):

$$S(\Delta TE) = PD\exp(-\Delta TE/T_2). \tag{2.1}$$

Similar as in (19), a linear relation between fiber packing fraction and PD was assumed, and the packing fraction $f$ was estimated as:

$$f = 1 - \frac{PD}{PD_{\text{Bulk}}}, \tag{2.2}$$

where $\text{PD}_{\text{Bulk}}$ was an estimate of the PD in a nearby region outside the hardware phantom that only contained water.

### ACQUISITION AND PREPROCESSING OF DIFFUSION-WEIGHTED IMAGES

Diffusion-weighted images were acquired with a single shot, diffusion-weighted spin echo sequence (repetition time (TR) = 9017 ms, echo time (TE) = 120 ms, FOV of 240 mm x 240 mm, imaging matrix of 94 x 96, 50 slices with slice thickness of 2.5 mm, and reconstructed voxel size of 2.5 mm x 2.5 mm x 2.5 mm). Furthermore, in the directions perpendicular to the fibers diffusion-weighted images were acquired with the following $b$-values [0 400 700 1200 2000 3500 5000] $\text{s/mm}^2$ (gradient pulse length ($\delta$) = 22 ms and diffusion time ($\Delta$) = 80.5 ms). An additional image without diffusion-weighting ($b$-value = 0) was acquired with reversed phase-encode blips, such that distortions due to the susceptibility-induced off-resonance field could be corrected with the topup routine in FSL [31, 32].

### PROCESSING AND ANALYSIS OF DIFFUSION-WEIGHTED IMAGES

To facilitate the comparison between the acquired and simulated data, the diffusion kurtosis model was fitted [33]. More specifically, the following equation was fit (Levenberg-Marquardt) to each voxel of the acquired diffusion-weighted data:

$$S(b) = S_0 \exp\Big(-bD + \frac{1}{6}(bD)^2 K\Big), \tag{2.3}$$

where $S_0$ is the diffusion signal without diffusion weighting, $b$ is the '$b$-value' quantifying the diffusion-weighting, $D$ the diffusivity parameter, and $K$ the kurtosis parameter.

The fiber packing fraction, determined from the estimated PD using equation 2.2, was used to cluster the voxels in the region with diverging fibers into bins with a spacing of 0.05. For each bin, the (normalized) diffusion-weighted signal was calculated as $\text{average}(S(b)/(S_0))$. Furthermore, the average diffusivity ($D$) and the average kurtosis parameter ($K$) were computed and compared to simulated values (see below).

## 2.2.3. DIFFUSION SIMULATIONS

### MONTE CARLO DIFFUSION SIMULATIONS

We used a Monte Carlo simulation of random walkers to generate a three-dimensional diffusion profile of the water diffusion outside infinitely long parallel solid cylinders. The simulation was implemented in Matlab as described in [27]. In short, $N_S$ spins were assigned a random position in simulated 3D voxels through drawings from a uniform

(3D) distribution. Spins that were placed inside a cylinder were repeatedly assigned new random positions, until every spin had an initial position outside a cylinder. Next, the position of each spin was iteratively updated by adding a step vector with a fixed length $l$ and random direction. If this vector overlapped with a cylinder, the spin's step vector was reflected elastically at the boundary (multiple times if required).

Periodic boundary conditions were used for all substrates, i.e. the simulated voxel essentially repeated itself in the radial direction and was constant in the axial direction (see below). This approach enabled spins to move infinitely far in both the radial and axial directions. Practically, the spin position modulo the voxel dimensions was computed each iteration to efficiently check for collision with cylinder boundaries.

To support simulated voxels containing a large number of cylinders, an acceleration technique similar to [34] was used. Essentially, the simulated voxel was subdivided in much smaller subvoxels. The number of subvoxels was set to approximately 25% of the number of cylinders. From each subvoxel, the cylinders overlapping that subvoxel (or with a distance smaller than the diffusion step length) were identified in advance. Using the modulo operator, the corresponding subvoxel could be efficiently selected from the position of each spin. Subsequently, to check whether a spin had hit a cylinder boundary, only the distance to the few cylinders corresponding to the particular subvoxels needed to be computed (rather than distances to all cylinders in the complete simulated voxel).

The diffusivity $D$ in the simulation was set to $2.0 \cdot 10^{-3}$ mm$^2$/s reflecting the diffusivity of water at 20 degrees Celsius. To save disk space and memory space, spin positions were only stored every 1.0 ms.

### SIMULATED SUBSTRATES

Three different simulated substrates were simulated: squarely packed cylinders, hexagonally packed cylinders, and randomly packed cylinders (see figure 2.2). The cylinders had a diameter of 16 µm and were aligned in parallel in each substrate. The packing fraction of a substrate was defined as the ratio of the surface area covered by cylinders and the total area considered in a perpendicularly oriented plane. Different packing fractions were simulated by increasing/decreasing the space between the cylinders. For squarely packed and hexagonally packed cylinders, the packing fraction can be calculated over a small unit cell around each cylinder due to the periodicity in structure (see figure 2.2A and B for an example).

For substrates with random packing, cylinders were initially placed in a voxel using square packing with the desired packing fraction. Subsequently, cylinders were moved one-by-one in a random order by adding a Gaussian distributed displacement ($\mu$=0, $\sigma$=(cylinder radius)/4) to their initial positions. Updated positions were only accepted if it did not result in overlapping cylinders. This procedure was repeated 10.000 times the number of cylinders in the voxel. In figure 2.2C an example of a substrate with a random packing is shown.

### SIMULATION OF THE DIFFUSION-WEIGHTED MRI SIGNAL

The output of the diffusion simulation was used to synthesize the diffusion-weighted MRI signal. Similar to [27], all spins were initialized with phase $\phi$ equal to zero. In each

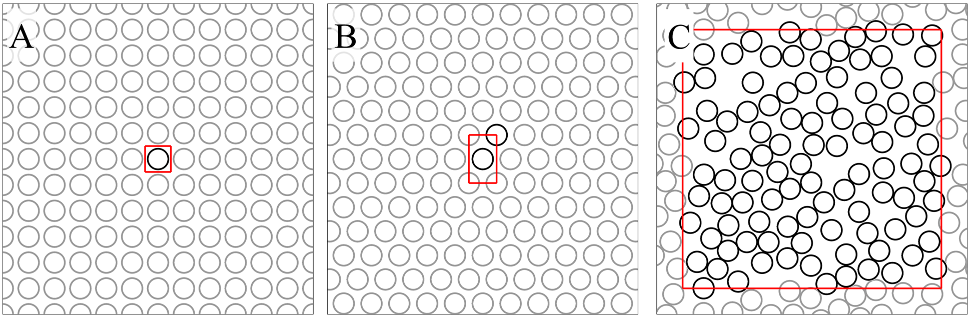

Figure 2.2: A) Photograph of the hardware phantom. B) Schematic of the hardware phantom. C) Estimated fiber packing fraction using Proton Density weighted MRI.

time step the phase of each spin was updated according to:

$$\Delta\phi = \gamma \mathbf{G}(t) \cdot \mathbf{x}(t) \Delta t, \tag{2.4}$$

where $\gamma$ is the gyromagnetic ratio for protons in water, $\mathbf{G}(t)$ is the gradient vector, $\mathbf{x}(t)$ the spin position at time $t$, and $\Delta t$ the duration of the time step. As in the hardware phantom, we merely focused on the radial part of the diffusion, i.e. $\mathbf{G}$ was oriented perpendicular to the fiber direction. Furthermore, rectangular gradient pulses were assumed with length ($\delta$ = 22 ms) and diffusion time ($\Delta$ = 80.5 ms) matching the MRI acquisition parameters. Since these gradient timings were in general not exactly a multiple of the time step $\Delta t$ (approximately 1 ms), we fractionally updated the phase at the start and end of the gradient pulses. The gradient strength was varied in steps to generate $b$-values from 0 to 5000 s/mm$^2$ in steps of 100 s/mm$^2$. The normalized diffusion-weighted MRI signal ($S/S_0$) was computed by summing up the contributions of all $N_S$ spins:

$$\frac{S(\mathbf{G},\Delta,\delta)}{S_0} = \frac{1}{N_S}\sum_{j=1}^{N_S} \exp(\phi_j). \tag{2.5}$$

## 2.3. EXPERIMENTS

### 2.3.1. EVALUATION OF PRECISION

The number of spins $N_S$, the number of simulated cylinders and the step size influence the precision of the simulated signal and as such needed to be set to appropriate values [27, 34]. To do so a substrate with random packing of cylinders and a packing fraction of 0.5 was generated. Other default settings to simulate the diffusion-weighted signal were: 100.000 spins, a step size of 5% of the cylinder diameter, and 2500 cylinders in a voxel sized 1x1x1 mm$^3$. The influence of the number of spins was studied by varying it between 1.000 and 100.000 spins, while keeping the default settings for the other parameters. Much the same way, the number of cylinders in the unit cell was varied between 100 cylinders in voxel (0.2x0.2x0.2 mm$^3$) and 2500 cylinders in a voxel (1.0x1.0x1.0 mm$^3$). Finally, the step size was varied between 0.5% and 10% of the cylinder diameter. At each setting the normalized diffusion-weighted signal was simulated ten times. The uncertainty of the simulation was determined by computing the corresponding standard deviation. Observe that this is a relative measure since the diffusion-weighted signal was normalized.

### 2.3.2. DEPENDENCY OF THE SIMULATED SIGNAL ON PACKING FRACTION AND CYLINDER DIAMETER

The dependency of the simulated signal on the packing fraction was evaluated by generating substrates of all three packings with different packing fractions and cylinder diameters. A voxel containing 2500 cylinders was used. Fiber densities ranged from 0.45 to 0.75 in steps of 0.05, while the diameter of the cylinders was varied from 4 µm to 20 µm in steps of 4 µm. Note that the step size in our simulations is set as a percentage of the cylinder diameter, by default 5% of the cylinder diameter. The (normalized) diffusion-weighted signal for each of these substrates was simulated, and diffusivity and kurtosis parameters were estimated by fitting equation 2.3.

### 2.3.3. DIFFUSION INSIDE CYLINDERS

For reference purposes, intra-cylinder diffusion was simulated as well. Spins were given a random initial position inside a cylinder. Similar to the diffusion simulation outside cylinders, the position of each spin was repeatedly updated by adding a step vector with a length equaling 5% of the cylinder diameter and random direction. Furthermore, collisions with the cylinder boundary were also assumed to be elastic. The diffusion-weighted MRI signal by these spins was computed similar as for spins outside the cylinders. The intra-cylinder diffusion was studied for different cylinder diameters, ranging from 4 µm to 20 µm in steps of 4 µm.

## 2.4. RESULTS

THE estimated fiber packing fraction in the hardware phantom is shown in figure 2.1C. The red square denotes the region of the phantom with slightly diverging fibers, in which the fiber packing fraction approximately ranges from 0.45 to 0.75. The estimated diffusivities and kurtosis parameters are shown in figure 2.3. The average diffusivity in the bulk (water outside the phantom) was $2.0 \cdot 10^{-3}$ mm$^2$/s.

### 2.4.1. EVALUATION OF PRECISION

The influence of the Monte Carlo simulation parameters on the precision of the simulated diffusion-weighted signal at different $b$-values is shown in figure 2.4. In the top-left figure, the standard deviation of the signal is plotted against the number of spins. A decrease in the standard deviation can be observed as the number of spins increases. This decrease is approximately proportional to the square root of the number of spins (i.e. linear on the logarithmic scale). In the top-right figure, the standard deviation of the signal versus the number of cylinders in the simulated voxel is shown. The standard deviation of the simulated diffusion signal also decreases when the simulated voxel contains more cylinders (approximately proportional to the square root of the number of cylinders). Observe that the default settings of 100.000 spins and 2500 cylinders in a voxel result in a standard deviation of approximately 0.003 (= 0.3% of $S_0$). Using these default settings,

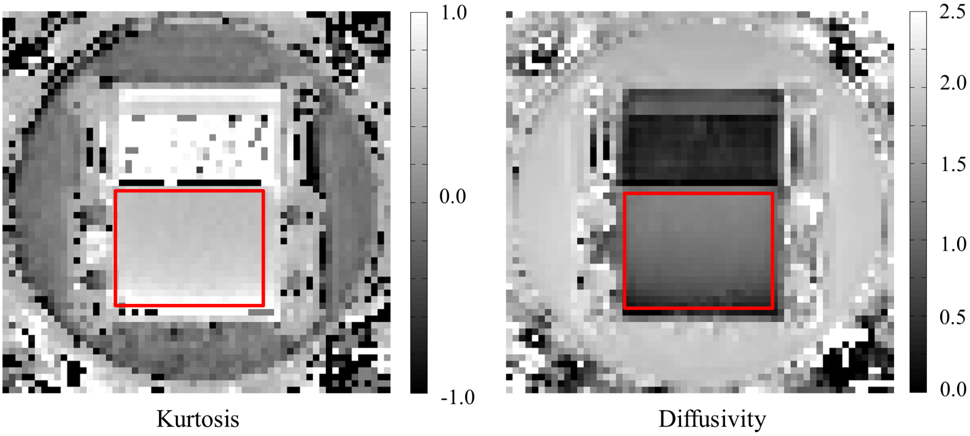

Figure 2.3: Estimated diffusivity and kurtosis parameters. The red box denotes the region of the phantom with diverging fibers. The unit of the diffusivity is in $10^{-3}$m$^2$/s.

the dependency on step size was evaluated. Results are shown in the bottom figure. The mean difference of approximately 0.002 between the default step size of 5% and the much smaller 0.5% of the cylinder diameter was comparable to the expected variance. Accordingly, we retain the applied default settings in the next experiments since they result in only a very small variation in signal.

### 2.4.2. DEPENDENCY OF THE SIMULATED SIGNAL ON PACKING FRACTION AND CYLINDER DIAMETER

In figure 2.5 the experimentally acquired (phantom) and simulated diffusion-weighted signals versus $b$-value are shown for different fiber densities and packing types. The figure demonstrates that the signal from the random packing is in reasonably good agreement with the experimental data (figure 2.5A) up to a packing fraction of 0.65. At packings larger than 0.65 the simulated signal was systematically smaller than the experimentally obtained signal. The hexagonal packing (figure 2.5B) and square packing (figure 2.5C) yielded diffusion-weighted signals that deviated largely from the experimentally acquired data.

Figure 2.6 shows the diffusivity and kurtosis parameters estimated from the experimentally acquired and simulated diffusion-weighted signal using random packings. The radial diffusivity estimated from the experimental data decreased from $1.3 \cdot 10^{-3}$ mm$^2$/s to $0.5 \cdot 10^{-3}$ mm$^2$/s while the packing fraction increased from 0.45 to 0.75. Over the same range of packing fractions, the kurtosis parameter increased from 0.54 to 1.07. Reasonable agreement was observed between the simulated and acquired data up to a packing fraction of 0.65.

Simulated diffusion-weighted signals as a function of the $b$-value for substrates with different cylinder diameters are visualized in the top row of figure 2.7. The initial slopes of these plots are rather linear. Simultaneously, the signals appear relatively independent of cylinder diameter up to $b$=1500 s/mm$^2$. However, at $b$-values more than 1500 s/mm$^2$

substrates with a smaller cylinder diameter yield a larger attenuation of the diffusion-weighted signal. The estimated diffusivity and kurtosis parameters as a function of packing fraction are shown in the bottom row of figure 2.7 for different fiber diameters. The diffusivity parameters appear primarily dependent on the packing fraction and not so much on the average cylinder radius. The kurtosis parameters, however, are sensitive to the cylinder diameter: smaller cylinder diameters result in smaller kurtosis parameters.

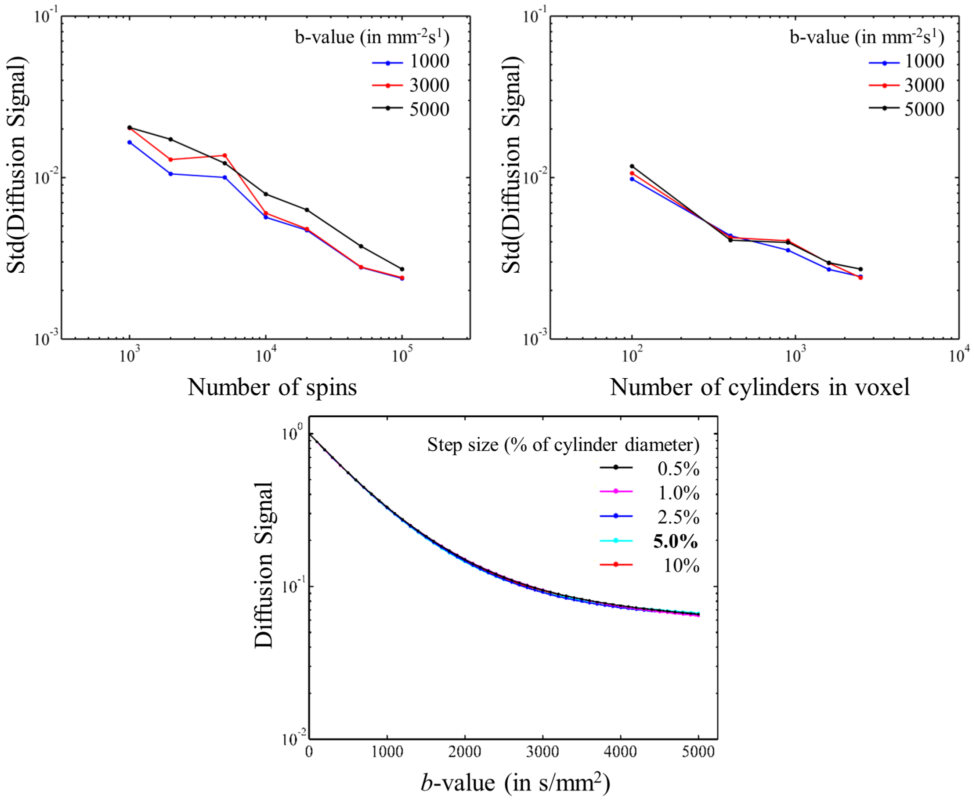

Figure 2.4: Dependency of Monte Carlo simulation on the number of spins (top-left), the number of cylinders in voxel (top-right), and the step size (bottom).

### 2.4.3. DIFFUSION INSIDE CYLINDERS

In figure 2.8 the simulated diffusion-weighted signal for diffusion inside cylinders is shown. Note that compared to diffusion outside the cylinders, there is much less attenuation of the signal. For diffusion inside cylinders with diameters of 8 μm or smaller, even at a relatively high $b$-value of 5000 s/mm$^2$ virtually no attenuation is visible.

## 2.5. DISCUSSION

WE investigated the relation between the normalized diffusion-weighted MRI signal in Monte Carlo simulations and in experimental acquisitions from a hardware

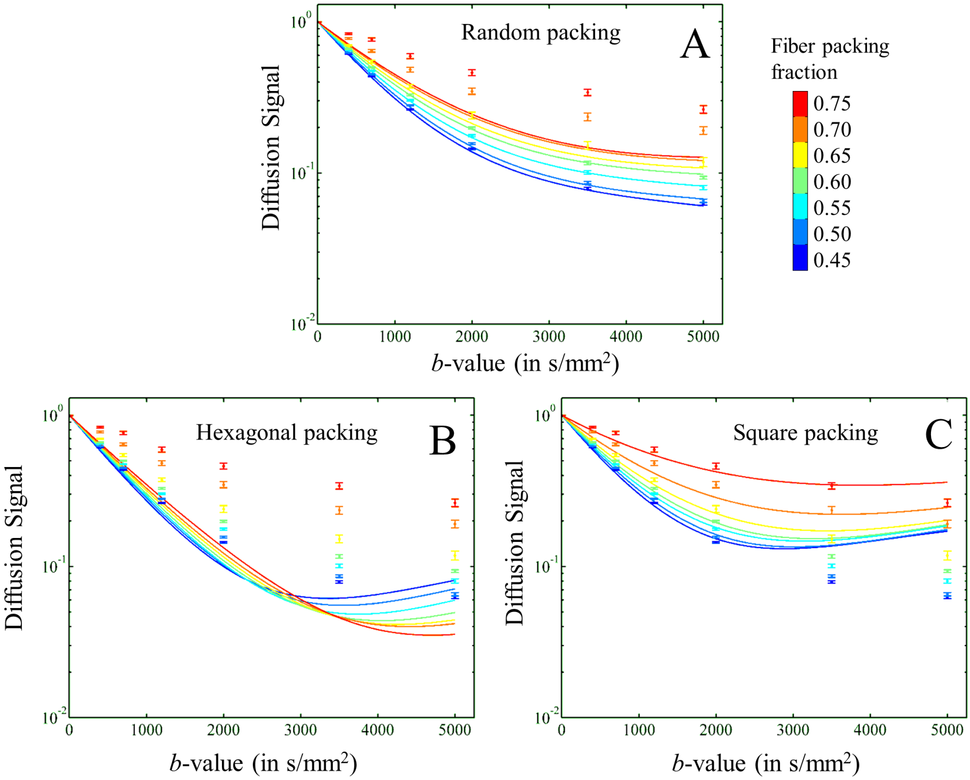

Figure 2.5: Experimentally acquired and simulated diffusion signals versus *b*-value for different fiber densities and packing types. Individual points represent experimental measurements from the phantom; continuous lines were obtained through simulations. Color indicates the packing fraction (see sidebar). Errorbars of the experimental data show the standard deviation of the mean.

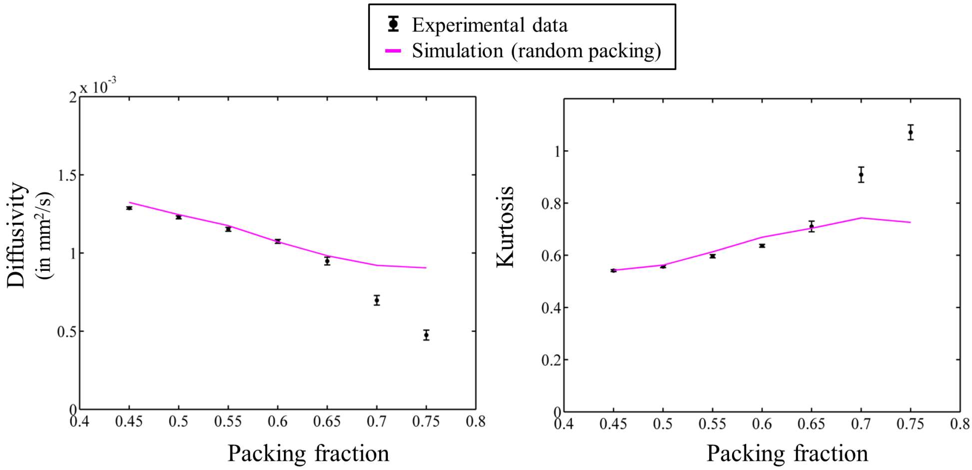

Figure 2.6: Diffusivity and kurtosis estimated from experimental and simulated diffusion data. Errorbars of the experimental data show the standard deviation of the mean.

phantom. In the Monte Carlo simulation, the influence of relevant simulation parameters (i.e. number of spins, step size), as well as substrate parameters (i.e. the packing fraction, diameter, and type of packing) on the diffusion-weighted MRI signal was investigated. In agreement with previous research [27, 34], the number of spins, and the step length were found to have a strong influence on the precision of the simulated signal. Our default setting yielded a very low variance and as such high precision of the simulation.

The periodic structure of substrates based on square and hexagonal packings resulted in unwanted oscillations of the simulated diffusion signal. Previously, such diffraction-like effects have been confirmed in NMR acquisitions of (periodic) porous solids [35]. With the random packing of cylinders we did not observe such effects.

For long diffusion times hindered diffusion (as opposed to restricted diffusion where random walkers are trapped inside cavities or axons) is expected to be adequately described by a Gaussian distribution. However, in this chapter an intermediate diffusion time of 80.5 ms was used, which yields an (unhindered) diffusion length of approximately 30 μm. Strong non-Gaussian signal-decay is therefore observed for simulated substrates with relatively large cylinder radii, but as the cylinder diameter decreases the diffusion decay signal becomes more Gaussian.

The simulations matched the experimental data very well up to packing fractions of 0.65. The relatively lower simulated signal above this threshold could reflect that spins are more confined in the hardware phantom than in the simulations. In the hardware phantom, fibers may be pushed against each other at high packing fractions effectively trapping water between the fibers whereas the simulated random packing always leaves some space between adjacent cylinders.

The simulation of the radial intra-axonal diffusion shows that it hardly affects the diffusion signal for representative diameters (smaller than or equal to 8 μm). This confirms the general notion that the radial intra-axonal diffusion cannot be estimated in white

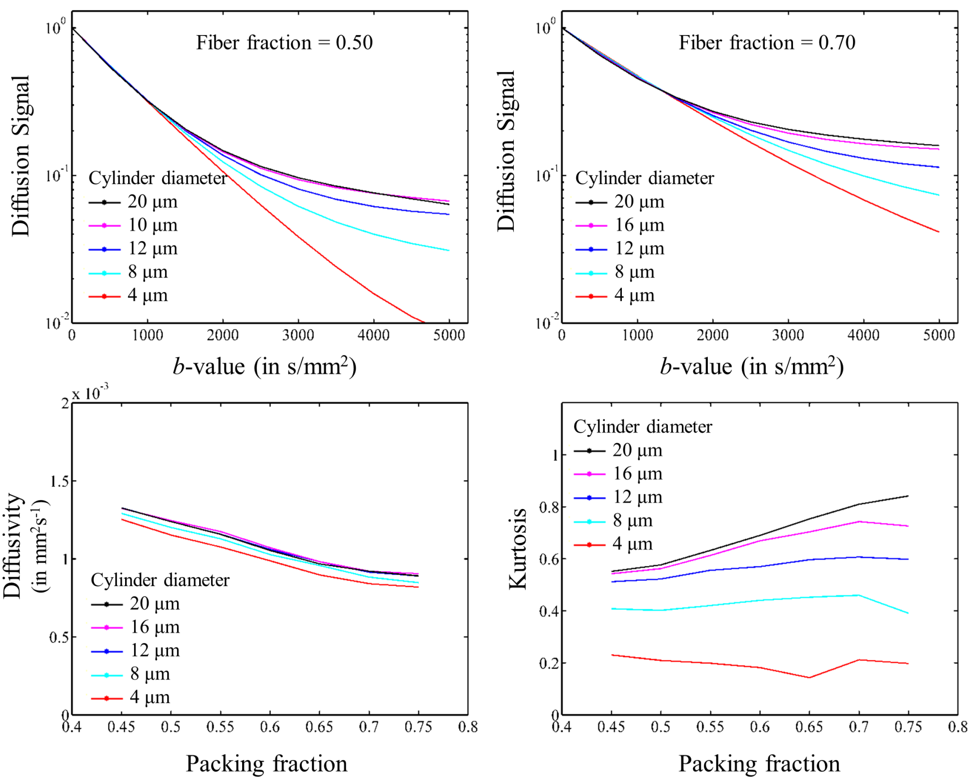

Figure 2.7: Simulated diffusion-weighted signals, diffusivity and kurtosis parameters for different cylinder diameters. Top-left: Diffusion signal for fiber fraction = 0.5; top-right: Diffusion signal for fiber fraction = 0.7, both as a function of *b*-value. Bottom-left: radial diffusivity; bottom-right: radial kurtosis, both as a function of the packing fraction.

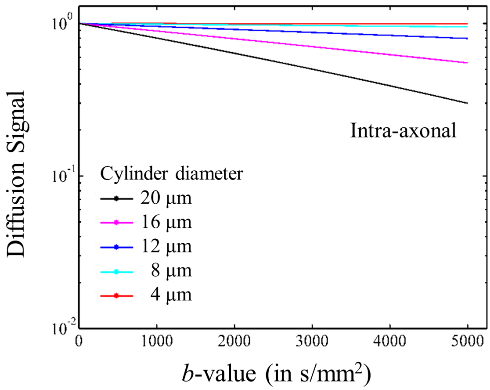

Figure 2.8: Simulated (normalized) diffusion-weighted signals as a function of *b*-value modeling diffusion inside impermeable cylinders with different diameter.

matter structures.

A limitation of our work is that our phantom consisted of fibers that are slightly thicker than the axons encountered in the brain's white matter. For instance, in the corpus callosum most axon diameters range between 0.1 µm to 2 µm [22]. Axons with diameters larger than 10 µm also exist, but are rare [22]. Our simulations suggest that particularly in white matter consisting of axons whose diameters are much smaller than typical diffusion lengths of 20-30 µm, the extracellular diffusion is adequately modeled by the Monte Carlo simulation.

Additionally, our experiments focused on the diffusion perpendicular to the fibers. We found that the axial diffusion both in our hardware phantom as well as in the simulations closely approximates free diffusion due to the highly parallel structure (data not shown). Although actual white matter has a more complex structure, reported axial diffusivities still approximate free diffusion.

Finally, probably the most important limitation of our work is in that we did not study crossing fiber structures. Essentially, we targeted to first establish the accuracy and precision of our simulations in single fiber structures with varying packing fraction. We consider simulating diffusion signals in complex structures the most important topic for our future research.

## 2.6. CONCLUSION

THE simulated MRI signals based on Monte Carlo simulations of spins subject to hindered diffusion by randomly packed cylinders accurately match the experimentally acquired data from the fiber phantom. The combined analysis of our Monte Carlo diffusion simulation and experimental data allows a more comprehensive study of the complex link between the diffusion-weighted MRI signal and the underlying microstructure.

## REFERENCES

[1] E. Stejskal and J. Tanner, *Spin diffusion measurements: spin echoes in the presence of a time-dependent field gradient,* The journal of chemical physics **42**, 288 (1965).

[2] C. Beaulieu, *The basis of anisotropic water diffusion in the nervous system–a technical review,* NMR in Biomedicine **15**, 435 (2002).

[3] P. J. Basser, J. Mattiello, and D. LeBihan, *Mr diffusion tensor spectroscopy and imaging,* Biophysical journal **66**, 259 (1994).

[4] E. Panagiotaki, T. Schneider, B. Siow, M. G. Hall, M. F. Lythgoe, and D. C. Alexander, *Compartment models of the diffusion mr signal in brain white matter: a taxonomy and comparison,* Neuroimage **59**, 2241 (2012).

[5] Y. Assaf and P. J. Basser, *Composite hindered and restricted model of diffusion (charmed) mr imaging of the human brain,* Neuroimage **27**, 48 (2005).

[6] H. Zhang, T. Schneider, C. A. Wheeler-Kingshott, and D. C. Alexander, *Noddi: practical in vivo neurite orientation dispersion and density imaging of the human brain,* Neuroimage **61**, 1000 (2012).

[7] E. Kaden, N. D. Kelm, R. P. Carson, M. D. Does, and D. C. Alexander, *Multi-compartment microscopic diffusion imaging,* NeuroImage **139**, 346 (2016).

[8] A. Szafer, J. Zhong, and J. C. Gore, *Theoretical model for water diffusion in tissues,* Magnetic resonance in medicine **33**, 697 (1995).

[9] D. C. Alexander, P. L. Hubbard, M. G. Hall, E. A. Moore, M. Ptito, G. J. Parker, and T. B. Dyrby, *Orientationally invariant indices of axon diameter and density from diffusion mri,* Neuroimage **52**, 1374 (2010).

[10] D. S. Novikov and E. Fieremans, *Relating extracellular diffusivity to cell size distribution and packing density as applied to white matter,* in *Proceedings of the 20th Annual Meeting of ISMRM, Melbourne, Victoria, Australia* (2012) p. 1829.

[11] J. Lätt, M. Nilsson, A. Rydhög, R. Wirestam, F. Ståhlberg, and S. Brockstedt, *Effects of restricted diffusion in a biological phantom: a q-space diffusion mri study of asparagus stems at a 3t clinical scanner,* Magnetic Resonance Materials in Physics, Biology and Medicine **20**, 213 (2007).

[12] S. Madi, K. M. Hasan, and P. A. Narayana, *Diffusion tensor imaging of in vivo and excised rat spinal cord at 7 t with an icosahedral encoding scheme,* Magnetic resonance in medicine **53**, 118 (2005).

[13] P. Tofts, D. Lloyd, C. Clark, G. Barker, G. Parker, P. McConville, C. Baldock, and J. Pope, *Test liquids for quantitative mri measurements of self-diffusion coefficient in vivo,* Magnetic resonance in medicine **43**, 368 (2000).

[14] C.-P. Lin, V. J. Wedeen, J.-H. Chen, C. Yao, and W.-Y. I. Tseng, *Validation of diffusion spectrum magnetic resonance imaging with manganese-enhanced rat optic tracts and ex vivo phantoms,* Neuroimage **19**, 482 (2003).

[15] K.-H. Cho, C.-H. Yeh, J.-D. Tournier, Y.-P. Chao, J.-H. Chen, and C.-P. Lin, *Evaluation of the accuracy and angular resolution of q-ball imaging,* Neuroimage **42**, 262 (2008).

[16] N. Yanasak and J. Allison, *Use of capillaries in the construction of an mri phantom for the assessment of diffusion tensor imaging: demonstration of performance,* Magnetic resonance imaging **24**, 1349 (2006).

[17] N. Shemesh, E. Özarslan, A. Bar-Shir, P. J. Basser, and Y. Cohen, *Observation of restricted diffusion in the presence of a free diffusion compartment: single-and double-pfg experiments,* Journal of Magnetic Resonance **200**, 214 (2009).

[18] M. Perrin, C. Poupon, B. Rieul, P. Leroux, A. Constantinesco, J.-F. Mangin, and D. LeBihan, *Validation of q-ball imaging with a diffusion fibre-crossing phantom on a clinical scanner,* Philosophical Transactions of the Royal Society of London B: Biological Sciences **360**, 881 (2005).

[19] E. Farrher, J. Kaffanke, A. A. Celik, T. Stöcker, F. Grinberg, and N. J. Shah, *Novel multisection design of anisotropic diffusion phantoms,* Magnetic resonance imaging **30**, 518 (2012).

[20] C. Poupon, B. Rieul, I. Kezele, M. Perrin, F. Poupon, and J. Mangin, *New diffusion phantoms dedicated to the study and validation of high-angular-resolution diffusion imaging (hardi) models,* Magnetic Resonance in Medicine **60**, 1276 (2008).

[21] E. Fieremans, Y. De Deene, S. Delputte, M. S. Özdemir, E. Achten, and I. Lemahieu, *The design of anisotropic diffusion phantoms for the validation of diffusion weighted magnetic resonance imaging,* Physics in medicine and biology **53**, 5405 (2008).

[22] F. Aboitiz, A. B. Scheibel, R. S. Fisher, and E. Zaidel, *Fiber composition of the human corpus callosum,* Brain Research **598**, 143 (1992).

[23] G. J. Stanisz, G. A. Wright, R. M. Henkelman, and A. Szafer, *An analytical model of restricted diffusion in bovine optic nerve,* Magnetic Resonance in Medicine **37**, 103 (1997).

[24] E. Fieremans, Y. De Deene, S. Delputte, M. S. Özdemir, Y. D'Asseler, J. Vlassenbroeck, K. Deblaere, E. Achten, and I. Lemahieu, *Simulation and experimental verification of the diffusion in an anisotropic fiber phantom,* Journal of Magnetic Resonance **190**, 189 (2008).

[25] F. Grinberg, E. Farrher, A. Oros-Peusquens, and N. J. Shah, *Random walks in model brain tissue,* in *AIP Conference Proceedings*, Vol. 1330 (AIP, 2011) pp. 31–34.

[26] H.-G. Lipinski, *Monte carlo simulation of extracellular diffusion in brain tissues,* Physics in medicine and biology **35**, 441 (1990).

[27] M. G. Hall and D. C. Alexander, *Convergence and parameter choice for monte-carlo simulations of diffusion mri,* Medical Imaging, IEEE Transactions on **28**, 1354 (2009).

[28] C. Liu, R. Bammer, B. Acar, and M. E. Moseley, *Characterizing non-gaussian diffusion by using generalized diffusion tensors,* Magnetic Resonance in Medicine **51**, 924 (2004).

[29] C.-H. Yeh, B. Schmitt, D. Le Bihan, J.-R. Li-Schlittgen, C.-P. Lin, and C. Poupon, *Diffusion microscopist simulator: a general monte carlo simulation system for diffusion magnetic resonance imaging,* PLOS ONE **8**, e76626 (2013).

[30] N. J. Tustison, B. B. Avants, P. A. Cook, Y. Zheng, A. Egan, P. A. Yushkevich, and J. C. Gee, *N4itk: improved n3 bias correction,* IEEE Transactions on Medical Imaging **29**, 1310 (2010).

[31] J. L. Andersson, S. Skare, and J. Ashburner, *How to correct susceptibility distortions in spin-echo echo-planar images: application to diffusion tensor imaging,* Neuroimage **20**, 870 (2003).

[32] S. M. Smith, M. Jenkinson, M. W. Woolrich, C. F. Beckmann, T. E. Behrens, H. Johansen-Berg, P. R. Bannister, M. De Luca, I. Drobnjak, and D. E. Flitney, *Advances in functional and structural mr image analysis and implementation as fsl,* Neuroimage **23**, S208 (2004).

[33] J. H. Jensen, J. A. Helpern, A. Ramani, H. Lu, and K. Kaczynski, *Diffusional kurtosis imaging: The quantification of non-gaussian water diffusion by means of magnetic resonance imaging,* Magnetic resonance in medicine **53**, 1432 (2005).

[34] M. G. Hall, G. Nedjati-Gilani, and D. C. Alexander, *Realistic voxel sizes and reduced signal variation in monte-carlo simulation for diffusion mr data synthesis,* arXiv preprint arXiv:1701.03634 (2017).

[35] P. T. Callaghan and A. Coy, *Diffraction-like effects in nmr diffusion studies of fluids in porous solids,* Nature **351**, 467 (1991).

# 3

# CSF CONTAMINATION-INVARIANT STATISTICS IN CONVENTIONAL DW-MRI OF THE FORNIX

*The goal of this chapter is to develop a method for assessment of microstructural properties of the fornix in conventional (low resolution, single non-zero b-value) diffusion-weighted MRI data. For this purpose, a bi-tensor model, comprising of an isotropic and an anisotropic diffusion compartment, was fitted to the diffusion-weighted images (DWIs). Two subject-specific constraints were studied to solve the ill-posedness of the parameter estimation at a single (non-zero) b-value, namely by fixating the mean diffusivity (MD) or the axial diffusivity (AxD) of the anisotropic compartment. The bi-tensor statistics were compared to conventional diffusion statistics using simulated fiber bundles with different diameters and using fornix segmentations of 577 elderly subjects. Based on simulated fiber bundles, the FA estimated by the bi-tensor model did not become biased with decreasing fiber bundle diameter, unlike conventional diffusion statistics such as FA and MD estimated by the single tensor model. In the population-based study, the bi-tensor tissue fraction decreased significantly with age, suggesting an increase of free water. The FA estimated by the bi-tensor model decreased with age, but this relation was not significant when the subject-specific values to which MD or AxD were constrained were added as covariates in the regression analysis. The distinction of an isotropic and an anisotropic diffusion compartment may allow a more sophisticated analysis of the fornix based on conventional DW-MRI data.*

---

G.A.M. Arkesteijn, D.H.J Poot, M. de Groot, M.A. Ikram, W.J. Niessen, L.J. van Vliet, M.W. Vernooij, and F.M. Vos, published in *Biomedical Physics & Engineering Express*, (2017), **3** 067003.

## 3.1. INTRODUCTION

DIFFUSION-WEIGHTED magnetic resonance imaging (DW-MRI) is a non-invasive imaging technique in which image contrast is determined by the (hindered) molecular diffusion of water [1]. DW-MRI is frequently used to study the brain's white matter, because the diffusion behavior of water reflects the orientation and organization of neural fibers in the white matter [2].

Diffusion tensor imaging (DTI) is a popular application of DW-MRI, in which the diffusion behavior is modeled by a rank-two diffusion tensor [3]. In voxels containing a single tissue type, DTI provides tissue-specific measures of the microstructure. However, in voxels containing different tissue classes due to partial volume effects (PVE), the diffusion tensor is influenced by all these diffusion compartments [4].

PVE complicate the analysis of diffusion-weighted images (DWIs) in two ways. Firstly, PVE make diffusivity statistics sensitive to random processes such as the positioning of the image grid. This random process yields a varying voxel composition, which causes additional noise on all diffusivity statistics, thereby decreasing the sensitivity to detect microstructural change. Secondly, PVE can introduce a bias in diffusivity statistics that depends on the size, structure and shape of the involved tracts or objects. DTI metrics such as the mean diffusivity (MD) and fractional anisotropy (FA) of the diffusion tensor may therefore be modulated by macrostructural properties such as fiber bundle thickness [5].

Cerebrospinal fluid (CSF) contamination is a partial volume effect that occurs when both CSF and tissue contribute to the signal of the same voxel. CSF is characterized by unhindered diffusivity with an apparent in-vivo diffusion coefficient approximately equal to that of free-water at 37°C [4]. The increased isotropic diffusion in CSF contaminated white matter voxels results in an overestimation of MD and an underestimation of FA. Therefore, increasing degrees of CSF contamination driven by macrostructural effects such as white matter atrophy may incorrectly suggest or exaggerate microstructural change [6]. The fornix, the primary white matter bundle connecting the hippocampus to the mammillary bodies of the hypothalamus, is particularly prone to CSF contamination due to its small size and proximity to the third and lateral ventricles [7]. Given its importance to episodic memory [8, 9] it is a good example of the challenge to disentangle the macroscopic effect of increasing CSF contamination due to aging from 'true' changes in fornix microstructure.

Different techniques can be used to limit the effects of CSF contamination. CSF contamination can be reduced during acquisition by either using a higher spatial resolution or suppressing the CSF signal with a fluid-attenuated inversion recovery (FLAIR) sequence [7, 10, 11]. However, (obviously) these methods are not be applicable to already acquired image databases applying conventional diffusion imaging protocols.

Several studies have proposed to include measures of brain atrophy or brain size as covariates in regression analyses to account for PVE by CSF. Examples are the inclusion of intracranial volume [12], brain parenchymal fraction [13], or white matter fraction [14]. However, these global measures are not necessarily optimal to correct for local effects such as CSF contamination in the fornix [15]. Local measures reflecting fornix atrophy, e.g. fornix volume or cross-sectional area, may be more appropriate to correct for CSF contamination in the fornix. However, such corrections cannot easily take morphological properties into account, such as fiber bundle shape, orientation or curvature, which may also modulate DTI metrics [5].

Preferably, CSF contamination is corrected on a voxel-by-voxel basis by explicitly modeling the contribution of CSF in the DW-MRI signal [15]. A model-based approach for CSF decontamination using a two-compartment tensor model was proposed in [16]. Ideally, the intra-axonal and extra-cellular water in the tissue microstructure are also modeled with separate diffusion compartments such that the overall system is modeled as a three-compartment system (intra-axonal, extra-cellular and CSF) [17]. However, for a stable fit of these models, the diffusion-weighted images (DWIs) have to be acquired with multiple diffusion weightings ($b$-values) [18, 19] at the expense of a longer imaging time. Unfortunately, in many datasets of interest (such as the ADNI data [20] or the Rotterdam Scan Study [21]) the diffusion data has already been acquired using a conventional single (non-zero) $b$-value acquisition protocol.

In case of single (non-zero) $b$-value DWIs, the fit of a simple two-compartment model is ill-posed. Prior work has attempted to make the estimation problem well-posed by spatially regularizing the diffusion tensor of the anisotropic compartment [18]. However, recent work has shown that such a spatial regularization does not actually alleviate the degeneracy of the estimation problem [22]. To make the estimation well-posed, a later work globally constrained the mean diffusivity (MD) of the anisotropic compartment [23]. This approach resulted in statistics with a reduced sensitivity to PVE with CSF. However, a limitation of this work was that a global constraint may not be appropriate for every subject, which in turn may introduce an estimation bias.

The goal of this chapter is to develop a method for assessment of structural properties of the fornix in conventional (low resolution, single non-zero $b$-value) diffusion-weighted MRI data. In particular, the method targets analysis of diffusion data from a large population study [24]. Instead of using global (population-averaged) constraints to make estimation of a two-compartment model feasible as in [23], we use subject-specific constraints on the AxD or MD of the anisotropic compartment. We provide an extensive evaluation by investigating the macrostructural dependence of conventional and proposed diffusion statistics using in-silico simulation. Furthermore, the reproducibility of conventional as well as proposed diffusion statistics is determined on 20 subjects for whom rescan data was available. Finally, the effects of ageing on both conventional and proposed diffusion statistics of the fornix are investigated on a large (population) dataset of 577 subjects.

## 3.2. METHODS

### 3.2.1. BI-TENSOR MODEL

We use a bi-tensor representation to model the DW-MRI data [18]. A more advanced approach using a three-compartment model (intra-axonal water, extra-cellular water and CSF) as in [17] is not feasible with our data. The bi-tensor representation assumes a CSF-contaminated voxel to consist of two diffusion compartments: a tissue compartment and a CSF compartment. The diffusion signal originating from these compartments can be modeled as a weighted sum of both diffusion signals. The diffusion in the tissue compartment is assumed to be Gaussian. The water in the CSF compartment is expected to diffuse freely, which at 37°C can be modeled by an isotropic diffusion tensor with eigenvalues equal to $d_{\text{CSF}} = 3.0 \cdot 10^{-3}$ mm$^2$/s. The bi-tensor signal model is formulated as:

$$S_{b,\mathbf{g}} = S_0\Big(f \exp\big(-b\mathbf{g}^T\mathbf{D}\mathbf{g}\big) + (1-f)\exp\big(-bd_{\text{CSF}}\big)\Big), \tag{3.1}$$

where $b$ is the experimental parameter that represents the amount of diffusion-weighting, $\mathbf{g}$ is a unit vector that specifies the direction of a diffusion-encoding gradient pulse, $S_0$ is the volume-weighted average of the non-diffusion weighted signals from the CSF and tissue compartment, $f$ and $(1-f)$ are the signal fractions of the tissue and CSF compartments respectively, and $\mathbf{D}$ is the diffusion tensor of the tissue compartment. When the DWIs have been acquired at two or more different (non-zero) $b$-values, the unknown parameters $S_0$, $f$ and $\mathbf{D}$ can be estimated by minimizing a distance function between the model and the measured diffusion signal. However, when the DWIs have been acquired at a single $b$-value, different combinations of $f$ and $\mathbf{D}$ exist that result in the same predicted diffusion signal. This makes the inverse problem of estimating the unknown parameters ill-posed.

### 3.2.2. CSF CONTAMINATION-INVARIANT STATISTICS

The degenerate $(f, \mathbf{D})$ pairs can be found by setting the tissue fraction $f$ to different values in the interval from 0 to 1, while estimating the remaining unknown parameters by fitting equation 3.1 to the observed data. Let $\Omega$ be the set of all positive-definite diffusion tensors $\mathbf{D}$ that are obtained as such. The degenerate set $\Omega$ can be visualized by, for instance, plotting the FA against the MD for all diffusion tensors in $\Omega$ (example in figure 1A), or by plotting the FA versus the axial diffusivity (AxD) (example in figure 1B). Figure 3.1A illustrates how the exact same signal profile can be obtained by reducing the FA and increasing the MD of tensor $\mathbf{D}$; at the same time the volume fraction of the isotropic part $(1-f)$ decreases for compensation (not shown in the figure). Alternatively, figure 3.1B shows how an identical signal profile is obtained by lowering FA and increasing AxD, also at a simultaneously lower $(1-f)$. Unfortunately, without additional information, the true diffusion tensor modeling the tissue compartment cannot be reconstructed.

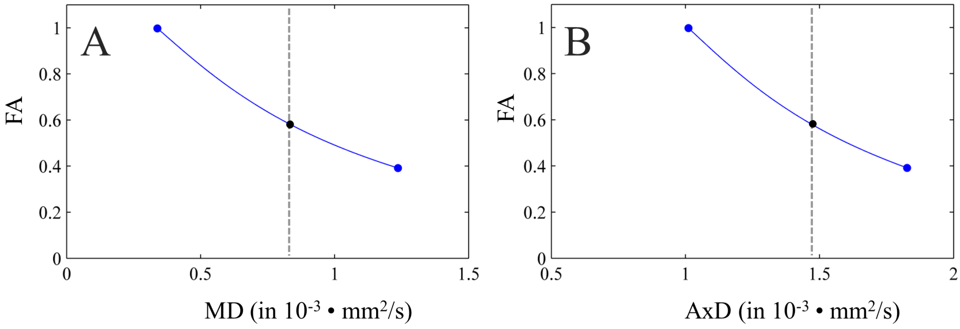

Figure 3.1: Visualization of a degenerate set of diffusion tensors. A) FA versus the mean diffusivity (MD) of the diffusion tensor. B) FA versus the axial diffusivity (AxD) of the diffusion tensor. The introduction of a constraint, e.g. on the MD or the AxD, allows a single diffusion tensor from this degenerate set to be constructed.

To better characterize the true diffusion tensor **D**, we will study two different approaches to select a tensor from a degenerate set. In the first approach, we select a tensor with a fixed MD; in the second approach, we select a tensor with a fixed AxD. In figure 3.1 it is illustrated how both approaches select a unique diffusion tensor from the degenerate set, and hence yield a well-posed estimation problem. It should be noted that these tensors can be efficiently computed by constraining the diffusion tensor during the fitting of the model. In previous work, a global value (same for all subjects) of $8.0 \cdot 10^{-3}$ mm$^2$/s was used as a constraint for the MD [23]. We now propose to compute representative subject-specific constraints for the MD and the AxD derived from single tensor fits in the splenium of the corpus callosum of the particular subject.

Clearly, imposing such constraints on the model is generally not preferred as it precludes the representation of certain variations in diffusion parameters. Even more, the constraints are not required with data acquired at multiple $b$-values or may be avoided with FLAIR DT imaging. However, these solutions are not applicable to conventional diffusion data collected on a single shell such as ours (see below). A motivation for the constraints is illustrated in figure 3.2. It displays the AxD (figure 3.2A), radial diffusivity (figure 3.2B) and MD (figure 3.2C) in a white matter segmentation of the brain of a 65-years old male. The histogram in figure 3.2D demonstrates that the MD shows the smallest coefficient of variation across the white matter, which suggests that it may be a suitable constraint. However, assuming a fixed MD in the body of the fornix may not always be appropriate. We therefore also explore constraining the AxD, such that both the FA and MD in the bi-tensor model can vary across the fornix.

Summarizing, the first constraint assumes a single, fixed MD that may differ per subject, without any further restriction on FA. The second constraint assumes a single, fixed AxD, per subject, without further restrictions on both MD and FA. Subscripts will be used to discriminate between diffusion statistics obtained with different approaches, e.g. $\mathrm{FA}_{\mathrm{MD}}$ refers to the FA of a bi-tensor model with constrained MD and $\mathrm{FA}_{\mathrm{AxD}}$ refers to the FA of a bi-tensor model with constrained AxD. Bi-tensor statistics obtained with a global MD-constraint of $8.0 \cdot 10^{-3}$ mm$^2$/s will be denoted with the subscript 'MD,Glob', e.g. $\mathrm{FA}_{\mathrm{MD,Glob}}$. Conventional single tensor statistics will be denoted with the subscript 'ST', e.g. $\mathrm{FA}_{\mathrm{ST}}$ or $\mathrm{MD}_{\mathrm{ST}}$.

### 3.2.3. PARAMETERIZATION OF THE BI-TENSOR MODEL

To enforce the constraints, the tissue diffusion tensor **D** in equation 3.1 is parameterized by a rotation matrix **R** and an eigenvalue matrix **E**, i.e. $\mathbf{D} = \mathbf{R}\mathbf{E}\mathbf{R}^T$. The rotation matrix **R** is a concatenation of three rotations about the $x$-, $y$- and $z$-axes, e.g. $\mathbf{R} = \mathbf{R}_x(\alpha_1)\mathbf{R}_x(\alpha_2)\mathbf{R}_x(\alpha_3)$. The MD-constraint is enforced by parameterizing the eigenvalues of the diagonal matrix **E** as follows:

$$\lambda_1 = 3C_1C_{\mathrm{MD}} \tag{3.2}$$

$$\lambda_2 = 3(1-C_1)C_2C_{\mathrm{MD}} \tag{3.3}$$

$$\lambda_3 = 3(1-C_1)(1-C_2)C_{\mathrm{MD}} \tag{3.4}$$

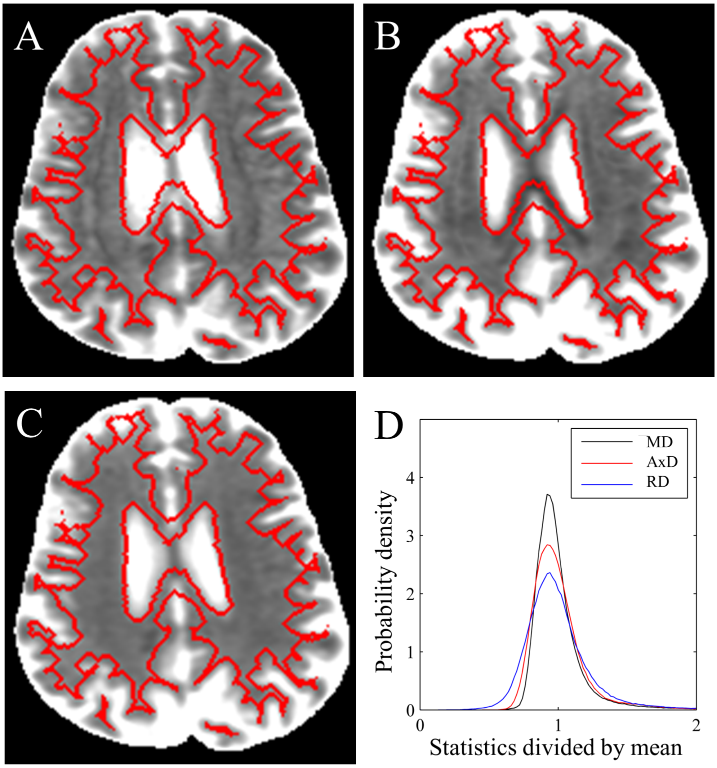

Figure 3.2: Transversal slices from an asymptomatic 65-years old male brain with contours of a white matter segmentation in red. The white matter segmentation was obtained using a kNN tissue segmentation method [25]. A) Axial diffusivity (AxD). B) Radial diffusivity (RD). C) Mean diffusivity (MD) of the diffusion tensor. The images are scaled between zero and two times the mean value of each diffusivity statistic. The mean values of AxD, RD and trace are computed from all voxels in the whole-brain white matter segmentation and are $1.1 \cdot 10^{-3}$ mm$^2$/s, $0.69/cdot10^-3$ mm$^2$/s and $0.83 \cdot 10^{-3}$ mm$^2$/s respectively. D) Histograms of the AxD, RD and trace after dividing each statistic by its mean value.

where $C_{\mathrm{MD}}$ is the value of the MD constraint and $C_1$ and $C_2$ are unknown parameters between 0 and 1. In case of the AxD-constraint, the parameterization is as follows:

$$\lambda_1 = C_{\mathrm{AxD}} \tag{3.5}$$

$$\lambda_2 = C_1 C_{\mathrm{AxD}} \tag{3.6}$$

$$\lambda_3 = C_2 C_{\mathrm{AxD}} \tag{3.7}$$

where $C_{\mathrm{AxD}}$ is the value of the AxD-constraint and $C_1$ and $C_2$ are again unknown parameters between 0 and 1. In both parametrizations $C_1$ and $C_2$ can be constrained during model fitting by an constrained optimization routine.

### 3.2.4. FIBER BUNDLE SIMULATIONS

Phantom fiber bundles were simulated in order to have a reference standard for assessment of features extracted from the single-tensor model and the proposed bi-tensor models. The Numeric Fiber Generator (NFG) v1.1.1 [26] was used to simulate sets of DWIs. Each set contained a single cylindrically shaped white matter fiber bundle of approximately 60 mm in length, with an arbitrary orientation. Diameters of the white matter fiber bundles were varied from 3 mm to 12 mm in steps of 1.5 mm. Three different microstructures were simulated with respectively FA=$\{0.75, 0.80, 0.85\}$, MD=$\{0.85, 0.80, 0.80\} \cdot 10^{-3}$ mm$^2$/s and AxD=$\{1.78, 1.78, 1.89\} \cdot 10^{-3}$ mm$^2$/s. The white matter bundles were completely surrounded by CSF, which was modeled as an isotropic compartment with a diffusivity of $3.0 \cdot 10^{-3}$ mm$^2$/s. The $b_0$-intensity of CSF, i.e. imaged at $b$-value = 0 s/mm$^2$, was set to three times the $b_0$-intensity of the white matter compartment. Acquisition parameters were set to approximately match the acquisition in the Rotterdam Study [21]: 25 gradient directions and a $b$-value of 1000 s/mm$^2$. PVEs were introduced in the boundary voxels of the fiber bundles, by first generating the DW-MRI signal on a fine imaging grid with a resolution of (0.15 mm)$^3$ and then summing the signal of each subvoxel element into a coarser voxel grid with a resolution of (3 mm)$^3$. Finally, Rician distributed data with an SNR of 20 (in the white matter in the $b_0$-image) were created from the simulated noise-free DWIs. Fiber bundle segmentations were created by including all voxels overlapping the (ground truth) fiber bundle. For each combination of diameter and microstructure, the simulations were conducted ten times such that a mean and standard deviation of relevant diffusion statistics could be computed.

### 3.2.5. STUDY POPULATION

Imaging data from the population-based Rotterdam Study was also used to evaluate the proposed framework [24]. The reproducibility of the framework was tested on 20 subjects for whom rescan data (MRI scans acquired on the same scanner) was available (see also [27]). The mean time between the baseline scan and rescan was 19.5 days (SD 10). These subjects were on average 76.7 (SD 4.8) years old, 50% was female. The framework was further evaluated on a group of 671 subjects, sampled from a cohort of the Rotterdam Study, such that an age distribution from 63 to 80 years was obtained. Due to missing or incorrect fornix segmentations 94 subjects were excluded, as explained below. As such 577 subjects remained: 279 males and 298 females. Ages ranged from 63.9 to 80.0 years, with mean age 69.3 (SD 3.5) years. None of the subjects was diagnosed with dementia. Written informed consent was obtained from all participants.

### 3.2.6. DATA ACQUISITION

Subjects were scanned on a 1.5 tesla MRI scanner (GE Signa Excite) using an 8-channel head coil. DWIs were acquired with a single shot, diffusion-weighted spin echo echo-planar imaging sequence (repetition time (TR) = 8575 ms, echo time (TE) = 82.6 ms, field of view (FOV) = 210 mm x 210 mm, imaging matrix = 96x64 (zero-padded to 256x256), 35 contiguous slices of slice thickness 3.5 mm) in 25 non-collinear directions with a maximum $b$-value of 1000 s/mm$^2$. Three volumes were acquired without diffusion weighting (the $b_0$-images). Additionally, structural images were acquired including a T1-weighted sequence [21].

### 3.2.7. DIFFUSION-IMAGE PROCESSING

The acquired DWIs were corrected for motion and eddy current distortion by affine coregistration to the reference $b_0$-image with Elastix [28]. Together with the affine transformation, DWIs were upsampled to a 1.0 mm isotropic resolution. Simultaneously, upsampling the image data has little additional adverse effects, but does yield images that are easier to inspect visually for potential artefacts or accurate coregistration. Gradient directions were reoriented according to the rotation component of the affine transformation to maintain correspondence during registration [29]. Next, the single-tensor model, bi-tensor model with global MD-constraint, bi-tensor model with subject-specific MD-constraint and bi-tensor model with subject-specific AxD-constraint were fitted to the DWIs using the fit_MRI toolbox [30] by maximum likelihood estimation assuming Rician distributed data [31].

### 3.2.8. CORPUS CALLOSUM SEGMENTATION

A segmentation of the splenium of the corpus callosum was applied to obtain a region-of-interest to compute the MD and AxD constraints. For this purpose the Johns Hopkins University (JHU) DTI atlas was registered to the FA images of each subject using a non-rigid transformation with `fnirt`, a non-linear registration tool in FSL. The JHU white matter labels, including the splenium of the corpus callosum, were then warped to each subject space using nearest neighbor interpolation. The median MD and AxD of a single tensor fit in the splenium of the corpus callosum segmentation were used as constraints in the fitting of the constrained bi-tensor models.

### 3.2.9. FORNIX SEGMENTATION

Conventional and proposed diffusion statistics of the fornix were compared across subjects. The fornix shows large anatomical variation across different subjects, which hinders accurate registration [32]. As such, a straightforward voxel-based analysis of the fornix in a common (atlas) space was not possible with our data. We therefore chose a region-of-interest based approach in subject space, and used FreeSurfer v5.1 software [33] to segment the fornix based on T1-weighted images combined with a probabilistic atlas. The FreeSurfer segmentations of the fornix were preferred over tractography segmentations based on the (low-resolution) DWIs, because the higher spatial resolution of the T1-weighted images enabled a more accurate segmentation. Indeed, tractography based segmentations as applied in [34, 35] largely failed for our data, due to the low resolution of the DWIs. The FreeSurfer segmentation of the fornix typically contains the body of the fornix (see figure 3.3A and B). However, approximately 15% of the fornix segmentations also erroneously included large parts of the corpus callosum (figure 3.3C). The corpus callosum was removed from the fornix segmentations using binary morphology operations as follows. A mask was created by applying a three-dimensional closing operation with a spherical structure element (radius of 4 mm) to the third and lateral ventricles (figure 3.3D). The largest N6-connected structure within this mask was kept as fornix.

To align the fornix segmentation with the DWIs, a transformation was computed by rigidly coregistering the T1-weighted scan to the $b_0$-image using `flirt`, a linear registration tool in FSL. However, echo-planar imaging (EPI) acquisitions are very sensitive

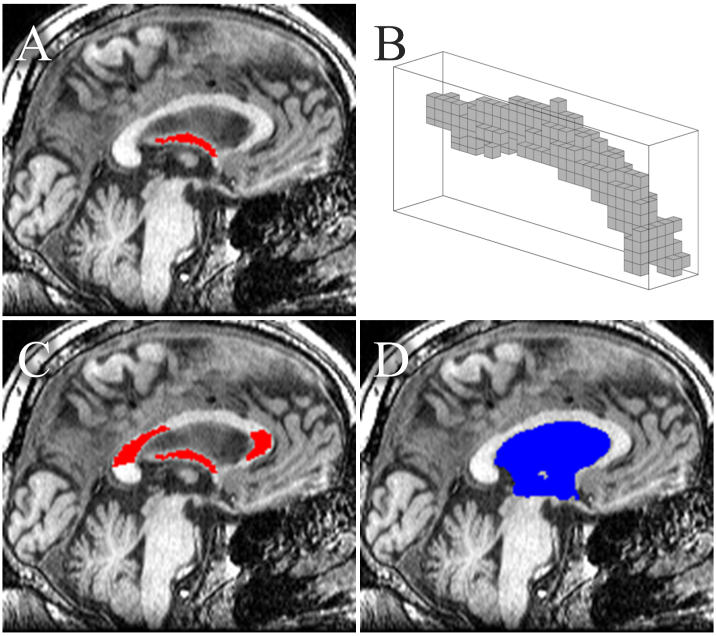

Figure 3.3: A) Sagittal slice of a fornix segmentation with T1w background image. B) Three-dimensional view of a fornix segmentation. Each cube is a (1 mm)$^3$ voxel. C) FreeSurfer segmentations of the fornix sometimes erroneously included parts of the corpus callosum, D) A three-dimensional closing operation applied to the third and lateral ventricles provided a mask that was used to exclude the corpus callosum from fornix segmentations.

to static magnetic field inhomogeneities. Variations in the static magnetic field, particularly at air-tissue interfaces, induce geometric distortions in the $b_0$-image due to the EPI readout. A straightforward rigid registration tends to slightly misalign the fornix to correct for geometric distortions elsewhere in the brain. This misalignment was prevented by using a smoothed FreeSurfer segmentation of the third and lateral ventricles as a weighting image for the cost function in `flirt`. Essentially, this emphasized accurate registration of the region around the fornix. All fornix segmentations were inspected and 94 out of 671 subjects with missing or incorrect fornix segmentations were removed from the study. More specifically; in 17 subjects FreeSurfer crashed, in 61 subjects FreeSurfer did not label a single voxel as fornix, and in 16 subjects the fornix segmentation contained major defects.

## 3.3. RESULTS

### 3.3.1. EXAMPLE OF A TYPICAL SUBJECT

A typical result for a 65-year old brain is displayed in figure 3.4. Figure 3.4A shows a coronal slice of a T1-weighted scan with the fornix segmentation in red. The small size of the fornix can be appreciated, e.g. even the body the thickest part of the fornix, is only 4-5 mm in diameter. In figure 3.4B, C, D and E, the $FA_{ST}$, $MD_{ST}$, $FA_{MD}$ and $f_{MD}$ are shown respectively. For visualization purposes voxels with tissue fraction $f_{\text{MD}}$ smaller than 0.3 have been masked black in figure 3.4D. In these voxels the MRI signal from the tissue compartment is too small for reliable estimation of $\text{FA}_{\text{MD}}$. Furthermore, observe that the image contrast provided by $\text{MD}_{\text{ST}}$ is approximately the inverse of the image contrast provided by $f_{\text{MD}}$. Due to the constraint in the bi-tensor model, any increase in the mean diffusivity in a voxel is explained by a decrease in $f_{\text{MD}}$.

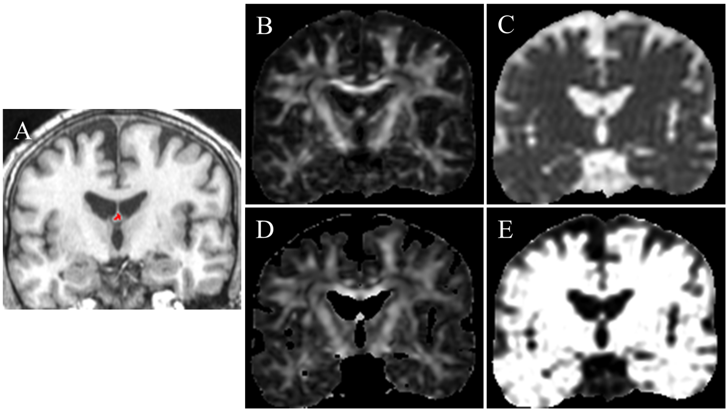

Figure 3.4: Coronal slices from an asymptomatic 65-year old male brain. A) T1w-image with fornix segmentation in red. B) $\text{FA}_{\text{ST}}$. C) $\text{MD}_{\text{ST}}$. D) $\text{FA}_{\text{MD}}$ (voxels with $f_{\text{MD}}$<0.3 have been masked black). E) $f_{\text{MD}}$.

### 3.3.2. SIMULATED FIBER BUNDLES

The segmented voxels in the simulated fiber bundle are affected by various degrees of CSF contamination, e.g. boundary voxels are typically more contaminated than center voxels. The effects of CSF contamination can be reduced by excluding the most contaminated voxels from the analysis. We therefore considered three (arbitrarily chosen) levels of contamination at which to extract diffusivity statistics from the segmentations, by computing an average over all voxels, over the 50% least contaminated voxels, and over the 10% least contaminated voxels. The ground truth degree of CSF contamination in each voxel was computed from the (noiseless) $b_0$-image.

Using the three exclusion levels, the FA and MD of a single tensor model ($\text{FA}_{\text{ST}}$ and $\text{MD}_{\text{ST}}$) as well as the FA and tissue fraction $f$ of the bi-tensor model with constrained MD ($\text{FA}_{\text{MD}}$ and $f_{\text{MD}}$) and constrained AxD ($\text{FA}_{\text{AxD}}$ and $f_{\text{AxD}}$), are plotted against the diameter of the simulated fiber bundles in figure 3.5. The shaded areas along the plotted curves represent two standard errors around the mean values. The constraints were set to $C_{\text{MD}} = 0.8 \cdot 10^{-3}$ mm$^2$/s and $C_{\text{AxD}} = 1.78 \cdot 10^{-3}$ mm$^2$/s in respectively the MD constrained and AxD constrained bi-tensor model. Note that the ground truth values in the simulated fiber bundle has an FA of 0.8.

It can be observed that conventional diffusion statistics ($\text{FA}_{\text{ST}}$ and $\text{MD}_{\text{ST}}$) and the bi-tensor tissue fractions ($f_{\text{MD}}$ and $f_{\text{AxD}}$) become increasingly biased with decreasing simulated fiber diameter and with higher percentages of contaminated voxels included. Obviously, computing the average from the 10% least contaminated voxels yields the smallest bias with respect to the simulated ground truth. At this exclusion level, the extracted $\mathrm{FA}_{\mathrm{ST}}$ and $\mathrm{MD}_{\mathrm{ST}}$ are almost equal to their simulated ground truth in fiber bundles with diameters larger than 9 mm (i.e. three times the voxel size). This is not the case in fiber bundles with smaller diameters, or when the average is computed from the more contaminated voxels in the tract segmentations. Furthermore, the CSF contamination introduces a relatively large uncertainty in the estimated conventional diffusion statistics ($\mathrm{FA}_{\mathrm{ST}}$ and $\mathrm{MD}_{\mathrm{ST}}$) and the bi-tensor tissue fractions ($f_{\mathrm{MD}}$ and $f_{\mathrm{AxD}}$).

The mean CSF contamination-invariant statistics $\mathrm{FA}_{\mathrm{MD}}$ and $\mathrm{FA}_{\mathrm{AxD}}$ appear independent of fiber bundle diameter and the used exclusion level and are approximately equal to the simulated ground truth. In the smallest fiber bundle the uncertainties in estimated $\mathrm{FA}_{\mathrm{MD}}$ and $\mathrm{FA}_{\mathrm{AxD}}$ are a little larger than ten percent of the ground truth. This can be explained by a smaller region-of-interest over which these statistics are computed, and (on average) a smaller fraction of the signal that originates from the tissue compartment in each voxel. Furthermore, the variation in $\mathrm{FA}_{\mathrm{AxD}}$ appears larger than the variation in $\mathrm{FA}_{\mathrm{MD}}$. Subsequently, the ability to discriminate between fiber bundle configurations with varying FA was evaluated using the 10% and 50% least contaminated voxels. For fiber bundles with different simulated FA values (0.75, 0.8 and 0.85), conventional and proposed diffusion statistics are plotted against the diameter in figure 3.6. The overlapping confidence bounds of $\mathrm{FA}_{\mathrm{ST}}$ for bundles smaller than 9.0 mm as well as the dependency of $\mathrm{FA}_{\mathrm{ST}}$ on bundle diameter imply that bundles with these differences in FA cannot be distinguished. In fiber bundles with diameters of 6.0 mm and larger, the variance in both $\mathrm{FA}_{\mathrm{MD}}$ and $\mathrm{FA}_{\mathrm{AxD}}$ is sufficiently small to discriminate between the three simulated FA's.

In figure 3.6 the effect of a mismatch between the applied constraints and the ground truth can be observed. The fiber bundle with true FA = 0.75 has true MD= $0.85 \cdot 10^{-3}$ $\mathrm{mm}^2/\mathrm{s}$, whereas the applied MD-constraint was $C_{\mathrm{MD}} = 0.80 \cdot 10^{-3}$ $\mathrm{mm}^2/\mathrm{s}$. In the second column of figure 3.6 it is shown that in this case the $\mathrm{FA}_{\mathrm{MD}}$ slightly overestimates the true FA by approximately 5%. Observe, however, that despite the bias, the mean $\mathrm{FA}_{\mathrm{MD}}$ is still independent of fiber diameter. Similarly, the fiber bundle with true FA=0.85 has true AxD= $1.89 \cdot 10^{-3}$ $\mathrm{mm}^2/\mathrm{s}$, whereas the applied AxD-constraint was $C_{\mathrm{AxD}} = 1.78 \cdot 10^{-3}$ $\mathrm{mm}^2/\mathrm{s}$. In the third column of figure 3.6 it can be observed that $\mathrm{FA}_{\mathrm{AxD}}$ slightly overestimates the true FA in this situation by about 5%.

### 3.3.3. REPRODUCIBILITY STUDY

As demonstrated in the simulations, excluding the most contaminated voxels from the segmentation is a straightforward method to reduce the effects of CSF contamination. Unfortunately the ground-truth contamination level is not known for our clinical datasets. Instead, we selected the 10% and 50% voxels with the highest $\mathrm{FA}_{\mathrm{ST}}$ in the fornix segmentation of our clinical datasets.

On twenty subjects for whom rescan data was available, we evaluated the reproducibility of parameter estimation. Baseline and follow-up scans were processed using the described processing pipeline. The mean $\mathrm{FA}_{\mathrm{ST}}$, $\mathrm{MD}_{\mathrm{ST}}$, $\mathrm{FA}_{\mathrm{MD,Glob}}$, $\mathrm{FA}_{\mathrm{MD}}$, $\mathrm{FA}_{\mathrm{AxD}}$, and tissue fractions $f_{\mathrm{MD,Glob}}$, $f_{\mathrm{MD}}$ and $f_{\mathrm{AxD}}$ in the 10% and 50% highest $\mathrm{FA}_{\mathrm{ST}}$ voxels of the fornix were computed for both scans of all twenty subjects. For all diffusion statistics, Bland-Altman plots showing the difference between the time point measurements

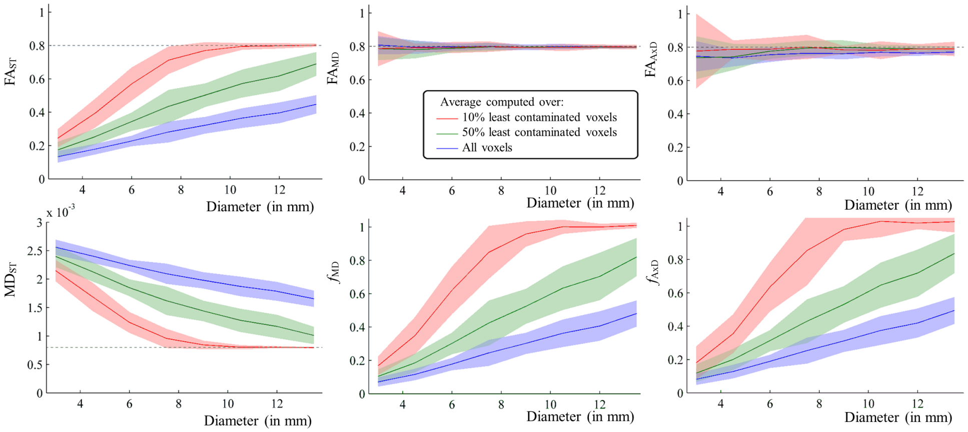

Figure 3.5: Effect of selecting the least contaminated voxels within tract segmentations of CSF-contaminated fiber bundles. Diffusion properties from single fiber bundle configurations with FA=0.8 and different fiber bundle diameters were estimated with the single-tensor model (left column), the bi-tensor model with constrained mean diffusivity (middle column), and the bi-tensor model with constrained axial diffusivity (right column). Diffusivity statistics were extracted by taking an average over all voxels (blue), over the 50% least contaminated voxels (green), and over the 10% least contaminated voxels (red). The shaded areas represent two standard errors around the mean values; the grey dashed lines represent the simulated ground truth.

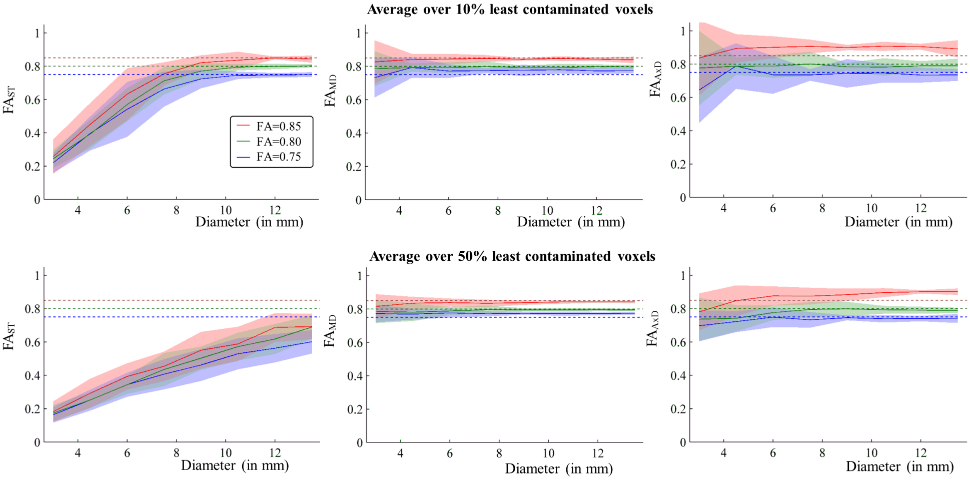

Figure 3.6: Impact of CSF contamination on fiber bundle configurations with varying diameters and FA. Diffusion properties from single fiber bundle configurations with different FA and different diameters were estimated with the single-tensor model (left column), the bi-tensor model with constrained mean diffusivity (middle column), and the bi-tensor model with constrained axial diffusivity (right column). Diffusivity statistics were computed by taking an average over the 10% least contaminated voxels (top row), or over the 50% least contaminated voxels (bottom row). The shaded areas represent two standard errors around the mean values; the colored dashed lines represent the simulated ground truth.

as function of the mean are presented in figure 3.7. Diffusion statistics computed from the 10% highest $\mathrm{FA}_{\mathrm{ST}}$ voxels are displayed in red, diffusion statistics computed from the 50% highest $\mathrm{FA}_{\mathrm{ST}}$ voxels are displayed in blue. The coefficients of repeatability (CR), defined as the 1.96 times the standard deviation of the differences between the two measurements are also reported in figure 3.7. For all diffusion statistics the coefficient of repeatability (CR) is smallest when the 50% highest $\mathrm{FA}_{\mathrm{ST}}$ voxels are used, but including more contaminated voxels also decreases the mean $\mathrm{FA}_{\mathrm{ST}}$ and increases $\mathrm{MD}_{\mathrm{ST}}$, while $f_{\mathrm{MD}}$ and $f_{\mathrm{AxD}}$ both decrease.

### 3.3.4. AGEING STUDY

Figure 3.8 shows scatter plots of the estimated $\mathrm{FA}_{\mathrm{ST}}$, $\mathrm{MD}_{\mathrm{ST}}$, $\mathrm{FA}_{\mathrm{MD,Glob}}$, $\mathrm{FA}_{\mathrm{MD}}$, $\mathrm{FA}_{\mathrm{AxD}}$, $f_{\mathrm{MD,Glob}}$, $f_{\mathrm{MD}}$ and $f_{\mathrm{AxD}}$ in the body of the fornix versus age. Linear regression lines with age were computed for all diffusion statistics. Red points and regression lines represent statistics computed from the 10% highest $\mathrm{FA}_{\mathrm{ST}}$ voxels, blue points and regression lines represent statistics computed from the 50% highest $\mathrm{FA}_{\mathrm{ST}}$ voxels. The regression-coefficients of these lines and their p-values are reported in table 3.1. All regression coefficients are significantly different from zero, both for the statistics computed from the 10% and 50% highest $\mathrm{FA}_{\mathrm{ST}}$ voxels.

Observe that diffusion statistics $\mathrm{FA}_{\mathrm{ST}}$, $\mathrm{FA}_{\mathrm{MD}}$ and $\mathrm{FA}_{\mathrm{AxD}}$ all decrease with age, whereas $\mathrm{FA}_{\mathrm{MD,Glob}}$ increases with age (with a very small slope). Furthermore, $\mathrm{MD}_{\mathrm{ST}}$ increases with age and the tissue fractions $f_{\mathrm{MD,Glob}}$, $f_{\mathrm{MD}}$ and $f_{\mathrm{AxD}}$ all decrease with age. For conventional diffusion statistics (i.e. $\mathrm{FA}_{\mathrm{ST}}$ and $\mathrm{MD}_{\mathrm{ST}}$) and bi-tensor tissue fractions $f_{\mathrm{MD,Glob}}$, $f_{\mathrm{MD}}$ and $f_{\mathrm{AxD}}$, a clear difference can be observed between the statistics computed from the 10% and 50% highest $\mathrm{FA}_{\mathrm{ST}}$ voxels. A paired sample t-test confirmed these differences were all significant with p-values smaller than $1 \cdot 10^{-10}$. The diffusion statistics $\mathrm{FA}_{\mathrm{MD,Glob}}$, $\mathrm{FA}_{\mathrm{MD}}$ and $\mathrm{FA}_{\mathrm{AxD}}$ provide similar values in the 10% and 50% highest $\mathrm{FA}_{\mathrm{ST}}$ voxels.

The MD and the AxD of the splenium of the corpus callosum were used as constraints in the bi-tensor model. Scatter plots of MD and AxD in the splenium versus age have been visualized in figure 3.9. For both statistics the linear regression line with age increases significantly. To investigate whether this increase explains the observed changes in the fornix, we included the MD of the splenium as a covariate in our regression analysis of $\mathrm{FA}_{\mathrm{MD}}$ and $f_{\mathrm{MD}}$ with age. In a similar fashion the AxD of the splenium was included in our regression analysis of $\mathrm{FA}_{\mathrm{AxD}}$ and $f_{\mathrm{AxD}}$ with age. The results are reported in table 3.1. Here it can be seen that after correction the bi-tensor tissue fractions $f_{\mathrm{MD}}$ and $f_{\mathrm{AxD}}$ still decrease significantly with age. However, both $\mathrm{FA}_{\mathrm{MD}}$ and $\mathrm{FA}_{\mathrm{AxD}}$ no longer correlate significantly with age, except for $\mathrm{FA}_{\mathrm{MD}}$ that increases with age when computed from the 50% highest $\mathrm{FA}_{\mathrm{ST}}$ voxels (although the slope is rather small).

## 3.4. DISCUSSION

We have presented and evaluated a framework that can be used to compute CSF contamination-invariant statistics in the body of the fornix from conventionally acquired DWIs.

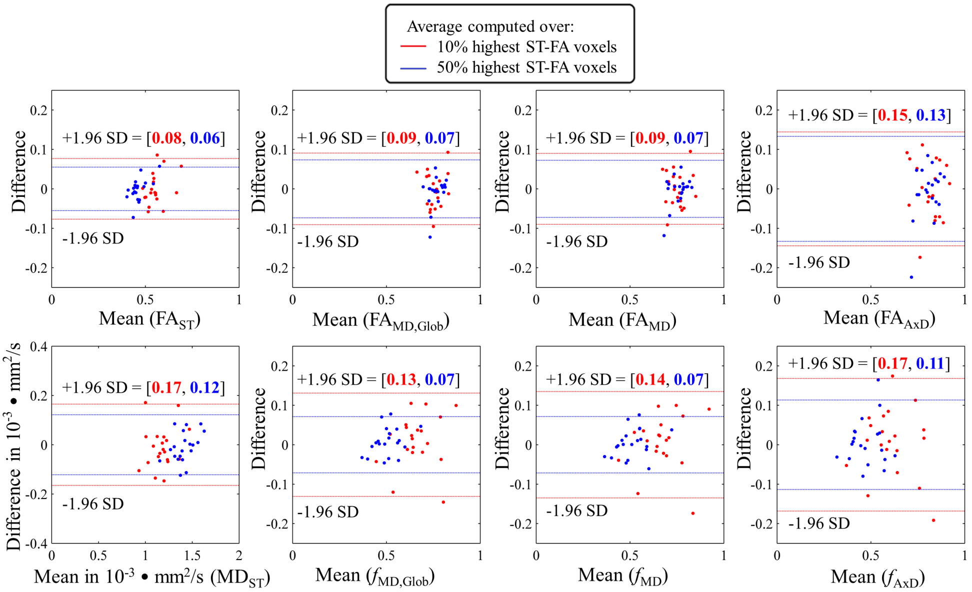

Figure 3.7: Bland-Altman plots show the repeatability of estimating the mean $FA_{ST}$, $MD_{ST}$, $FA_{MD,Glob}$, $FA_{MD}$, $FA_{AxD}$, and tissue fractions $f_{MD,Glob}$, $f_{MD}$ and $f_{AxD}$ from the 10% highest (in red) or the 50% highest (in blue) $FA_{ST}$ voxels in the fornix. The diffusivity statistics were estimated from baseline and follow-up scans in twenty subjects of the Rotterdam Study for whom rescan data was available.

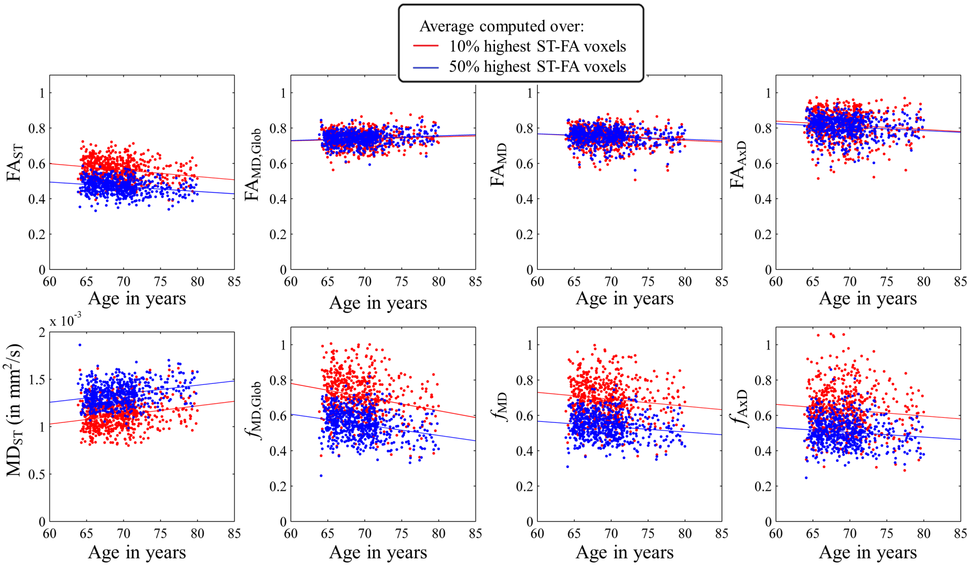

Figure 3.8: Scatter plots of diffusion statistics $FA_{ST}$, $MD_{ST}$, $FA_{MD,Glob}$, $FA_{MD}$, $FA_{AxD}$, $f_{MD,Glob}$, $f_{MD}$ and $f_{AxD}$ versus age for 577 subjects of the Rotterdam Study. Statistics computed from the 10% highest $FA_{ST}$ voxels in the fornix are shown in red, from the 50% highest $FA_{ST}$ voxels in blue. Linear regression lines with age are shown in each plot.

Table 3.1: Regression coefficients for diffusion statistics from figure 3.8. Column $\beta_{\text{age}}$ (10%) shows the regression coefficients of statistics computed from the 10% highest $\text{FA}_{\text{ST}}$ voxels in the fornix, column $\beta_{\text{age}}$ (50%) of the 50% highest $\text{FA}_{\text{ST}}$ voxels in the fornix. In rows $\text{FA}_{\text{MD}}{}^*$ and $f_{\text{MD}}{}^*$ the regression coefficients were calculated including the used MD-constraint (i.e. $\text{MD}_{\text{Splenium}}$) as a covariate. In rows $\text{FA}_{\text{AxD}}{}^*$ and $f_{\text{AxD}}{}^*$ the regression coefficients were calculated including the used AxD-constraint (i.e. $\text{AxD}_{\text{Splenium}}$) as a covariate. The unit of $\beta$ is in $\text{year}^{-1}$, except for $\text{MD}_{\text{ST}}$, which is in $\text{mm}^2\text{s}^{-1}\text{year}^{-1}$. Regression coefficients with a p-value<0.05 are denoted in bold.

| Variables | $\beta_{\text{age}}$ (10%) | p-value | $\beta_{\text{age}}$ (50%) | p-value |
|---|---|---|---|---|
| $\text{FA}_{\text{ST}}$ | $\mathbf{-3.6\cdot 10^{-3}}$ | $1.3\cdot 10^{-7}$ | $\mathbf{-2.7\cdot 10^{-3}}$ | $1.3\cdot 10^{-7}$ |
| $\text{MD}_{\text{ST}}$ | $\mathbf{9.6\cdot 10^{-6}}$ | $4.1\cdot 10^{-8}$ | $\mathbf{9.0\cdot 10^{-6}}$ | $1.2\cdot 10^{-10}$ |
| $\text{FA}_{\text{MD,Glob}}$ | $\mathbf{1.1\cdot 10^{-3}}$ | $4.6\cdot 10^{-2}$ | $\mathbf{1.3\cdot 10^{-3}}$ | $2.1\cdot 10^{-3}$ |
| $f_{\text{MD,Glob}}$ | $\mathbf{-7.7\cdot 10^{-3}}$ | $5.4\cdot 10^{-8}$ | $\mathbf{-6.0\cdot 10^{-3}}$ | $1.5\cdot 10^{-10}$ |
| $\text{FA}_{\text{MD}}$ | $\mathbf{-1.8\cdot 10^{-3}}$ | $3.9\cdot 10^{-3}$ | $\mathbf{-1.5\cdot 10^{-3}}$ | $2.8\cdot 10^{-3}$ |
| $\text{FA}_{\text{AxD}}$ | $\mathbf{-2.4\cdot 10^{-3}}$ | $1.7\cdot 10^{-2}$ | $\mathbf{-1.9\cdot 10^{-3}}$ | $6.0\cdot 10^{-3}$ |
| $f_{\text{MD}}$ | $\mathbf{-3.9\cdot 10^{-3}}$ | $2.9\cdot 10^{-3}$ | $\mathbf{-3.1\cdot 10^{-3}}$ | $3.0\cdot 10^{-4}$ |
| $f_{\text{AxD}}$ | $\mathbf{-3.3\cdot 10^{-3}}$ | $3.3\cdot 10^{-2}$ | $\mathbf{-2.7\cdot 10^{-3}}$ | $5.3\cdot 10^{-3}$ |
| $\text{FA}_{\text{MD}}{}^*$ | $7.3\cdot 10^{-4}$ | $2.2\cdot 10^{-1}$ | $\mathbf{9.0\cdot 10^{-4}}$ | $4.6\cdot 10^{-2}$ |
| $\text{FA}_{\text{AxD}}{}^*$ | $5.2\cdot 10^{-4}$ | $6.0\cdot 10^{-1}$ | $4.1\cdot 10^{-4}$ | $5.6\cdot 10^{-1}$ |
| $f_{\text{MD}}{}^*$ | $\mathbf{-3.9\cdot 10^{-3}}$ | $5.6\cdot 10^{-3}$ | $\mathbf{-3.1\cdot 10^{-3}}$ | $6.4\cdot 10^{-4}$ |
| $f_{\text{AxD}}{}^*$ | $\mathbf{-3.8\cdot 10^{-3}}$ | $2.0\cdot 10^{-2}$ | $\mathbf{-3.0\cdot 10^{-3}}$ | $3.4\cdot 10^{-3}$ |

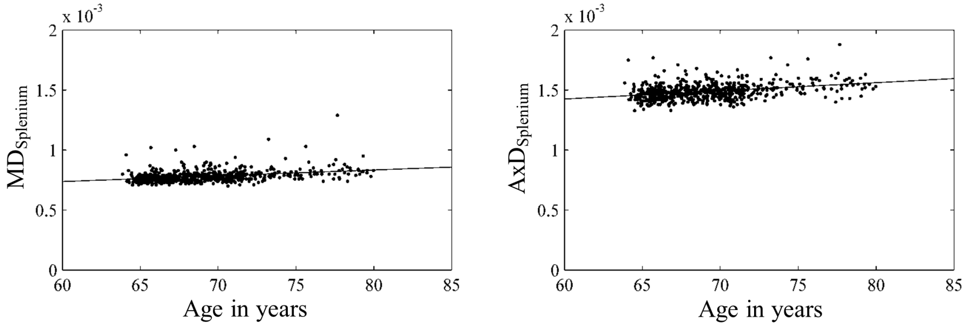

Figure 3.9: Scatter plots of diffusion statistics of the median $\text{FA}_{\text{ST}}$ (left) and $\text{MD}_{\text{ST}}$ (right) versus age in the splenium of the corpus callosum. Linear regression lines with age are also shown. All regression lines are significant.

### 3.4.1. DEPENDENCE ON MACROSTRUCTURAL PROPERTIES

The simulation results showed that conventional, single-tensor, DTI metrics such as $\mathrm{FA}_{\mathrm{ST}}$ and $\mathrm{MD}_{\mathrm{ST}}$ become increasingly biased with decreasing fiber diameter. This confirms prior work that investigated the influence of partial volume effects on DTI metrics [5]. Our simulation experiment also demonstrated that excluding the most contaminated voxels from the fiber bundle segmentations was only partially effective in removing CSF contamination. In fiber bundles with diameters larger than approximately three times the voxel size, CSF contamination could be removed by restricting the analysis to the 10% least contaminated voxels. Segmentations of smaller fiber bundles exist (almost) exclusively of boundary voxels, for which the employed heuristic of analyzing the 10% least contaminated voxels was less effective. Essentially, this demonstrates that the conventional FA measurements on the fornix in elderly subjects (having a diameter of approximately 4 mm) can be particularly affected by CSF contamination when imaged with a slice thickness or in-plane resolution larger than 3 mm.

The mean $\mathrm{FA}_{\mathrm{MD}}$ and $\mathrm{FA}_{\mathrm{AxD}}$ were independent of the fiber diameter even for very small fiber diameters. However, for small fiber diameters (i.e. smaller than 6 mm) the variance in the estimated $\mathrm{FA}_{\mathrm{MD}}$ and $\mathrm{FA}_{\mathrm{AxD}}$ increased a bit due to a smaller region-of-interest over which these statistics are computed, and (on average) a smaller fraction of the signal that originates from the tissue compartment in each voxel.

The macrostructural dependence of diffusion statistics was further evaluated on the aging study data by comparing the diffusion statistics computed from respectively the 10% and 50% highest $\mathrm{FA}_{\mathrm{ST}}$ voxels. For conventional diffusion statistics such as $\mathrm{FA}_{\mathrm{ST}}$ and $\mathrm{MD}_{\mathrm{ST}}$, clear and highly significant differences were observed between the means from the 10% and 50% highest $\mathrm{FA}_{\mathrm{ST}}$ voxels. Diffusion statistics $\mathrm{FA}_{\mathrm{MD}}$ and $\mathrm{FA}_{\mathrm{AxD}}$ appeared relatively robust to the choice of using the 10% or 50% highest $\mathrm{FA}_{\mathrm{ST}}$ voxels, suggesting these statistics are CSF contamination-invariant.

### 3.4.2. AGEING

Conventional diffusion statistics $\mathrm{FA}_{\mathrm{ST}}$ and $\mathrm{MD}_{\mathrm{ST}}$ decreased and increased, respectively, with age. This may reflect changes in the fornix microstructure, but may also reflect fornix atrophy that yields increased levels of CSF contamination. The bi-tensor statistics $\mathrm{FA}_{\mathrm{MD}}$ and $\mathrm{FA}_{\mathrm{AxD}}$ both decreased significantly with age, suggesting changes in the fornix microstructure. However, the negative correlation of $\mathrm{FA}_{\mathrm{MD}}$ and $\mathrm{FA}_{\mathrm{AxD}}$ with age disappeared when the applied subject-specific constraints were added as a covariate in the regression analysis. This may suggest that the microstructural change in the body of the fornix is not significantly different from the microstructural change in the splenium of the corpus callosum.

The bi-tensor tissue fractions $f_{\mathrm{MD}}$ and $f_{\mathrm{AxD}}$ decreased significantly with age, even after adding the applied subject-specific constraints as a covariate in the regression analysis. This may suggest that there is a change in the fornix that appears as if tissue is being replaced by water. This could be due to fornix atrophy but could also reflect a higher degree of extra-cellular water in the fornix microstructure (see below).

### 3.4.3. SUBJECT-SPECIFIC CONSTRAINTS VERSUS A GLOBAL CONSTRAINT

The use of subject-specific constraints has advantages and disadvantages compared to the use of a global constraint. By computing subject-specific constraints from (noisy) splenium data, additional uncertainty may be added to the estimated bi-tensor parameters compared to a global constraint. However, the results of the reproducibility study showed that the reproducibility of $\text{FA}_{\text{MD,Glob}}$ and $\text{FA}_{\text{MD}}$ is very similar, which suggests this effect is not large. An advantage of subject-specific constraints is that computing the constraints from the same subject may yield an increased accuracy of the estimated bi-tensor parameters. Particularly in a study population with large variations (e.g. due to a wide age range), the use of a global constraint may not be appropriate for every subject. This may result in a decreased accuracy compared to using subject-specific constraints.

### 3.4.4. LIMITATIONS

Inherent limitations of our work are in the constraints that have to be imposed to make estimation with the bi-tensor well-posed in the fornix. Besides bias and variance due to noise on the data, also potential differences in the tissue microstructure of the splenium and fornix (e.g. different degrees of extracellular water) may make the imposed constraints less appropriate. The effect of using inappropriate constraints was evaluated in simulated fiber bundles. The results showed that when these constraints are violated, a slight bias may be introduced into the estimation of $\text{FA}_{\text{MD}}$ and $\text{FA}_{\text{AxD}}$. However, for realistic in-vivo differences between ground truth and constrained value these biases were small (in the order of 5%). Still, these effects may add scatter to the final data, thereby decreasing the statistical power of the proposed framework with respect to single-tensor data.

One type of microstructural change that may not be reflected in the FA of a bi-tensor model is an increase in extracellular, intra-tract water content. The CSF-compartment in the bi-tensor model is a free-water compartment. Simultaneously, in loosely packed white matter bundles, extracellular water in the microstructure could be assumed to have diffusivity properties close to those of free-water. Under this assumption any increase in extracellular water gives rise to a decrease in the tissue fraction, while leaving the diffusivities of the tissue diffusion tensor unchanged. As a consequence, the tissue fractions in the bi-tensor model are not CSF-contamination invariant: it may model the amount of CSF contamination as well as the amount of extracellular water. Thus, the interpretation of changes in this parameter is not trivial as it may be driven by both macrostructural and microstructural changes. To further distinguish between these different kinds of microstructural change an acquisition protocol with multiple $b$-values is required. However, such imaging was not performed for our study data.

## 3.5. CONCLUSION

OUR research showed how conventional (single non-zero $b$-value) DW-MRI datasets can be analyzed with an MD-constrained or AxD-constrained bi-tensor model. In simulations the mean FA estimated by these constrained bi-tensors models did not depend on macrostructural properties, which suggests that our diffusion statistics are indeed CSF contamination-invariant. Diffusion parameters such as the bi-tensor tissue fractions or the single tensor FA or MD were not CSF contamination-invariant. The bias in these diffusion statistics did not only depend on macrostructural properties such as the diameter of a white matter structure, but also on whether the 10% or 50% least contaminated voxels in a segmentation were used. Results from the ageing study suggest the occurrence of microstructural change in the body of the fornix with age. However, this change is not significantly different from the microstructural change occurring in the splenium of the corpus callosum. In conclusion, the distinction of an isotropic and an anisotropic diffusion compartment can allow a more sophisticated analysis in future studies of the fornix, particularly to discriminate between microstructural and macrostructural changes.

## REFERENCES

[1] E. Stejskal and J. Tanner, *Spin diffusion measurements: spin echoes in the presence of a time-dependent field gradient,* The journal of chemical physics **42**, 288 (1965).

[2] C. Beaulieu, *The basis of anisotropic water diffusion in the nervous system–a technical review,* NMR in Biomedicine **15**, 435 (2002).

[3] P. J. Basser, J. Mattiello, and D. LeBihan, *Mr diffusion tensor spectroscopy and imaging,* Biophysical journal **66**, 259 (1994).

[4] A. L. Alexander, K. M. Hasan, M. Lazar, J. S. Tsuruda, and D. L. Parker, *Analysis of partial volume effects in diffusion-tensor mri,* Magnetic Resonance in Medicine **45**, 770 (2001).

[5] S. B. Vos, D. K. Jones, M. A. Viergever, and A. Leemans, *Partial volume effect as a hidden covariate in dti analyses,* Neuroimage **55**, 1566 (2011).

[6] C. Metzler-Baddeley, D. K. Jones, and M. J. O'Sullivan, *Csf contamination contributes to apparent microstructural alterations in mild cognitive impairment,* Neuroimage **92**, 27 (2014).

[7] L. Concha, D. W. Gross, and C. Beaulieu, *Diffusion tensor tractography of the limbic system,* American Journal of Neuroradiology **26**, 2267 (2005).

[8] J. P. Aggleton, D. McMackin, K. Carpenter, J. Hornak, N. Kapur, S. Halpin, C. Wiles, H. Kamel, P. Brennan, and S. Carton, *Differential cognitive effects of colloid cysts in the third ventricle that spare or compromise the fornix,* Brain **123**, 800 (2000).

[9] C. Metzler-Baddeley, D. K. Jones, B. Belaroussi, J. P. Aggleton, and M. J. O'Sullivan, *Frontotemporal connections in episodic memory and aging: a diffusion mri tractography study,* Journal of Neuroscience **31**, 13236 (2011).

[10] N. G. Papadakis, K. M. Martin, M. H. Mustafa, I. D. Wilkinson, P. D. Griffiths, C. L. Huang, and P. W. Woodruff, *Study of the effect of csf suppression on white matter diffusion anisotropy mapping of healthy human brain,* Magnetic resonance in medicine **48**, 394 (2002).

[11] M.-C. Chou, Y.-R. Lin, T.-Y. Huang, C.-Y. Wang, H.-W. Chung, C.-J. Juan, and C.-Y. Chen, *Flair diffusion-tensor mr tractography: comparison of fiber tracking with conventional imaging,* American journal of neuroradiology **26**, 591 (2005).

[12] H. Takao, N. Hayashi, S. Inano, and K. Ohtomo, *Effect of head size on diffusion tensor imaging,* Neuroimage **57**, 958 (2011).

[13] W. Rashid, A. Hadjiprocopis, C. Griffin, D. Chard, G. Davies, G. Barker, P. Tofts, A. Thompson, and D. Miller, *Diffusion tensor imaging of early relapsing-remitting multiple sclerosis with histogram analysis using automated segmentation and brain volume correction,* Multiple Sclerosis **10**, 9 (2004).

[14] M. W. Vernooij, M. de Groot, A. van der Lugt, M. A. Ikram, G. P. Krestin, A. Hofman, W. J. Niessen, and M. M. Breteler, *White matter atrophy and lesion formation explain the loss of structural integrity of white matter in aging,* Neuroimage **43**, 470 (2008).

[15] C. Metzler-Baddeley, M. J. O'Sullivan, S. Bells, O. Pasternak, and D. K. Jones, *How and how not to correct for csf-contamination in diffusion mri,* Neuroimage **59**, 1394 (2012).

[16] C. Pierpaoli and D. Jones, *Removing csf contamination in brain dt-mris by using a two-compartment tensor model,* in *Proc. International Society for Magnetic Resonance in Medicine 12th Scientific meeting ISMRM04* (2004) p. 1215.

[17] H. Zhang, T. Schneider, C. A. Wheeler-Kingshott, and D. C. Alexander, *Noddi: practical in vivo neurite orientation dispersion and density imaging of the human brain,* Neuroimage **61**, 1000 (2012).

[18] O. Pasternak, N. Sochen, Y. Gur, N. Intrator, and Y. Assaf, *Free water elimination and mapping from diffusion mri,* Magnetic Resonance in Medicine **62**, 717 (2009).

[19] A. R. Hoy, C. G. Koay, S. R. Kecskemeti, and A. L. Alexander, *Optimization of a free water elimination two-compartment model for diffusion tensor imaging,* Neuroimage **103**, 323 (2014).

[20] C. R. Jack, M. A. Bernstein, B. J. Borowski, J. L. Gunter, N. C. Fox, P. M. Thompson, N. Schuff, G. Krueger, R. J. Killiany, and C. S. DeCarli, *Update on the magnetic resonance imaging core of the alzheimer's disease neuroimaging initiative,* Alzheimer's & Dementia **6**, 212 (2010).

[21] M. A. Ikram, A. van der Lugt, W. J. Niessen, P. J. Koudstaal, G. P. Krestin, A. Hofman, D. Bos, and M. W. Vernooij, *The rotterdam scan study: design update 2016 and main findings,* European journal of epidemiology **30**, 1299 (2015).

[22] M. Taquet, B. Scherrer, N. Boumal, J. M. Peters, B. Macq, and S. K. Warfield, *Improved fidelity of brain microstructure mapping from single-shell diffusion mri,* Medical image analysis **26**, 268 (2015).

[23] G. A. Arkesteijn, D. H. Poot, M. de Groot, M. W. Vernooij, W. J. Niessen, L. J. Van Vliet, and F. M. Vos, *Csf contamination-invariant statistics in diffusion-weighted mri,* in *Biomedical Imaging (ISBI), 2015 IEEE 12th International Symposium on* (IEEE, 2015) pp. 454–457.

[24] A. Hofman, G. G. Brusselle, S. D. Murad, C. M. van Duijn, O. H. Franco, A. Goedegebure, M. A. Ikram, C. C. Klaver, T. E. Nijsten, and R. P. Peeters, *The rotterdam study: 2016 objectives and design update,* European journal of epidemiology **30**, 661 (2015).

[25] H. A. Vrooman, C. A. Cocosco, F. van der Lijn, R. Stokking, M. A. Ikram, M. W. Vernooij, M. M. Breteler, and W. J. Niessen, *Multi-spectral brain tissue segmentation using automatically trained k-nearest-neighbor classification,* Neuroimage **37**, 71 (2007).

[26] T. G. Close, J.-D. Tournier, F. Calamante, L. A. Johnston, I. Mareels, and A. Connelly, *A software tool to generate simulated white matter structures for the assessment of fibre-tracking algorithms,* Neuroimage **47**, 1288 (2009).

[27] R. de Boer, M. Schaap, F. van der Lijn, H. A. Vrooman, M. de Groot, M. W. Vernooij, M. A. Ikram, E. F. van Velsen, A. van der Lugt, and M. M. Breteler, *Statistical analysis of structural brain connectivity,* in *Medical Image Computing and Computer-Assisted Intervention–MICCAI 2010* (Springer, 2010) pp. 101–108.

[28] S. Klein, M. Staring, K. Murphy, M. Viergever, and J. P. Pluim, *Elastix: a toolbox for intensity-based medical image registration,* Medical Imaging, IEEE Transactions on **29**, 196 (2010).

[29] A. Leemans and D. K. Jones, *The b-matrix must be rotated when correcting for subject motion in dti data,* Magnetic Resonance in Medicine **61**, 1336 (2009).

[30] D. H. Poot and S. Klein, *Detecting statistically significant differences in quantitative mri experiments, applied to diffusion tensor imaging,* Medical Imaging, IEEE Transactions on **34**, 1164 (2015).

[31] H. Gudbjartsson and S. Patz, *The rician distribution of noisy mri data,* Magnetic resonance in medicine **34**, 910 (1995).

[32] T. Hattori, K. Ito, S. Aoki, T. Yuasa, R. Sato, M. Ishikawa, H. Sawaura, M. Hori, and H. Mizusawa, *White matter alteration in idiopathic normal pressure hydrocephalus: tract-based spatial statistics study,* American Journal of Neuroradiology **33**, 97 (2012).

[33] B. Fischl, D. H. Salat, A. J. van der Kouwe, N. Makris, F. Ségonne, B. T. Quinn, and A. M. Dale, *Sequence-independent segmentation of magnetic resonance images,* Neuroimage **23**, S69 (2004).

[34] M.-R. Nazem-Zadeh, C. H. Chapman, T. L. Lawrence, C. I. Tsien, and Y. Cao, *Radiation therapy effects on white matter fiber tracts of the limbic circuit,* Medical physics **39**, 5603 (2012).

[35] M.-R. Nazem-Zadeh, S. Saksena, A. Babajani-Fermi, Q. Jiang, H. Soltanian-Zadeh, M. Rosenblum, T. Mikkelsen, and R. Jain, *Segmentation of corpus callosum using diffusion tensor imaging: validation in patients with glioblastoma,* BMC medical imaging **12**, 10 (2012).

# 4

# ORIENTATION PRIOR AND CONSISTENT MODEL SELECTION INCREASE SENSITIVITY OF TRACT-BASED SPATIAL STATISTICS IN CROSSING-FIBER REGIONS

*The goal of this chapter is to increase the statistical power of crossing-fiber statistics in voxelwise analyses of diffusion-weighted magnetic resonance imaging (DW-MRI) data. In the proposed framework a fiber orientation atlas and a model complexity atlas were used to fit the ball-and-sticks model to diffusion-weighted images of subjects in a prospective population-based cohort study. Reproducibility and sensitivity of the partial volume fractions in the ball-and-sticks model were analyzed using TBSS (tract-based spatial statistics), and were compared to a reference framework. The reproducibility was investigated on two scans of 30 subjects acquired with an interval of approximately three weeks by studying the intraclass correlation coefficient (ICC). The sensitivity to true biological effects was evaluated by studying the regression with age on 500 subjects between 65 and 90 years old. Compared to the reference framework, the ICC improved significantly when using the proposed framework. Higher t-statistics indicated that regression coefficients with age could be determined more precisely with the proposed framework, and more voxels correlated significantly with age. The application of a fiber orientation atlas and a model complexity atlas can significantly improve the reproducibility and sensitivity of crossing-fiber statistics in TBSS.*

---

G.A.M. Arkesteijn, D.H.J. Poot, M.A. Ikram, W.J. Niessen, L.J. van Vliet, M.W. Vernooij, and F.M. Vos, submitted to *IEEE Transactions on Medical Imaging*.

## 4.1. INTRODUCTION

DIFFUSION-WEIGHTED magnetic resonance imaging (DW-MRI) is a non-invasive imaging technique in which image contrast is determined by the (hindered) molecular diffusion of water [1]. It is frequently used to assess the brain's white matter integrity, because it provides insight into the microstructural organization of neural fibers [2]. A popular application is diffusion tensor imaging (DTI), in which the water diffusion is modeled by a single Gaussian diffusion profile [3]. From the diffusion tensor, quantitative DTI metrics such as the fractional anisotropy (FA) and mean diffusivity (MD) can be derived. These DTI metrics are often used as an imaging biomarker for white matter tract integrity, to study for example neurodegenerative diseases or brain ageing [4, 5].

It is well known that the assumption of a single diffusion tensor model to represent the underlying diffusion within the volume of a single voxel is not always valid, e.g. in voxels with more than one coherently orientated fiber population [6, 7]. In such voxels, the analysis of conventional DTI metrics has undesirable effects: spurious changes may be detected in the radial and axial diffusivity [8], FA may lack sensitivity to detect changes in the white matter microstructure [9], and FA may seem to be paradoxically increased merely due to selective degeneration of a fiber population [10].

Several alternative models have been proposed to provide a more adequate description of the diffusion in fiber crossings, e.g. the ball-and-sticks model [11], multi-tensor models [7, 12], or CHARMED [13]. These models describe the diffusion signal in crossing-fiber configurations by modeling each fiber population independently, and enable fiber population-specific characterization and comparison of the underlying microstructure. However, these models typically require more extensive DW-MRI protocols, making the image acquisition lengthy. Furthermore, sophisticated routines are needed to determine the appropriate number of fiber populations by using either explicit [14] or implicit model selection [11].

Researchers frequently use voxelwise analyses of DW-MRI data to localize changes in diffusion parameters in group studies. A popular framework for such an analysis is TBSS (tract-based spatial statistics) [15], which applies an FA-driven registration to establish spatial correspondence of all subjects in a common space. Subsequently, individual FA features are projected on a mean 'tract' skeleton for subsequent statistical analysis. However, applying this approach to evaluate statistics in fiber-crossings is not straightforward. In that case, not only the spatial coordinates but also the fiber population-specific metrics need to correspond across subjects for a meaningful analysis.

Recently, a framework was proposed to analyze crossing-fiber statistics in TBSS using a front-evolution algorithm to label the fiber populations based on their estimated orientations [16]. However, the fiber orientation-based labeling problem does not necessarily have a trivial solution in every voxel. Especially for conventional DW-MRI data (single non-zero $b$-value), the estimated fiber orientations and model selection routines can be imprecise. In effect, inconsistent metrics may be obtained from fiber populations across subjects, which in turn may cause crossing-fiber statistics to loose statistical power. This may explain why crossing-fiber statistics were less sensitive to ageing-effects than conventional metrics from a single diffusion tensor in [16].

The goal of this chapter is to introduce a framework that strengthens the statistical power of crossing-fiber statistics in voxelwise analyses of conventional DW-MRI data. This is achieved by reducing fluctuations in the orientations of the estimated fiber populations and preventing inconsistencies in the number of fiber populations, through two additions to the fitting procedure of a crossing-fibers model. The first addition is the introduction of an ‘orientation prior’ into the estimation of the model parameters. This prior promotes correspondence of estimated fiber orientations across different subjects. The second addition is a ‘consistent model selection’, obtained by determining the number of fiber populations in a common space instead of independently in each subject.

We evaluate the impact of this new approach on the reproducibility and sensitivity of crossing-fiber statistics. More specifically, the reproducibility is evaluated on two scans of 30 subjects, acquired with an interval of approximately three weeks. Furthermore, the sensitivity to detect ageing effects is investigated in a group of 500 community-dwelling subjects aged 65 to 90 years. In this work we restrict our investigation to the analysis of partial volume fractions (PVFs) in the well-known ball-and-sticks model using TBSS, but the proposed changes are straightforward and easy to generalize to other generative crossing-fiber models and different frameworks for voxelwise analyses. The proposed framework is compared to standard approaches based on the conventional, single tensor representation and another approach relying on the ball-and-sticks model.

## 4.2. METHODS

### 4.2.1. OVERVIEW OF THE PROPOSED FRAMEWORK

An overview of the proposed framework is provided in figure 4.1. Two versions of the ball-and-sticks model were fitted to the diffusion-weighted images (DWIs). The first with one stick compartment and the second with two stick compartments. The ball-and-two-sticks model was regularized using a fiber orientation atlas to enhance the precision of the fit. Next, an adjusted TBSS pipeline was used to transform and skeletonize the estimated PVFs into a common space. In the common space the different skeletonized datasets were merged according to a model complexity atlas: in two-fiber skeleton voxels the PVFs originate from the ball-and-two-sticks diffusion model, whereas in single fiber voxels the first PVF originated from the ball-and-one stick model and the second PVF was set to zero. As such, consistent model selection was enforced across the subjects of the study population.

### 4.2.2. STUDY POPULATION

The proposed framework was evaluated using a subset of brain imaging data from the Rotterdam Study, a prospective population-based cohort study among middle aged and elderly subjects in a district of the city of Rotterdam, the Netherlands [17]. The Rotterdam Study has been approved by the medical ethics committee according to the Population Study Act Rotterdam Study, executed by the Ministry of Health, Welfare and Sports of the Netherlands. Written informed consent was obtained from all participants. The reproducibility of extracting crossing-fiber diffusion parameters was evaluated from two scans of 30 subjects, acquired on the same scanner with an average time interval of 19.5 days (SD 10). We will refer to this dataset as the reproducibility dataset. The subjects in this dataset were on average 76.7 (SD 4.8) years old, 50% was female. Further evaluation

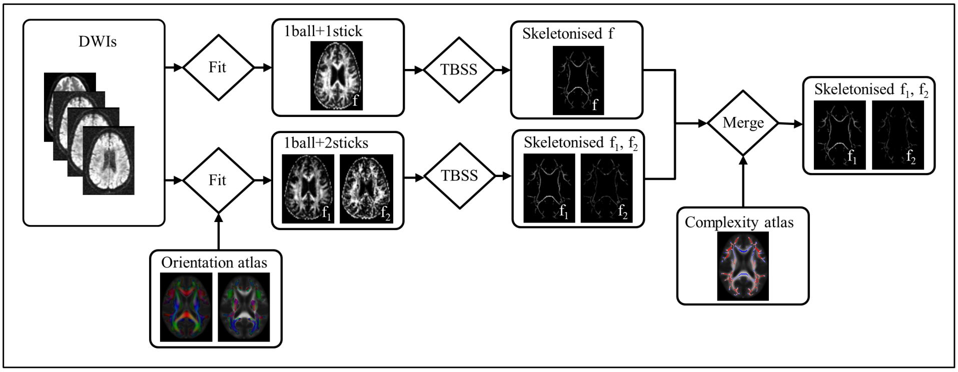

Figure 4.1: Overview of the proposed framework. Two diffusion models, i.e. a ball-and-one-stick and a ball-and-two-sticks model, are fitted to diffusion-weighted images (DWIs) per subject. An orientation prior, warped from the common space to subject space, is used to initialize the fit of the ball-and-two-sticks model and also acts as an orientation prior during fitting. The estimated partial volume fractions (PVFs) are warped and skeletonized using an adjusted TBSS pipeline. In the common space, the different skeletonized datasets are merged according to a complexity atlas, such that two skeletonized datasets remain. In single-fiber and crossing-fiber voxels (according to the model complexity atlas) the two skeletonized datasets contain PVFs from a ball-and-one-stick and a ball-and-two-sticks model respectively.

of the framework was performed on a group of 500 subjects from the Rotterdam Study, sampled from the entire population such that their ages were uniformly distributed between 65 and 90 years old. We will refer to this data as the ageing dataset. The mean age in this group was 77.3 (SD 7.0) years old, 45% was female. All subjects were free of dementia at the time of the MRI scans.

### 4.2.3. DATA ACQUISITION

All subjects were scanned on a 1.5 Tesla MRI scanner (GE Signa Excite) using an 8-channel head coil. No major hardware or software updates were performed on the scanner throughout the study [18]. DWIs were acquired with a single shot, diffusion-weighted spin echo echo-planar imaging sequence using a repetition time TR = 8575 ms, an echo time TE = 82.6 ms, a field of view FOV = 210x210 mm$^2$, an imaging matrix = 96x64 (zero-padded to 256x256), 35 contiguous slices with a thickness of 3.5 mm, and (hence) a native voxel size of 2.2 mm x 3.3 mm x 3.5 mm. DWIs were acquired in 25 non-collinear directions with a maximum $b$-value of 1000 s/mm$^2$. Three volumes were acquired without diffusion weighting (the $b_0$-volumes) [18].

### 4.2.4. DWI PREPROCESSING

The acquired DWIs were corrected for motion and eddy current distortion by affine coregistration to the second acquired $b_0$-volume with Elastix [19]. The DWIs were resampled to (2.5 mm)$^3$ cubic resolution while the affine transformations were applied. After coregistration to the reference $b_0$-volume, the gradient directions were reoriented according to the rotation component of the transformation [20].

### 4.2.5. BALL-AND-STICKS MODEL

In the ball-and-sticks model [11], the diffusion-weighted signal $\mathbf{S}_{\boldsymbol{\theta}}$ is modeled according to:

$$S_{\boldsymbol{\theta},i} = S_0\left(\left(1-\sum_{j=1}^{N} f_j\right)\exp\left(-b_i d\right)+\sum_{j=1}^{N} f_j \exp\left(-b_i d\left(\mathbf{V}_j\cdot\mathbf{g}_i\right)^2\right)\right), \tag{4.1}$$

where $b_i$ is the diffusion-weighting parameter, $\mathbf{g}_i$ is a unit vector that specifies the direction of the diffusion-encoding gradient pulses, $S_0$ is the non-diffusion-weighted signal, $N$ is the number of stick compartments (0, 1 or 2 in this chapter), $d$ is a diffusivity parameter, $f_j$ is the partial volume fraction (PVFs) and $\mathbf{V}_j$ the principal eigenvector of the $j$th stick compartment. As in [11], the eigenvectors $\mathbf{V}_j$ are parameterized using spherical coordinates $\psi_j$ and $\phi_j$.

### 4.2.6. AUTOMATIC RELEVANCE DETECTION

The fiber orientation atlas and model complexity atlas were constructed based on automatic relevance determination (ARD). Prior work has used ARD to estimate the unknown parameters in the ball-and-sticks model [11]. In the ARD framework (available through the function `bedpostx` as part of FSL [11]), a Bayesian approach is applied to fit a ball-and-sticks model with two stick compartments in every voxel. We will refer to the stick associated with the largest volume fraction as the primary fiber population; the stick with the smallest volume fraction will be called the secondary fiber population. Overfitting is avoided by using a shrinkage prior that automatically reduces the volume fraction of the secondary fiber population to zero when it is not supported by the data.

### 4.2.7. CONSTRUCTION OF THE FIBER ORIENTATION ATLAS

To construct the orientation atlas, first the diffusion tensor parameters were estimated in all 500 subjects using the fit_MRI toolbox by maximum likelihood estimation [21] assuming Rician distributed data. Additionally, the ball-and-two-stick parameters were estimated through ARD. DTI-TK was used to align the diffusion tensor images to a population-specific common space using the full diffusion tensor information [22]. Subsequently, the functions `deformationScalar3DVolume` and `deformationSymTensor3DVolume` in DTI-TK were used to warp the PVFs and the corresponding stick orientations from ARD to this same common space. In the common space fiber populations with PVFs smaller than 0.05 were discarded [11], such that voxels could contain zero, one or two fiber populations.

To compute the fiber orientation atlas, in each voxel the remaining primary and secondary fiber orientations (i.e. with PVFs above 0.05) were clustered into two groups from which the average orientations were computed. The clustering was achieved using an adapted $K$-means clustering routine ($K = 2$), that effectively minimizes this sum of squared angular errors (reckoning with 180° symmetry):

$$J = \sum_{k=1}^{2}\sum_{i\in C_k} \arccos\left(\mathrm{abs}\left(\mathbf{V}_i\cdot\mathbf{V}_{k,\mathrm{mean}}\right)\right)^2, \tag{4.2}$$

where $C_k$ is the $k$th cluster, $\mathbf{V}_i$ the $i$th fiber orientation in $C_k$, and $\mathbf{V}_{k,\mathrm{mean}}$ the average fiber orientation of all fiber orientations in $C_k$. Specifically, the $K$-means clustering routine was initialized by assigning all largest stick compartments to the first cluster and all smallest stick compartments to the second cluster. Next, in the update step, the mean orientation of each cluster was obtained by first computing the scatter matrices $\mathbf{S}_k$ (the sum of dyadic products of the fiber orientations) [23]:

$$\mathbf{S}_k = \sum_{i \in C_l} \mathbf{V}_i \cdot \mathbf{V}_i^T. \tag{4.3}$$

Subsequently, the average fiber orientation $\mathbf{V}_{k,\text{mean}}$ was computed as the principal eigenvector of the matrix $\mathbf{S}_k$, i.e. the eigenvector corresponding to the largest eigenvalue. In the assignment step each fiber orientation was assigned to the 'nearest' cluster mean in terms of angle (reckoning with 180° symmetry). The update and assignment step were iterated until no fibers changed cluster.

### 4.2.8. CONSTRUCTION OF THE COMPLEXITY ATLAS

In the common space the FA images, derived from the spatially-normalized diffusion tensor images, were averaged after which a skeleton was generated with the function `tbss_skeleton` (in FSL). The mean FA skeleton was thresholded at 0.2 merely to exclude voxels with large inter-subject variability and/or partial volume effects with grey matter or cerebrospinal fluid. Subsequently, the warped PVF volumes (see the previous section) were 'skeletonized' by only retaining the voxels overlapping with the mean FA skeleton mask. Note that for establishing correspondence, DTI-TK performs a high dimensional registration, similar to previous work [24] instead of a 'maximum skeleton projection' step of a standard TBSS analysis [15]. At the end of the procedure, each skeleton voxel may contain zero, one or two fiber populations. The model complexity atlas was defined as the average number of fiber populations in each FA skeleton voxel.

### 4.2.9. MODEL ESTIMATION

The ball-and-one-stick model in the proposed framework was fit by maximum likelihood estimation as in [21]; not using any prior knowledge on the stick's orientation. The ball-and-two-sticks model was fit using the fiber orientation atlas in two ways: (1) the atlas orientation was used to initialize the non-linear fit, and (2) a Gaussian-shaped prior $p(\boldsymbol{\theta})$ was applied to regularize the fitting of the model:

$$p(\boldsymbol{\theta}) = \exp\left(-\frac{\epsilon_1^2}{2\sigma_\theta^2}\right)\exp\left(-\frac{\epsilon_2^2}{2\sigma_\theta^2}\right), \tag{4.4}$$

where $\epsilon_1$ and $\epsilon_2$ represent the angles between the principal eigenvector of both sticks and their corresponding atlas orientations (reckoning with 180° symmetry), and $\sigma_\theta$ denotes the width of the Gaussian-shaped orientation prior. The estimate of $\boldsymbol{\theta}$ is given by:

$$\hat{\boldsymbol{\theta}} = \underset{\boldsymbol{\theta}}{\arg\max}\ \log\Big(p(\mathbf{S}|\boldsymbol{\theta})\,p(\boldsymbol{\theta})\Big) \tag{4.5}$$

which was implemented using the fit_MRI toolbox [21].

### 4.2.10. PROPOSED TBSS ANALYSIS

The PVFs of the ball-and-one-stick as well as the ball-and-two-sticks model parameters were warped to the common space using the computed DTI-TK transformations (see above). Subsequently, the two parameter sets were 'skeletonized' by retaining the voxels coinciding with the FA skeleton mask. Trilinear interpolation was used in warping the images to the common space. This was possible because the PVFs in the ball-and-two-sticks model are implicitly sorted in subject space by means of the orientation prior. Finally, the skeletonized datasets from the two models were merged according to the model complexity atlas: the two-fiber voxels (according to the model complexity atlas) of the skeleton received the primary and secondary PVFs from a two-stick diffusion model; the single fiber skeleton voxels obtained the primary PVF from the one-stick diffusion model and the secondary PVF was set to zero.

To facilitate comparison with the second reference pipeline (see below), we also evaluated the effect of using nearest-neighbour interpolation (instead of trilinear interpolation) to transform the PVFs to the common space. For this purpose two adapted versions of the proposed framework were considered, either simply using nearest-neighbour interpolation to warp the PVFs or using 3D Gaussian smoothing prior to using nearest-neighbour interpolation to warp the PVFs. The standard deviation of the 3D Gaussian smoothing kernel was set to 0.487 voxels, such that it approximately matched the smoothing effect of trilinear interpolation.

### 4.2.11. REFERENCE FRAMEWORKS

The first reference framework essentially performed a modified TBSS analysis of conventional diffusion tensor images. In the common space FA images, computed from the spatially-normalized diffusion tensor images, were 'skeletonized' by only retaining the voxels coinciding with the mean FA skeleton mask. As such, we (again) did not use the 'maximum skeleton projection' step of the standard TBSS analysis [15]. This is relevant because the projection may favor single fiber voxels since these tend to have a higher FA than crossing-fiber voxels. Subsequently, FA statistics were evaluated for each skeleton voxel as in the conventional TBSS analysis.

The second reference framework relied on the primary and secondary PVFs from the ARD modeling. The FSL routine `tbss_x` [16] was used to warp these PVFs and their corresponding stick orientations to the common space, 'skeletonize' the transformed volumes, and subsequently sort the primary and secondary PVFs based on their corresponding orientations. The routine `tbss_x` was adjusted to make it compatible with the DTI-TK transformations. Instead of the FSL routines `applywarp` and `vecreg`, DTI-TK functions `deformationScalar3DVolume` and `deformationSymTensor3DVolume` were applied, respectively. In subject space, the PVFs are still unsorted and may correspond to different fiber populations in adjacent voxels. To prevent interpolation of the PVFs of different fiber populations, similar to the original `tbss_x` routine, nearest neighbor interpolation was used to warp the PVFs to the common space. Furthermore, just as above the warped image volumes were 'skeletonized' by only retaining the voxels overlapping with the mean FA skeleton mask. Finally the skeletonized primary and secondary PVFs were analyzed.

### 4.2.12. STATISTICAL ANALYSIS OF THE REPRODUCIBILITY

To assess the reproducibility of the proposed framework and the reference frameworks, the intraclass correlation coefficient (ICC) was computed from 30 subjects who were scanned twice. Both the proposed framework and the reference frameworks were used to estimate, warp, and skeletonize the model parameters from both scans in the common space. In the proposed framework both nearest-neighbor and trilinear interpolation were used for transforming the PVFs, and the width (spread) of the orientation prior $\sigma_\theta$ was varied between 1 and 90 degrees. The orientation prior may reduce inter-subject variability while improving consistency and precision (here seen as intra-subject variability). Hence, the intraclass correlation coefficient (ICC), which balances both, was computed from 30 subjects who were scanned twice. To compute the ICC for both the primary and secondary PVFs in each skeleton voxel, a one-way random effects model was used [25].

### 4.2.13. STATISTICAL ANALYSIS OF AGEING

The proposed and reference frameworks were applied to a group of 500 subjects from the population-based Rotterdam Study [17] to study changes in diffusion measures with aging in crossing-fiber regions and to study the effect of using the proposed methodology for this study. The relevant diffusion statistics were analyzed using a conventional linear model analysis using age as the only covariate. Voxelwise statistics in TBSS were carried out using a permutation-based inference tool for nonparametric statistical thresholding (`randomise`, part of FSL). The number of permutations was set to 5000. The significance threshold was set at $p<0.05$ (employing Familywise Error Rate (FWE) correction for multiple comparisons) using the threshold-free cluster enhancement (TFCE) option in the randomise permutation-testing tool in FSL. The same statistical analysis of ageing was also applied to a random subset of 100 subjects to assess the performance when fewer data is available.

## 4.3. RESULTS

### 4.3.1. FIBER ORIENTATION ATLAS AND MODEL COMPLEXITY ATLAS

The fiber orientation atlas, constructed from 500 subjects, is visualized in figure 4.2. The first row shows the orientations of the average primary fiber population. The second row in figure 4.2 visualizes the orientation of the average secondary fiber population when present in more than 50% of the population. It can be observed that the estimated average primary and secondary fiber orientations are approximately left-right symmetric, relatively smooth, and appear anatomically plausible.

The model complexity atlas, constructed from 500 subjects, is visualized in figure 4.3. For visualization purposes, the average number of fiber populations is binned into four categories, such that regions in red, light-red, light-blue and blue reflect regions with a decreasing prevalence of crossing-fibers respectively. To obtain a discrete model complexity atlas, the average number of fiber populations was thresholded at 1.5. The blue and light-blue areas in figure 4.3 are thus regarded as single-fiber areas whereas the red and light-red regions in figure 4.3 are regarded as crossing-fiber areas. Indeed, white matter structures known to contain a single fiber population, e.g. the corpus callosum, correspond with single-fiber areas in the complexity atlas. Furthermore, the crossing-fiber voxels form clusters that are approximately left-right symmetrical. In our model complexity atlas, approximately 67 percent of the white matter skeleton consists of crossing-fiber voxels.

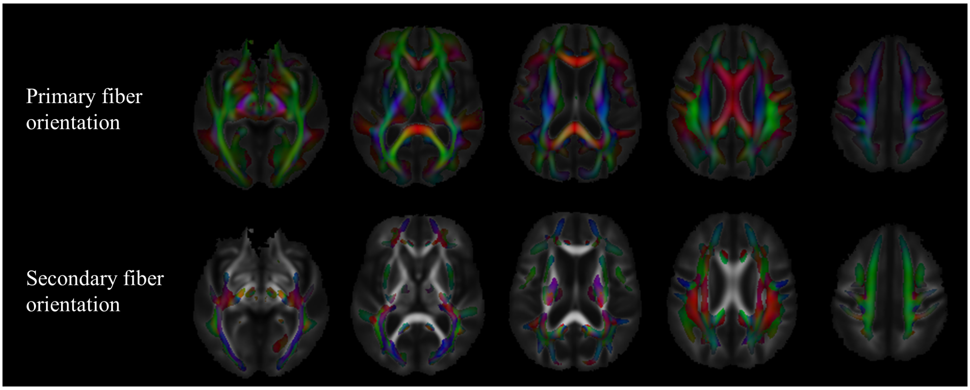

Figure 4.2: Mean fiber orientations of the primary fiber tract (top row) and secondary fiber tract, if present (bottom row). The fiber orientations modulate the background FA image, such that red corresponds with left-right, green with posterior-anterior and blue with inferior-superior.

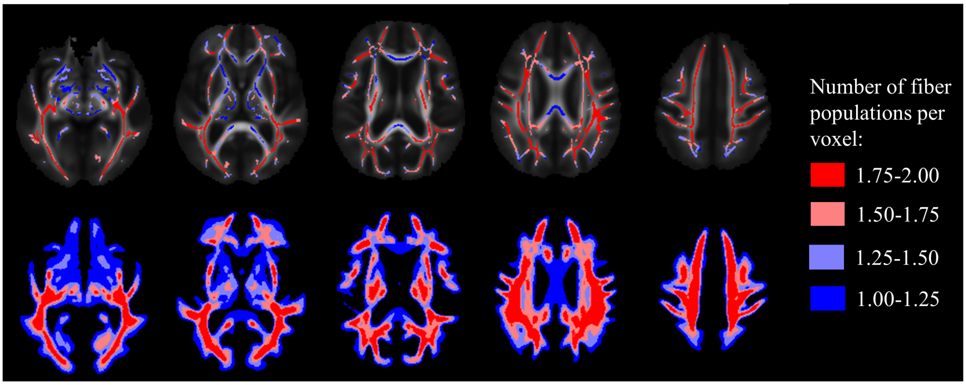

Figure 4.3: The average number of fiber populations per voxel in the common space. In the top row skeletonized data is visualized with the group-mean FA as background image. The bottom row shows the average number of fiber populations per voxel in not-skeletonized data. Voxels with (on average) fewer than 1 fiber tract are masked black.

### 4.3.2. REPRODUCIBILITY STUDY

The estimated primary and secondary fiber orientations of one subject from the reproducibility dataset are visualized in figure 4.4. The red and blue cylinders represent the stick orientations estimated from respectively the first and second scan in two regions-of-interest (ROIs). Only stick compartments with PVFs higher than the threshold of 0.05

are shown. For visualization purposes the proposed method was applied to the entire dataset (i.e. not only to the voxels on the FA skeleton). With the ARD framework (middle row of figure 4.4), the estimated stick orientations show large variation (see e.g. the green circle in ROI1), or the number of stick compartments can be different (green circle in ROI2). This would decrease the effectiveness of orientation-based labelling of fiber populations used in the second reference framework. With the proposed framework (bottom row of figure 4.4), the estimated stick orientations show less variation between the first and second scan and the number of stick compartments corresponds exactly (by definition).

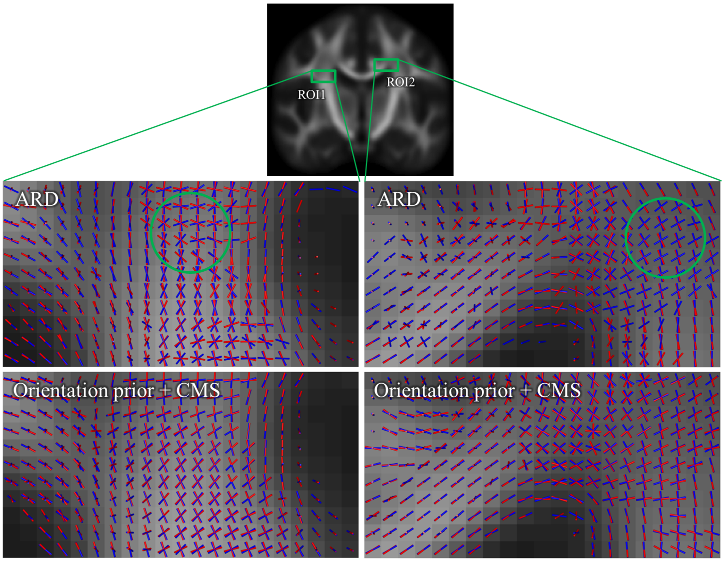

Figure 4.4: Estimated stick orientations in two regions-of-interest (ROIs) of a subject from the reproducibility dataset warped to the common space. The red and blue cylinders represent the stick orientations estimated from respectively the first scan and second scan. Both automatic relevance detection (ARD) and the proposed framework with an orientation prior ($\sigma_\theta$=25 degrees) and consistent model selection (CMS) were used to estimate the ball-and-sticks model parameters. The single tensor FA is visualized on the background for anatomical reference. When using ARD, the estimated stick orientations do not always correspond (green circle in ROI1). Furthermore, the number of stick compartments may deviate (green circle in ROI2). In the bottom row, it can be observed that the application of prior information about the orientation and number of stick compartments makes estimated stick orientations appear more similar across different datasets.

In figure 4.5 the ICC of the primary and secondary PVFs, obtained with the proposed and second reference framework, are shown. For the primary PVFs, the ICC was averaged over all skeleton voxels. For the secondary PVFs, the ICC was averaged over all crossing-fiber skeleton voxels (according to the complexity atlas). For the proposed framework, the ICC is shown for different types of interpolation and as a function of the width of the orientation prior $\sigma_\theta$. Compared to nearest-neighbour interpolation (blue line), trilinear interpolation (red line) greatly improves the ICC of both the primary and secondary PVF. Trilinear interpolation increases the ICC by improved spatial alignment, but also the smoothing effect (inherent to trilinear interpolation) is partly responsible for the increased ICC (green line).

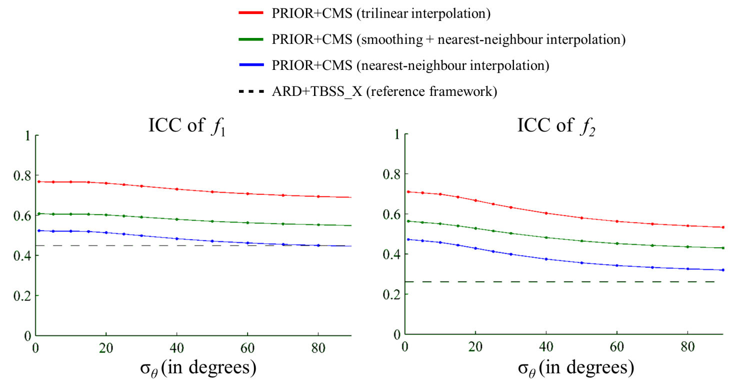

Figure 4.5: Left: average intraclass correlation coefficient (ICC) of $f_1$ on the TBSS skeleton. Right: average ICC of $f_2$ in crossings-fiber regions on the TBSS skeleton. The black dashed lines denote the ICC of the reference framework, the colored lines denote the ICC of the proposed framework using nearest-neighbour interpolation (blue), smoothing and nearest-neighbour interpolation (green) and trilinear interpolation (red).

Figure 4.5 demonstrates that a prior width $\sigma_\theta$ of 25 degrees is a good trade-off between improving the ICC without introducing too much prior information on the fiber orientations. Accordingly, the results in the remainder of this chapter were generated with this prior width in combination with trilinear interpolation. In figure 4.6 the ICC of the primary and secondary PVFs, obtained with the reference and proposed framework, are shown on the skeleton. The ICC of both the primary and secondary PVFs is significantly higher across the whole skeleton.

### 4.3.3. AGEING CORRELATIONS IN POPULATION DATA

The results of the statistical analysis of ageing are plotted in figure 4.7, figure 4.8 and figure 4.9. In figure 4.7 the regression coefficients with age and the corresponding t-statistics of both the proposed framework and the second reference framework are shown. It can be observed that the effect size is similar, but the regression coefficients obtained with the proposed framework appear more spatially-smooth (see red arrows). Furthermore, the t-statistics for the regression coefficient with age are larger when the proposed framework is used (see red arrows), indicating the regression coefficient can be determined more precisely.

More results of the statistical analysis of ageing are plotted in figure 4.8. The first two rows of images show skeleton voxels with significant negative correlations of the primary and secondary PVFs with age when only 100 subjects are included in the analysis. The bottom two rows show the results when all 500 subjects are included in the analysis. For the analysis on 500 subjects, the PVFs obtained with the reference and proposed frameworks showed very similar patterns with ageing, i.e. uniformly distributed over the brain large clusters of voxels were found in which the PVFs decreased significantly with age. Differences in the sensitivity were most apparent in the analysis on 100 subjects, e.g. see the blue arrows in figure 4.8. In the subset of 100 subjects, the percentages of

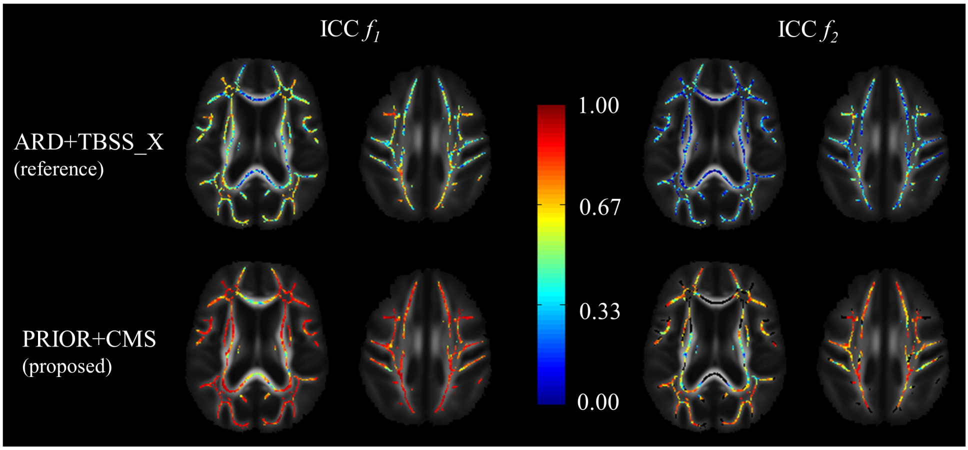

Figure 4.6: Intraclass correlation coefficient (ICC) of the primary partial volume fraction $f_1$ (left) and the secondary partial volume fraction $f_2$ (right) computed from 30 subjects for whom rescan data was available. Top row: ICC of the reference framework applying ARD and orientation-based labeling of the PVFs. Bottom row: the proposed framework applying an atlas orientation prior and CMS. Note that skeleton voxels with a single fiber population have been masked black for the secondary PVFs obtained with the proposed framework.

skeleton voxels that showed significant decrease in FA with age were 30% ($f_1$ of reference framework), 36% ($f_1$ of proposed framework), 6% ($f_2$ of reference framework) and 12% ($f_2$ of proposed framework).

In figure 4.9 correlation with age is shown for the FA generated with the first reference framework and PVFs obtained with the proposed framework in a coronal slice. FA showed a very similar pattern with ageing as the primary PVFs, i.e. large clusters of voxels across the white matter skeleton were found in which the FA decreased significantly with age. In voxels containing the corticospinal tract, however, both the FA and primary PVF did not have a significant correlation with age. However, in those voxels the secondary PVF often did significantly decrease with age.

## 4.4. DISCUSSION

In this chapter we presented a framework to improve the analysis of MR diffusion data with a ball-and-sticks model. Two novelties were introduced. The first novelty was the application of an atlas orientation prior to guarantee consistent labeling in crossing-fiber regions. The second novelty was a 'consistent model selection', obtained by determination of the number of fiber populations in a common space instead of for each subject independently. We demonstrated that the reproducibility of measuring PVFs was improved both in single fiber regions and crossing-fiber regions. Furthermore, a proof-of-principle analysis of the effect of age on white matter diffusion properties showed improved statistical power to detect age-related changes in white matter.

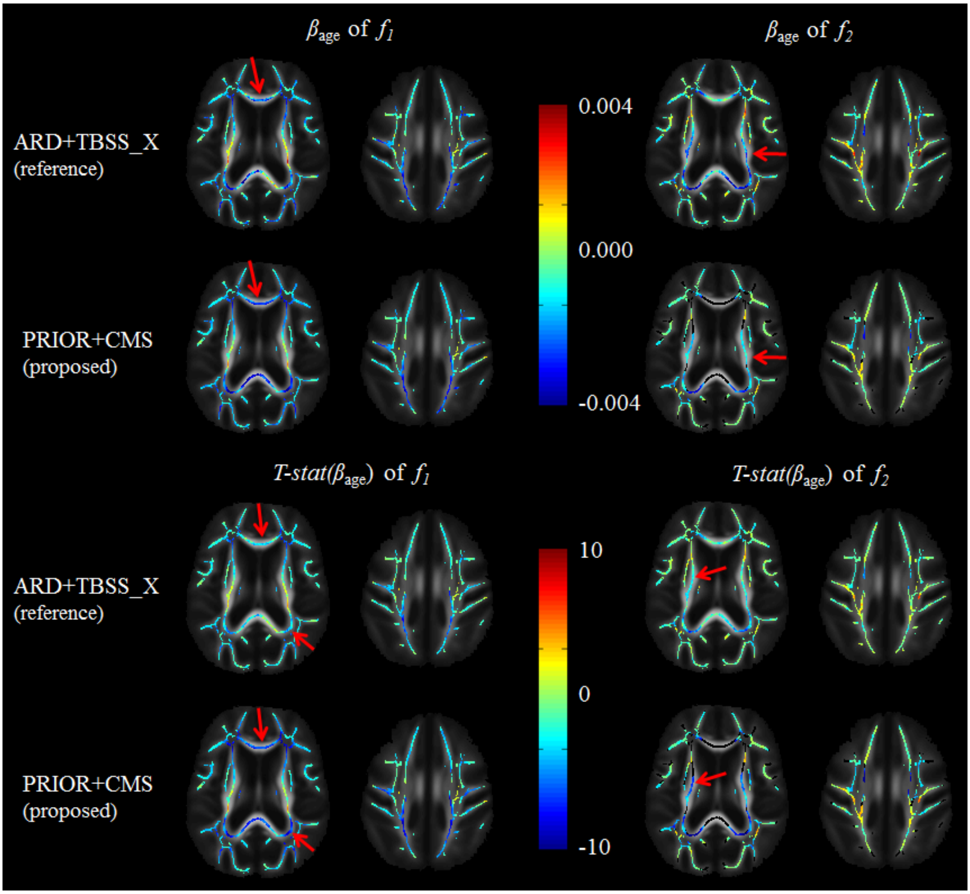

Figure 4.7: The regression coefficient and its t-statistic of the primary and secondary PVFs with age. PVFs were generated using the proposed and second reference framework. Note that skeleton voxels with a single fiber population have been masked black for the secondary PVFs obtained with the proposed framework. In the top two rows, the red arrows point at examples of regions where the proposed framework appears to provide more spatially-smooth estimates of the regression coefficient. In the bottom two rows, the red arrows point at examples of regions where the proposed framework where the t-statistic is higher.

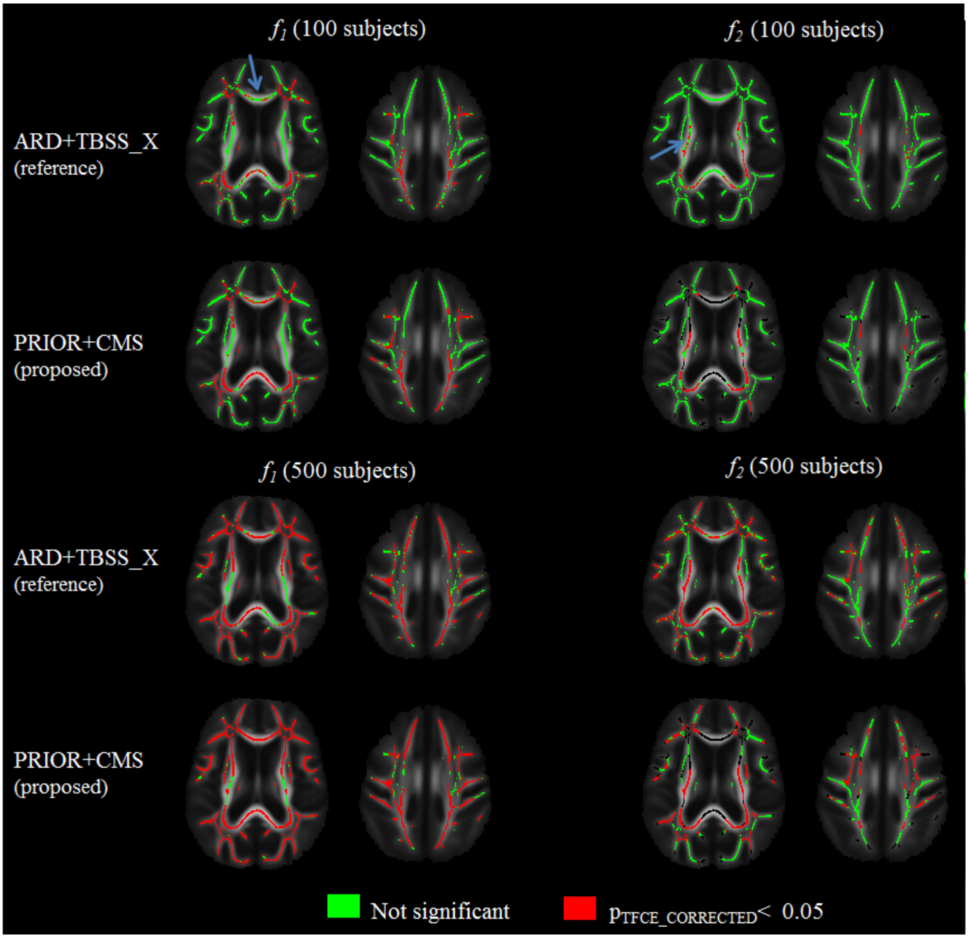

Figure 4.8: Significance of the correlation between the primary and secondary PVFs with age. PVFs were generated using the proposed and second reference framework. Note that skeleton voxels with a single fiber population have been masked black for the secondary PVF obtained with the proposed framework. The arrows point at specific regions where the outcomes of the two frameworks differ.

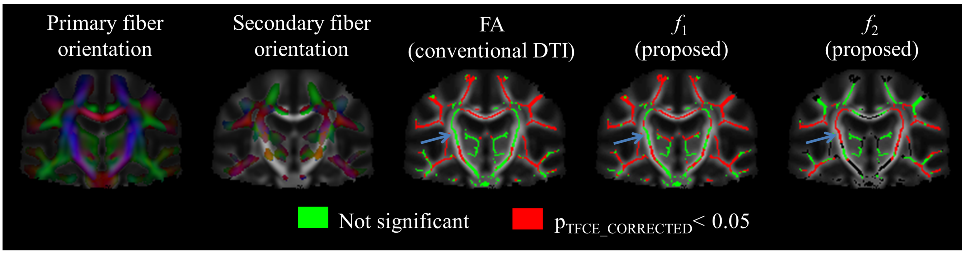

Figure 4.9: Significance of the correlation between the FA, primary and secondary PVFs with age. FA was determined by means of the first reference framework, PVFs through the proposed framework. FA and primary PVF in skeleton voxels containing the corticospinal tract (arrows) show little correlation with age, whereas the secondary PVF has a significant negative correlation with age in those voxels. From the visualization of the fiber orientations it can be deduced in that region the primary fiber population reflects the corticospinal tract, and the secondary fiber population reflects a commissural tract.

### 4.4.1. FIBER ORIENTATION ATLAS AND MODEL COMPLEXITY ATLAS

The fiber orientation atlas and the model complexity atlas were constructed using the 500 subjects from the Rotterdam Scan study. Alternatively, these atlases could have been constructed from data acquired with a more advanced DW-MRI protocol, but we deliberately did not do this. The possibility to accurately model properties of a secondary fiber population does not only depend on the anatomical presence of a fiber crossing, but also on DW-MRI acquisition parameters such as the voxel size, the signal-to-noise ratio, the number of diffusion-encoding gradient directions and the used $b$-values [11]. As a result, the constructed atlases should not only reflect the brain anatomy in our subject group, but also the DW-MRI protocol used in the acquisition. Therefore, ideally, the model complexity and fiber orientation atlas are constructed from a representative population using a similar DW-MRI protocol as the study population.

The construction of the fiber orientation atlas and model complexity atlas were both based on the ARD framework. This facilitated a comparison with the second reference framework [16] that also relies on the ARD framework for the estimation of fiber orientations and (implicit) model selection on a per-subject basis.

The discrete model complexity atlas was obtained by thresholding the average number of fiber population per voxel. The threshold value should balance between overfitting (i.e. using too many stick compartments that are not supported by the data) and under-fitting (i.e. using too few stick compartments that cannot describe the data adequately). In this chapter a threshold value of 1.5 was used to choose between fitting a ball-and-one stick model and ball-and-two sticks model. Although the choice for 1.5 was somewhat arbitrary and may be further optimized, it could still show that consistent model selection can improve the sensitivity of crossing-fiber statistics.

### 4.4.2. REPRODUCIBILITY STUDY

The first novelty, the application of an orientation prior, promoted a more consistent labelling of the fiber populations. In the proposed framework the labeling effectively takes place during estimation in subject space, such that the PVFs can be interpolated when transformed to the common space. Both the application of an orientation prior and the use of (trilinear) interpolation were shown to result in an improved ICC.

The second novelty, the determination of the number of fiber populations in a common space, was also shown to improve the ICC, particularly for measuring the secondary PVFs. This improvement might be explained by the sensitivity of ARD (or model selection in general) to noise. Since the noise realization in the first and second scan is different, this could result in a different (effective) number of anisotropic compartments in the diffusion model, especially in configurations with unbalanced volume fractions or a small angular divergence between the two fiber populations. Analyzing the 'same' voxel with a different number of anisotropic compartments in the diffusion model would increase the apparent variation in the estimated parameters. Effectively, it behaves as noise that is added onto the PVFs, which is avoided in the proposed framework by imposing a consistent model selection.

### 4.4.3. SENSITIVITY

A skeleton-based linear regression analysis between age and the relevant diffusion parameters was performed, primarily to gain insight into the sensitivity (reflected by higher t-statistics) of the framework. The proposed framework using both an orientation prior and consistent model selection appeared to be more sensitive compared to the second reference framework using ARD and orientation-based labeling of fiber populations in the common space. Particularly when using a smaller subset of 100 subjects, the number of voxels that correlated significantly with age was higher when using the proposed framework. An increased sensitivity will facilitate the detection of smaller effects, or enable the use of smaller populations while retaining similar levels of statistical significance.

### 4.4.4. AGEING

Besides gaining insight into the sensitivity of the different frameworks, the ageing study demonstrated the added value of analyzing the PVFs of ball-and-sticks models over single tensor FA. In large clusters throughout the brain it was found that FA as well as the primary PVFs in the ball-and-sticks model decreased linearly with age. This behavior of FA and PVFs is in agreement with prior work, where it was reported that FA and primary PVFs are highly correlated [16]. Even though the pattern with ageing appeared similar, it should be noted that analyses with FA and with primary PVFs are conceptually different. The FA is a scalar measurement and is not specific to a particular fiber population in a voxel, whereas the primary PVF is an orientation-dependent measurement of the primary fiber population in a voxel. This enables a population-specific analysis of the brain, or the testing of tract-specific hypotheses.

The most prominent difference between analyzing FA and PVFs was demonstrated in crossing fiber areas. We found that the FA in the corticospinal tract did not correlate significantly with age. Previous studies also reported insignificant correlations between FA and age in the corticospinal tract [26], or even reported that the FA in parts of the corticospinal tract paradoxically increased with age in elderly subjects [27]. Our model complexity atlas and fiber orientation atlas demonstrates that the corticospinal tract crosses (or is in close proximity to) many commissural and association tracts. Analysis with ball-and-sticks models revealed that the primary PVFs, with an orientation aligned to the corticospinal tract, did not correlate significantly with age. However, the secondary PVF, aligned with various commissural and association tracts, was found to decrease significantly with age. Such a selective degeneration of the secondary fiber tract may indeed result in an estimated increase in FA, and may explain the increase in FA with age observed in the corticospinal tract [27]. This underlines the importance of using improved methods to analyze crossing fiber areas.

### 4.4.5. LIMITATIONS

Inherent limitations of the proposed framework are in the use of the fiber orientation and model complexity atlas. The use of an inappropriate orientation prior during may bias the estimated diffusion statistics. In subjects with pathologies that drastically impact the white matter orientations (e.g. large brain tumors), the use of an orientation atlas may therefore not be adequate. Normal brain atrophy can be modeled by the non-rigid transformations during coregistration. Because the orientations of the fiber orientation atlas are rotated accordingly, the use of an orientation prior is still appropriate. Furthermore, the relatively wide orientation prior width of 25 degrees, also increases the generalizability of the framework.

Similarly, the use of the complexity atlas has limitations. When the complexity atlas indicates an incorrect number to be present, this may cause under-fitting or over-fitting of the data. It should be noted that over-fitting of the data is reduced by the applied orientation prior, i.e. a stick compartment not supported by the data is expected to point in the direction of the orientation prior and its estimated stick fractions will be small.

## 4.5. CONCLUSION

WE have developed a framework, that utilizes an atlas orientation prior and consistent model selection, to improve the analysis of diffusion data with a ball-and-sticks model. The application of an atlas orientation prior and the use of consistent model selection was shown to significantly improve the reproducibility and sensitivity of the ball-and-sticks model parameters in TBSS. Particularly in group studies, the proposed framework may therefore detect more subtle differences and quantify changes more precisely.

## REFERENCES

[1] E. Stejskal and J. Tanner, *Spin diffusion measurements: spin echoes in the presence of a time-dependent field gradient,* The journal of chemical physics **42**, 288 (1965).

[2] C. Beaulieu, *The basis of anisotropic water diffusion in the nervous system–a technical review,* NMR in Biomedicine **15**, 435 (2002).

[3] P. J. Basser, J. Mattiello, and D. LeBihan, *Mr diffusion tensor spectroscopy and imaging,* Biophysical journal **66**, 259 (1994).

[4] Y. Liu, G. Spulber, K. K. Lehtimäki, M. Könönen, I. Hallikainen, H. Gröhn, M. Kivipelto, M. Hallikainen, R. Vanninen, and H. Soininen, *Diffusion tensor imag-*

*ing and tract-based spatial statistics in alzheimer's disease and mild cognitive impairment,* Neurobiology of Aging **32**, 1558 (2011).

[5] M. W. Vernooij, M. de Groot, A. van der Lugt, M. A. Ikram, G. P. Krestin, A. Hofman, W. J. Niessen, and M. M. Breteler, *White matter atrophy and lesion formation explain the loss of structural integrity of white matter in aging,* Neuroimage **43**, 470 (2008).

[6] A. L. Alexander, K. M. Hasan, M. Lazar, J. S. Tsuruda, and D. L. Parker, *Analysis of partial volume effects in diffusion-tensor mri,* Magnetic Resonance in Medicine **45**, 770 (2001).

[7] D. S. Tuch, T. G. Reese, M. R. Wiegell, N. Makris, J. W. Belliveau, and V. J. Wedeen, *High angular resolution diffusion imaging reveals intravoxel white matter fiber heterogeneity,* Magnetic Resonance in Medicine **48**, 577 (2002).

[8] C. A. Wheeler-Kingshott and M. Cercignani, *About "axial" and "radial" diffusivities,* Magnetic Resonance in Medicine **61**, 1255 (2009).

[9] C. Pierpaoli, A. Barnett, S. Pajevic, R. Chen, L. Penix, A. Virta, and P. Basser, *Water diffusion changes in wallerian degeneration and their dependence on white matter architecture,* Neuroimage **13**, 1174 (2001).

[10] G. Douaud, S. Jbabdi, T. E. J. Behrens, R. A. Menke, A. Gass, A. U. Monsch, A. Rao, B. Whitcher, G. Kindlmann, P. M. Matthews, and S. Smith, *Dti measures in crossing-fibre areas: Increased diffusion anisotropy reveals early white matter alteration in mci and mild alzheimer's disease,* Neuroimage **55**, 880 (2011).

[11] T. Behrens, H. J. Berg, S. Jbabdi, M. Rushworth, and M. Woolrich, *Probabilistic diffusion tractography with multiple fibre orientations: What can we gain?* Neuroimage **34**, 144 (2007).

[12] M. Caan, G. Khedoe, D. Poot, A. den Dekker, S. Olabarriaga, K. Grimbergen, L. van Vliet, and F. Vos, *Adaptive noise filtering for accurate and precise diffusion estimation in fiber crossings,* in *Medical Image Computing and Computer-Assisted Intervention–MICCAI 2010* (Springer, 2010) pp. 167–174.

[13] Y. Assaf and P. J. Basser, *Composite hindered and restricted model of diffusion (charmed) mr imaging of the human brain,* Neuroimage **27**, 48 (2005).

[14] J. Yang, D. H. Poot, G. A. Arkesteijn, M. W. Caan, L. J. van Vliet, and F. M. Vos, *Estimating diffusion properties in complex fiber configurations based on structure-adaptive multi-valued tensor-field filtering,* in *SPIE Medical Imaging* (International Society for Optics and Photonics, 2015) pp. 941320–941320–7.

[15] S. M. Smith, M. Jenkinson, H. Johansen-Berg, D. Rueckert, T. E. Nichols, C. E. Mackay, K. E. Watkins, O. Ciccarelli, M. Z. Cader, P. M. Matthews, and T. E. J. Behrens, *Tract-based spatial statistics: Voxelwise analysis of multi-subject diffusion data,* Neuroimage **31**, 1487 (2006).

[16] S. Jbabdi, T. E. Behrens, and S. M. Smith, *Crossing fibres in tract-based spatial statistics,* Neuroimage **49**, 249 (2010).

[17] A. Hofman, G. G. Brusselle, S. D. Murad, C. M. van Duijn, O. H. Franco, A. Goedegebure, M. A. Ikram, C. C. Klaver, T. E. Nijsten, and R. P. Peeters, *The rotterdam study: 2016 objectives and design update,* European journal of epidemiology **30**, 661 (2015).

[18] M. A. Ikram, A. van der Lugt, W. J. Niessen, G. P. Krestin, P. J. Koudstaal, A. Hofman, M. M. Breteler, and M. W. Vernooij, *The rotterdam scan study: design and update up to 2012,* European Journal of Epidemiology **26**, 811 (2011).

[19] S. Klein, M. Staring, K. Murphy, M. Viergever, and J. P. Pluim, *Elastix: a toolbox for intensity-based medical image registration,* Medical Imaging, IEEE Transactions on **29**, 196 (2010).

[20] A. Leemans and D. K. Jones, *The b-matrix must be rotated when correcting for subject motion in dti data,* Magnetic Resonance in Medicine **61**, 1336 (2009).

[21] D. H. Poot and S. Klein, *Detecting statistically significant differences in quantitative mri experiments, applied to diffusion tensor imaging,* Medical Imaging, IEEE Transactions on **34**, 1164 (2015).

[22] H. Zhang, P. A. Yushkevich, D. C. Alexander, and J. C. Gee, *Deformable registration of diffusion tensor mr images with explicit orientation optimization,* Medical image analysis **10**, 764 (2006).

[23] A. Schwartzman, R. F. Dougherty, and J. E. Taylor, *Cross-subject comparison of principal diffusion direction maps,* Magnetic Resonance in Medicine **53**, 1423 (2005).

[24] M. de Groot, M. W. Vernooij, S. Klein, M. A. Ikram, F. M. Vos, S. M. Smith, W. J. Niessen, and J. L. Andersson, *Improving alignment in tract-based spatial statistics: Evaluation and optimization of image registration,* Neuroimage **76**, 400 (2013).

[25] K. O. McGraw and S. P. Wong, *Forming inferences about some intraclass correlation coefficients,* Psychological methods **1**, 30 (1996).

[26] M. E. Perry, C. R. McDonald, D. J. Hagler Jr, L. Gharapetian, J. M. Kuperman, A. K. Koyama, A. M. Dale, and L. K. McEvoy, *White matter tracts associated with set-shifting in healthy aging,* Neuropsychologia **47**, 2835 (2009).

[27] M. de Groot, L. G. Cremers, M. A. Ikram, A. Hofman, G. P. Krestin, A. van der Lugt, W. J. Niessen, and M. W. Vernooij, *White matter degeneration with aging: Longitudinal diffusion mr imaging analysis,* Radiology **279**, 532 (2015).

# 5

# LONGITUDINAL ANALYSIS OF DW-MRI WITH A BALL-AND-STICKS MODEL

*The purpose of this chapter is to increase the sensitivity in longitudinal analysis of DW-MRI data with the ball-and-sticks model. Longitudinal DW-MRI data (baseline and two follow-up scans) of 25 middle-aged subjects (47 to 61 years at base line) were acquired. After coregistering all the diffusion-weighted images (DWIs) from the baseline and follow-up scans to a subject-specific intermediate space, an extended ball-and-sticks model was fitted. Stick orientations were constrained such that they did not change over time. The stick fractions were warped and projected onto the TBSS (tract-based spatial statistics) skeleton, and were compared to a reference framework in which all scans were processed independently. Compared to the reference framework, the standard deviation of the apparent noise on the primary stick fractions on the TBSS skeleton was reduced with approximately a factor two. The use of the proposed longitudinal DW-MRI pipeline may significantly increase the precision compared to a default cross-sectional image processing pipeline.*

---

G.A.M. Arkesteijn, D.H.J. Poot, M. Niestijl, M.W. Vernooij, W.J. Niessen, L.J. van Vliet, and F.M. Vos, in *Biomedical Imaging (ISBI), 2015 IEEE 12th International Symposium on*, pp. 783-786 (2015).

## 5.1. INTRODUCTION

DIFFUSION-WEIGHTED magnetic resonance imaging (DW-MRI) is a non-invasive MRI technique that enables measurement of diffusion of water [1]. It is frequently used to assess the brain's white matter integrity, because the water diffusivity reflects the microstructural organization of neural fibers [2].

The quantitative nature of DW-MRI makes it especially suitable for longitudinal studies because it facilitates measurement of subject-specific changes in diffusion behavior. Longitudinal studies in DW-MRI have for instance been used to quantify small changes in the white matter after ischemic stroke [3], during development [4], and during normal ageing [5].

A limitation of many DW-MRI studies (e.g. [3–5]) is in the use of the conventional single tensor model. It is well known that water diffusion in white matter cannot be adequately modeled by a Gaussian, particularly in voxels containing more than one fiber tract. Therefore, diffusion descriptors computed from this model may lack sensitivity [6], or may suggest spurious change in the white matter microstructure [7, 8].

Several alternative models have been proposed to provide a more adequate description of the diffusion including the ball-and-sticks model [9], multi-tensor models [10], or CHARMED [11]. However, the number of unknown parameters is larger in these models, which hinders precise estimation.

Particularly in a longitudinal DW-MRI study it is of interest that a good precision is achieved, because the effect size is typically small. Simultaneously, however, a longitudinal study offers the opportunity to pool information across different scans of the same subject. For instance, in many DW-MRI studies it seems reasonable that the orientation of white matters does not change drastically over the time span of a few years. This would allow the estimated white matter orientations to be constrained over time. In effect this reduces the total number of unknown parameters, which could enhance the precision of parameter estimation.

The goal of this chapter is to increase the sensitivity of longitudinal DW-MRI studies using the ball-and-sticks model. The key novelty of our approach is that we coregister the DWIs from the baseline and follow-up scans from the same subject and then fit a ball-and-sticks model to all DWIs simultaneously. While doing so the stick orientations are constraint to be the same on the different time points. All other unknown ball-and-sticks parameters are estimated separately for each time point. We evaluate the proposed method with diffusion data from 25 subjects.

## 5.2. MATERIALS & METHODS

### 5.2.1. OVERVIEW OF THE PROPOSED FRAMEWORK

In figure 5.1 an overview of the proposed framework is presented. After basic preprocessing, the DWIs from the baseline and follow-up scans are coregistered to a subject-specific intermediate space. Next, an extended ball-and-sticks model is fitted to all DWIs simultaneously. In this extended ball-and-sticks model, the stick orientations are constrained across the different scans. All other unknown parameters are still estimated for each scan. In the following sections, each of these steps will be discussed in more detail.

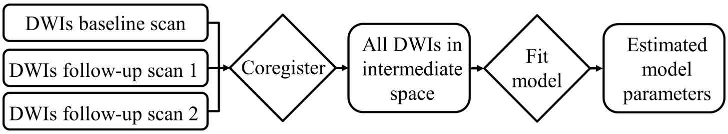

Figure 5.1: Overview of the proposed framework for fitting a diffusion model to the DWIs of a single subject.

### 5.2.2. STUDY POPULATION

The proposed framework was evaluated on 25 middle-aged subjects (47 to 61 years at base line) from the Rotterdam Study, a prospective population-based cohort study among middle-aged and elderly subjects in a district of the city of Rotterdam, the Netherlands [12]. Ethical approval was granted by the institutional review board, and written informed consent was obtained from all participants.

### 5.2.3. DATA ACQUISITION

All subjects were scanned three times on a 1.5 Tesla MRI scanner (GE Signa Excite) using an 8-channel head coil. The average time between baseline scan and last follow-up scan was 5.8 years. No major hardware or software updates were performed on the scanner throughout the study [13]. DWIs were acquired with a single shot, diffusion-weighted spin echo echo-planar imaging sequence using TR = 8575 ms, TE = 82.6 ms, FOV = 210x210 mm$^2$, imaging matrix = 96x64 (zero-padded to 256x256), yielding 35 contiguous slices with a thickness of 3.5 mm. DWIs were acquired in 25 non-collinear directions with a $b$-value of 1000 s/mm$^2$. Three volumes were acquired without diffusion-weighting (the $b_0$-volumes) [13].

### 5.2.4. PREPROCESSING

The DWIs from each baseline and follow-up scan were separately corrected for motion and eddy current distortion by affine coregistration to the $b_0$-volume using `flirt` (part of FSL [14]). After coregistration to the reference $b_0$-volume, the gradient directions were reoriented according to the rotation component of the transformation [15]. Then, a single tensor model was fitted separately to the DWI baseline and follow up-data merely to facilitate mutual coregistration.

### 5.2.5. COREGISTRATION OF DWIS

The DWIs from the baseline and both follow-up scans were transformed to a subject-specific intermediate space. While doing so, it is essential to avoid any asymmetry bias [16]. We therefore extended the approach in [5] to support three scans. An overview is presented in figure 5.2.

Let $A$, $B$ and $C$ refer to the scans at three different time points. First, based on the FA (fractional anisotropy), all pairwise (nonrigid) transformations (i.e. $T_{AB}$, $T_{BA}$, $T_{BC}$, $T_{CB}$, $T_{AC}$, $T_{CA}$) were computed using `fnirt` (part of FSL). Next, the transformation to intermediate space $M$ was computed by inverting and adding the displacement fields, e.g. $T_{AM} = \text{inv}(T_{BA})/3 + \text{inv}(T_{CA})/3$.

The affine transformations applied during preprocessing (motion end eddy current

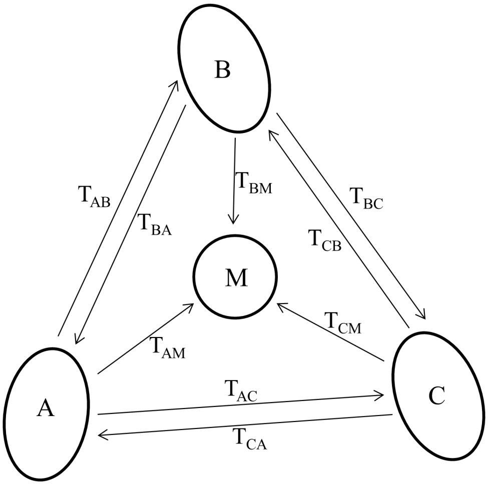

Figure 5.2: Overview of the coregistration of the DWIs from three different scans.

distortion correction) were concatenated with the nonrigid transformations to the subject-specific intermediate space, such that only a single interpolation of the DWIs was required. Simultaneously, the DWIs were upsampled to 2.0 $\text{mm}^3$ cubic resolution. After this transformation, the corresponding gradient directions were globally reoriented [15].

### 5.2.6. REFERENCE BALL-AND-STICKS MODEL

In the ball-and-sticks model [9], the diffusion-weighted signal in the $i$th DWI is modeled as follows:

$$S_{\boldsymbol{\theta},i} = S_0\left(\left(1-\sum_{j=1}^{N} f_j\right)\exp\left(-b_i d\right)+\sum_{j=1}^{N} f_j \exp\left(-b_i d\left(\mathbf{V}_j\cdot\mathbf{g}_i^T\right)^2\right)\right), \tag{5.1}$$

in which $b$ is the diffusion-weighting parameter, $\mathbf{g}$ is a unit vector that specifies the direction of a diffusion-encoding gradient pulse, $S_0$ is the non-diffusion-weighted signal, $N$ is the number of stick compartments, $d$ is a diffusivity parameter, $f_j$ represents a stick's volume fraction and $\mathbf{V}_j$ the principal eigenvector of the $j$th stick compartment.

The function `bedpostx` (part of FSL [9]) was used to fit the ball-and-sticks model with $N = 2$ stick compartments to each scan in its native space. After estimation, the stick fractions and orientations were warped to the subject-specific intermediate space, using the appropriate functions in FSL (i.e. `applywarp` and `vecreg`).

### 5.2.7. LONGITUDINAL BALL-AND-STICKS MODEL

In the longitudinal ball-and-sticks model, the diffusion-weighted signal $S_{\boldsymbol{\theta}}$ in the $i$th acquired DWI of the $k$th scan is modeled according to:

$$S_{\boldsymbol{\theta},i,k} = S_{0,k}\left(\left(1-\sum_{j=1}^{N} f_{j,k}\right)\exp\left(-b_{i,k} d_k\right)+\sum_{j=1}^{N} f_{j,k} \exp\left(-b_{i,k} d_k\left(\mathbf{V}_j\cdot\mathbf{g}_{i,k}^T\right)^2\right)\right). \tag{5.2}$$

Here, the eigenvectors $\mathbf{V}_j$ are parameterized using spherical coordinates $\psi_j$ and $\phi_j$. In case of $k = 3$ scans and $N = 2$ stick compartments, the unknown parameter vector $\boldsymbol{\theta}$ becomes $[S_{0,1}, f_{1,1}, f_{2,1}, d_1, S_{0,2}, f_{1,2}, f_{2,2}, d_2, S_{0,3}, f_{1,3}, f_{2,3}, d_3, \psi_1, \phi_1, \psi_2, \phi_2]$. Notice that now the stick direction parameters $(\psi_1, \phi_1, \psi_2, \phi_2)$ are the same for each scan $k$. A maximum likelihood estimator using a Rician noise distribution was used to estimate the unknown parameter vector in each voxel of the intermediate space [17].

### 5.2.8. TBSS ANALYSIS

The stick fractions of both the proposed (longitudinal) and reference framework were analyzed on a white matter skeleton in atlas space (FMRIB58) using TBSS (tract-based spatial statistics) [18]. The function `tbss_x` was used to warp and project the stick fractions onto a skeleton, which takes into account that partial volume fractions are not scalar measurements of diffusion but have orientations that need to be matched across subjects [19]. The ICBM-DTI-81 white matter label atlas [20] was warped to FMRIB58 space and used to label skeleton voxels, such that average stick fractions over different white matter structures could be computed.

## 5.3. EXPERIMENTS & RESULTS

In figure 5.3 one example of stick orientations estimated with the reference framework are visualized. In single fiber regions, e.g. the corpus callosum (red circle), the sticks are similarly oriented in the three different scans. In crossing-fiber regions, however, the sticks have inconsistent orientations across the three scans (blue circle).

The between-scan differences of the primary stick fractions of the same subject are primarily caused by ‘noise’. Therefore we take these between-scan differences as a measure of estimation variation. For each subject the standard deviation of the primary stick fractions f1 across the three scans is computed in the TBSS skeleton voxels. In figure 5.4 we show this standard deviation, averaged over the 25 subjects in our study. Observe that the average standard deviation of the proposed framework is only half that of the reference framework.

In figure 5.5 the average within-subject standard deviation of the mean primary stick fractions in each of the 48 white matter structures in the ICBM-DTI-81 atlas is visualized. Again it can be observed that the proposed framework yields smaller between-scan differences. Finally, as an example, we visualize the average primary stick fractions obtained with the proposed framework in the ‘Superior corona radiata R (label 25)’ in figure 5.6.

## 5.4. DISCUSSION & CONCLUSION

We have evaluated a framework to simultaneously fit the ball-and-sticks model to multiple scans of the same subject. This approach allowed the stick-orientation to be constrained over different scans, while all other parameters were estimated separately for each scan. We have limited our evaluation of the longitudinal framework to the ball-and-sticks model. More complex models of diffusion (e.g. [17] or [11]) were not supported by our DW-MRI data as they require the DWIs to be acquired with more than one non-zero $b$-value.

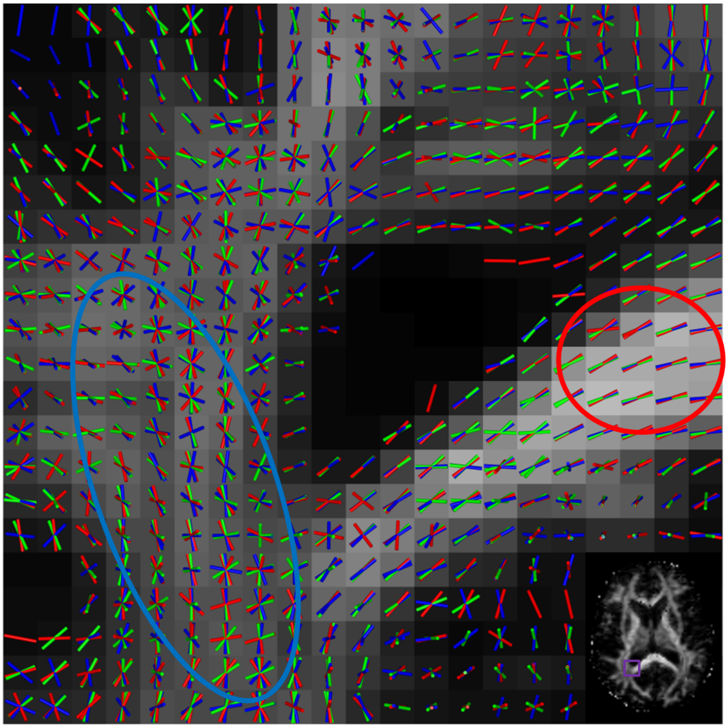

Figure 5.3: Example of stick orientations estimated from the baseline (red), the first follow-up (blue) and the second follow-up (green) scan of the same subject.

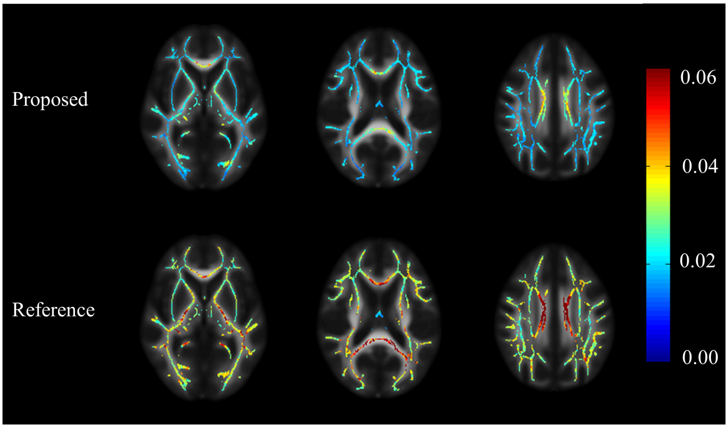

Figure 5.4: The average within-subject standard deviation of the primary stick fraction on a white matter skeleton.

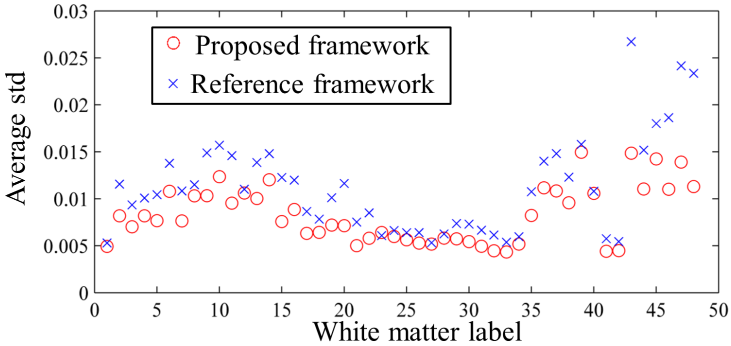

Figure 5.5: Average within-subject standard deviation of the primary stick fractions in 48 white matter structures.

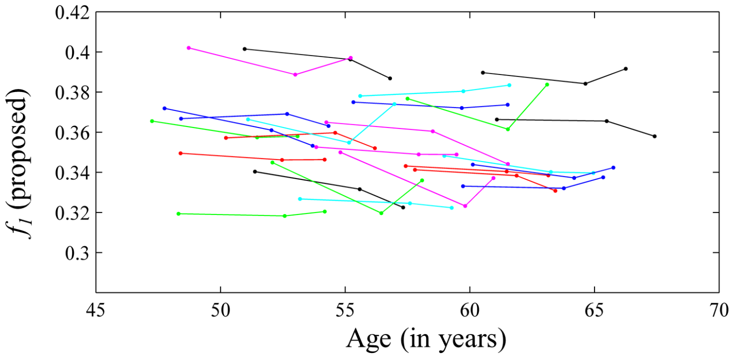

Figure 5.6: Example of primary stick fractions obtained with the proposed framework in the 'Superior corona radiata R (label 25)' versus age. Connected points represent the same subject. Lines have random colors to distinguish between different subjects.

A non-rigid transformation was used to warp the scans to a subject-specific intermediate space. We preferred this approach over an affine or rigid transformation such that shrinkage of the brain and growth of the ventricles could be represented.

The advantage of constraining the orientations across different scans can be appreciated in figure 5.3. The shown variation of the estimated stick orientations across scans simultaneously results in additional variance in the estimated stick fractions (see figure 5.4 and figure 5.5). Large fluctuations of the stick orientations across different scans may also affect the (orientation-based) labeling of the stick fractions used in `tbss_x` which will add to the variance on the skeletonized stick fractions. These are the primary reasons why the within-subject standard deviations of the stick fractions were much lower with the proposed framework.

The small within-subject fluctuations of the stick fractions suggest that the proposed framework may be more sensitive to subtle changes in the white matter, and may therefore be a promising tool in future longitudinal DW-MRI studies.

## 5.5. ACKNOWLEDGMENTS

THIS study was financially supported as part of the STW Perspectief programme Population Imaging Genetics (ImaGene) supported by the Dutch Technology Foundation (STW), project 12722.

## REFERENCES

[1] E. Stejskal and J. Tanner, *Spin diffusion measurements: spin echoes in the presence of a time-dependent field gradient,* The journal of chemical physics **42**, 288 (1965).

[2] C. Beaulieu, *The basis of anisotropic water diffusion in the nervous system–a technical review,* NMR in Biomedicine **15**, 435 (2002).

[3] C. Wang, G. T. Stebbins, D. L. Nyenhuis, L. deToledo Morrell, S. Freels, E. Gencheva, L. Pedelty, K. Sripathirathan, M. E. Moseley, D. A. Turner, J. D. E. Gabrieli, and P. B. Gorelick, *Longitudinal changes in white matter following ischemic stroke: A three-year follow-up study,* Neurobiology of Aging **27**, 1827 (2006).

[4] D. J. Simmonds, M. N. Hallquist, M. Asato, and B. Luna, *Developmental stages and sex differences of white matter and behavioral development through adolescence: A longitudinal diffusion tensor imaging (dti) study,* Neuroimage **92**, 356 (2014).

[5] M. de Groot, L. G. Cremers, M. A. Ikram, A. Hofman, G. P. Krestin, A. van der Lugt, W. J. Niessen, and M. W. Vernooij, *White matter degeneration with aging: Longitudinal diffusion mr imaging analysis,* Radiology **279**, 532 (2015).

[6] C. Pierpaoli, A. Barnett, S. Pajevic, R. Chen, L. Penix, A. Virta, and P. Basser, *Water diffusion changes in wallerian degeneration and their dependence on white matter architecture,* Neuroimage **13**, 1174 (2001).

[7] C. A. Wheeler-Kingshott and M. Cercignani, *About "axial" and "radial" diffusivities,* Magnetic Resonance in Medicine **61**, 1255 (2009).

[8] G. Douaud, S. Jbabdi, T. E. J. Behrens, R. A. Menke, A. Gass, A. U. Monsch, A. Rao, B. Whitcher, G. Kindlmann, P. M. Matthews, and S. Smith, *Dti measures in crossing-fibre areas: Increased diffusion anisotropy reveals early white matter alteration in mci and mild alzheimer's disease,* Neuroimage **55**, 880 (2011).

[9] T. Behrens, H. J. Berg, S. Jbabdi, M. Rushworth, and M. Woolrich, *Probabilistic diffusion tractography with multiple fibre orientations: What can we gain?* Neuroimage **34**, 144 (2007).

[10] M. W. Caan, H. Khedoe, D. H. Poot, A. J. den Dekker, S. D. Olabarriaga, K. A. Grimbergen, L. J. van Vliet, and F. M. Vos, *Estimation of diffusion properties in crossing fiber bundles,* Medical Imaging, IEEE Transactions on **29**, 1504 (2010).

[11] Y. Assaf and P. J. Basser, *Composite hindered and restricted model of diffusion (charmed) mr imaging of the human brain,* Neuroimage **27**, 48 (2005).

[12] A. Hofman, G. G. Brusselle, S. D. Murad, C. M. van Duijn, O. H. Franco, A. Goedegebure, M. A. Ikram, C. C. Klaver, T. E. Nijsten, and R. P. Peeters, *The rotterdam study: 2016 objectives and design update,* European journal of epidemiology **30**, 661 (2015).

[13] M. A. Ikram, A. van der Lugt, W. J. Niessen, G. P. Krestin, P. J. Koudstaal, A. Hofman, M. M. Breteler, and M. W. Vernooij, *The rotterdam scan study: design and update up to 2012,* European Journal of Epidemiology **26**, 811 (2011).

[14] M. Jenkinson and S. Smith, *A global optimisation method for robust affine registration of brain images,* Medical image analysis **5**, 143 (2001).

[15] A. Leemans and D. K. Jones, *The b-matrix must be rotated when correcting for subject motion in dti data,* Magnetic Resonance in Medicine **61**, 1336 (2009).

[16] M. Reuter and B. Fischl, *Avoiding asymmetry-induced bias in longitudinal image processing,* Neuroimage **57**, 19 (2011).

[17] M. Caan, G. Khedoe, D. Poot, A. den Dekker, S. Olabarriaga, K. Grimbergen, L. van Vliet, and F. Vos, *Adaptive noise filtering for accurate and precise diffusion estimation in fiber crossings,* in *Medical Image Computing and Computer-Assisted Intervention–MICCAI 2010* (Springer, 2010) pp. 167–174.

[18] S. M. Smith, M. Jenkinson, H. Johansen-Berg, D. Rueckert, T. E. Nichols, C. E. Mackay, K. E. Watkins, O. Ciccarelli, M. Z. Cader, P. M. Matthews, and T. E. J. Behrens, *Tract-based spatial statistics: Voxelwise analysis of multi-subject diffusion data,* Neuroimage **31**, 1487 (2006).

[19] S. Jbabdi, T. E. Behrens, and S. M. Smith, *Crossing fibres in tract-based spatial statistics,* Neuroimage **49**, 249 (2010).

[20] S. Mori, K. Oishi, H. Jiang, L. Jiang, X. Li, K. Akhter, K. Hua, A. V. Faria, A. Mahmood, R. Woods, A. W. Toga, G. B. Pike, P. R. Neto, A. Evans, J. Zhang, H. Huang, M. I. Miller, P. van Zijl, and J. Mazziotta, *Stereotaxic white matter atlas based on diffusion tensor imaging in an icbm template,* Neuroimage **40**, 570 (2008).

# 6

# CONCLUSION & FUTURE RESEARCH

## 6.1. CONCLUSION

THE objectives of this thesis were (1) to enhance our insight in the relation between the tissue structure and the DW-MRI signal, and (2) to develop methods to quantify diffusion properties as accurately and precisely as possible based on conventional DW-MRI data. More specifically, we investigated how to analyze brain regions susceptible to partial volume effects with the CSF, how to best analyze brain regions with crossing fiber-regions, and how longitudinal DW-MRI can be leveraged to increase the precision of computed diffusion statistics.

### 6.1.1. RELATION BETWEEN TISSUE STRUCTURE AND THE DW-MRI SIGNAL

In chapter 2, the accuracy of Monte Carlo simulations of the DW-MRI signal was investigated in comparison to measurements of a hardware phantom.

The hardware phantom consisted of solid fibers with varying packing density. As such it acted as a model for the extra-axonal diffusion. In the Monte Carlo experiments, the DW-MRI signal was computed by simulating diffusion outside randomly packed cylinders with varying fiber packing density. The Monte Carlo simulations of the DW-MRI signal were shown to be in good agreement with experimental data from the hardware phantom up to fiber packing fractions of 0.65.

Two limitations of the hardware fiber phantom were studied: the absence of intra-axonal diffusion and the relatively large diameter of the used fibers.

Simulation of the intra-axonal diffusion showed that there is almost zero attenuation of the radial DW-MRI signal originating from spins inside axons with diameters smaller than 8 μm at $b$-values smaller than 5000 $\mathrm{s/mm^2}$. This supports common approaches to model intra-axonal diffusion with stick compartments, e.g. the ball-and-sticks model [1] or NODDI [2].

Furthermore, the Monte Carlo simulation experiments showed that the diffusion-weighted MRI signal from the extra-cylindrical space does not depend on the cylinder diameter for $b$-values smaller than approximately 1500 $\mathrm{s/mm^2}$. For $b$-values larger than 1500 s/mm$^2$, particularly in substrates containing cylinders with relatively large diameters, the attenuation of the signal was non-mono-exponential. In substrates with small cylinder diameters (4 μm or smaller), the attenuation curve appeared to be mono-exponential. This suggests that in actual white matter with typical axon diameters of 0.1 μm to 2 μm [3], hindered extracellular diffusion is indeed well modeled by a (3D) Gaussian distribution.

In conclusion, the Monte Carlo diffusion simulations accurately match the experimental data from the hardware phantom. Therefore, the combination of Monte Carlo simulations and a hardware diffusion phantom may allow studying the complex link between the DW-MRI signal and the underlying microstructure.

### 6.1.2. PARTIAL VOLUME EFFECTS WITH CSF

In chapter 3, we have investigated the computation of 'CSF contamination-invariant statistics' from conventional DW-MRI data. These statistics were expected to be more robust to partial volume effects with the CSF than conventional diffusion statistics, and were obtained by fitting a constrained bi-tensor model to the data.

Particularly, we studied a bi-tensor model in which either the MD or the AxD of the tensor compartment was constrained to a subject-specific value. These subject-specific values were computed from the median MD or AxD of a single tensor fit in the splenium of the corpus callosum. In simulations the mean FA estimated by these bi-tensor models did not depend on macrostructural properties, which suggested that the proposed diffusion statistics are indeed CSF contamination-invariant. Diffusion parameters such as the bi-tensor tissue fractions or the single tensor FA or MD were not CSF contamination-invariant. The bias in these diffusion statistics depended on macrostructural properties such as the diameter of a white matter structure.

Application of the proposed statistics to the fornix in an ageing study may indicate microstructural change in the body of the fornix with age. However, this change was not significantly different from the microstructural change occurring in the splenium of the corpus callosum.

In conclusion, CSF contamination-invariant statistics can allow a more sophisticated analysis in future studies of white matter structures in close vicinity of the CSF such as the fornix, particularly when the discrimination between microstructural and macrostructural changes is of interest. A limitation of the proposed statistics remains in the constraints that need to be imposed on the bi-tensor model.

### 6.1.3. ANALYSIS OF CROSSING-FIBER REGIONS

Conventional DW-MRI data consisting of a small number of diffusion-weighted images at a single non-zero *b*-value yield a high variance of the estimated parameters when crossing-fiber models are used.

In chapter 4, we presented a framework containing two novelties to overcome the aforementioned drawback and improve the analysis of conventional DW-MRI data with a ball-and-sticks model. The first novelty was the application of an atlas orientation prior to promote consistent labelling in crossing-fiber regions. The second novelty was the determination of the number of fiber populations in a common space instead of subject specific.

We demonstrated that the reproducibility of measuring partial volume fractions was improved both in single fiber regions and crossing-fiber regions. Furthermore, a proof-of-principle analysis of the effect of age on white matter diffusion properties showed improved statistical power to detect age-related changes in white matter. Particularly in cross-sectional group studies, this framework has the potential of detecting more subtle differences and quantify changes more precisely than existing approaches.

### 6.1.4. LEVERAGING LONGITUDINAL DW-MRI DATA

In chapter 5, we presented an approach to improve the analysis of longitudinal DW-MRI data with the ball-and-sticks model. We adopted an approach in which simultaneously the ball-and-sticks model is fit to multiple scans of the same subject. The stick-orientation was constrained over different scans, while all other parameters were estimated separately for each scan.

Experiments showed that constraining the orientations across different scans resulted in a much smaller within-subject fluctuations compared to fitting the ball-and-sticks model to each scan individually. The small within-subject fluctuations of the stick fractions suggest that the proposed technique is more sensitive to subtle changes in the white matter. Therefore, it may be a promising tool in future longitudinal DW-MRI studies.

## 6.2. FUTURE RESEARCH

### 6.2.1. EXTENSIONS OF THE METHODS DEVELOPED IN THIS THESIS

The methods proposed in this thesis were primarily validated by studying the reproducibility of statistics and their correlation with age. In the near future, we plan a more comprehensive validation by using data of subjects scanned with both conventional DW-MRI protocols and more advanced DW-MRI protocols. Furthermore, the value of the proposed methods in the context of pathologies is of interest and left to future research.

The techniques we developed in this thesis to improve the analysis of conventional DW-MRI with the ball-and-sticks model, can in future research be applied to more advanced crossing-fiber models and higher quality DW-MRI data. In higher quality DW-MRI data, the variance of the estimated parameters of more sophisticated crossing-fiber models may still be problematic because more unknown parameters need to be estimated. The techniques introduced in chapter 4 and 5 (e.g. priors and constraints) can be used to reduce the variance in respectively cross-sectional and longitudinal DW-MRI studies.

### 6.2.2. DIFFUSION IMAGE COREGISTRATION

Even though sophisticated diffusion models are becoming more popular, coregistration of estimated diffusion statistics in a group study often still relies on single tensor information (e.g. the FA or the full tensor information). Future research may focus on coregistration based on the full information of sophisticated diffusion models. For multi-tensor models, such an approach was shown to yield more accurate coregistration [4]. Accurate coregistration is particularly relevant for analyses of diffusion statistics conducted in a common space.

### 6.2.3. QUANTITATIVE DIFFUSION STATISTICS

Most diffusion statistics are semi-quantitative. This means that on the same scanner with the same DW-MRI protocol diffusion statistics are reasonably reproducible, but a bias may be observed when the same subject is scanned on a different scanner or with a different DW-MRI protocol. Future research may focus on developing truly quantitative diffusion statistics that are relatively independent of the particular scanner and DW-MRI protocol, or alternatively investigate how a potential bias between scanners and protocols is best modeled.

To gain insight into the differences of diffusion statistics estimated from data acquired on different MRI scanners with different DW-MRI protocols, we recently acquired DW-MRI data of the same subjects on different MRI scanners (i.e. 1.5 Tesla, 3.0 Tesla and 7.0 Tesla MRI scanners) using different DW-MRI protocols. The analysis of this dataset is left to future research, but may provide insight into the dependence of estimated diffusion statistics on magnetic field strength, image resolution, or diffusion gradient strength and timings. Such insight is relevant in multi-center studies, or when subject data is compared to reference data acquired on a different scanner or with a different DW-MRI protocol.

## REFERENCES

[1] T. Behrens, H. J. Berg, S. Jbabdi, M. Rushworth, and M. Woolrich, *Probabilistic diffusion tractography with multiple fibre orientations: What can we gain?* Neuroimage **34**, 144 (2007).

[2] H. Zhang, T. Schneider, C. A. Wheeler-Kingshott, and D. C. Alexander, *Noddi: practical in vivo neurite orientation dispersion and density imaging of the human brain,* Neuroimage **61**, 1000 (2012).

[3] F. Aboitiz, A. B. Scheibel, R. S. Fisher, and E. Zaidel, *Fiber composition of the human corpus callosum,* Brain Research **598**, 143 (1992).

[4] M. Taquet, B. Scherrer, O. Commowick, J. M. Peters, M. Sahin, B. Macq, and S. K. Warfield, *A mathematical framework for the registration and analysis of multi-fascicle models for population studies of the brain microstructure,* Medical Imaging, IEEE Transactions on **33**, 504 (2014).

# List of Publications

- **Arkesteijn, Georgius A M**, Dirk H J Poot, Marius de Groot, Meike W Vernooij, Wiro J Niessen, Lucas J van Vliet, and Frans M Vos, ’CSF contamination-invariant statistics in conventional diffusion-weighted MRI of the fornix’, *Biomedical Physics & Engineering Express* (2017), **3** 067003.

- **Arkesteijn, Georgius A M**, Dirk H J Poot, Milan Niestijl, Meike W Vernooij, Wiro J Niessen, Lucas J van Vliet, and Frans M Vos, ’Longitudinal analysis of diffusion-weighted MRI with a ball-and-sticks model’, In *IEEE 12th International Symposium on Biomedical Imaging (ISBI)* 2017, pp. 783-786.

- Yang, Jianfei, Dirk H J Poot, **Georgius A M Arkesteijn**, Matthan W Caan, Lucas J van Vliet, and Frans M Vos. ’Estimating diffusion properties in complex fiber configurations based on structure-adaptive multi-valued tensor-field filtering’, In *SPIE Medical Imaging International Society for Optics and Photonics* 2015, pp. 941320-941320.

- **Arkesteijn, Georgius A M**, Dirk H J Poot, Marius de Groot, Meike W Vernooij, Wiro J Niessen, Lucas J van Vliet, and Frans M Vos. ’CSF contamination-invariant statistics in diffusion-weighted MRI’, In *IEEE 12th International Symposium on Biomedical Imaging (ISBI)* 2015, pp. 454-457.

# DANKWOORD

Fantastisch, het proefschrift is nu echt af. Nu het einde in zicht is, heb ik uiteraard een gevoel van blijheid en opluchting. Maar deels vind ik het ook ontzettend jammer dat er een einde komt aan een periode waarvan ik ontzettend heb genoten. Het schrijven van een proefschrift kan alleen met de steun en inzet van vele anderen om mij heen, en die wil ik hier in het laatste deel van mijn proefschrift graag hiervoor bedanken.

Waar vele promovendi genoegen moeten nemen met één of misschien twee begeleiders, had ik het voorrecht gesteund te worden door een compleet team van begeleiders. Frans, halverwege mijn masteronderzoek maakte jij mij al enthousiast om als promovendus te beginnen. Je zag toen waarschijnlijk kwaliteiten in mij die ik zelf nog niet helemaal zag. Het vertrouwen en de vrijheden die jij mij hebt gegeven, maken het doen van onderzoek gewoon ontzettend leuk. Lucas, zowel jouw kritische blik, alsmede het vermogen om uit enkele woorden al te begrijpen wat ik precies bedoel, zorgden ervoor dat er gedurende elke voortgangsbespreking ook daadwerkelijk een beetje voortgang werd geboekt. Wiro, jouw ontzettende enthousiaste houding werkt aanstekelijk en je hield mij altijd scherp over wat een volgende stap moet zijn in het onderzoek. Meike, jouw klinische en medische expertise waren essentieel voor het onderzoek. Fantastisch hoe je altijd meedacht over mogelijkheden om de relevantie van mijn onderzoek te vergroten. Dirk, je bent een wandelende encyclopedie over alles wat ook maar iets met MRI, Matlab, optimalisaties of ruisdistributies te maken heeft. Het was ontzettend fijn dat ik altijd even kon binnenlopen, als ik ergens zelf niet uit kwam. Marius, bedankt voor alle hulp. Zeker in het begin was dat van grote waarde om gelijk goed van start te gaan.

Matthan, bedankt voor al jouw hulp en regelwerk bij het scannen van zowel het hardware fantoom als de vrijwilligers. Farida and Ezequiel, thank you for letting us borrow such a wonderful diffusion hardware phantom. 'Mijn' Bachelor en Master studenten Ruben, Jelle, Cristina, Milan, Richard en Karin, bedankt voor jullie enthousiaste instelling gedurende jullie onderzoek en zoals jullie zien heeft dat direct danwel indirect bijgedragen aan dit proefschrift. En ook de STW gebruikerscommissie, scanmedewerkers en vrijwilligers, wil ik bij deze graag bedanken voor de tijd en moeite die zij in mijn onderzoek hebben gestoken.

Alle (oud) collega's en (oud) studenten uit de QI-groep, bedankt voor de geweldige open sfeer waarin ik mijn onderzoek heb kunnen doen, en natuurlijk voor alle C++, T++ en vermakelijk discussies tijdens de vele koffiepauzes. Jianfei, Lena en Willem, ik vond het ontzettend leuk om ook de voortgang van jullie onderzoek te zien tijdens de vele gezamelijke werkbesprekingen van 'team brein'. Ook de jaarlijkse onuitputtelijke voorraad kruidnoten van Wim, de KOFFIE van Ronald, en de uitjes en activeiten geregeld door Mandy en Annelies droegen bij aan deze goede groepssfeer en zullen mij voorlopig nog even bijblijven. Ook wil ik graag de resterende collega's van de QI-groep hier nog expliciet bedanken voor de mooie tijd: Tian, Juan Pedro, Anna, Rasmus, Jos, Boling, Gyllion, Christiaan, Jelle H, Hamidreza, Jeroen H, Yan, Leon, Babak, Tom, Kedir, Ganesh, Thijs, Robiel, Mojtaba, Jelena, Robert N, Lennard, Milos, Nadya, Jeroen S, Richard, Mohammed, Ted, Pierre, Robert M, Jelle S, Ron, Piet, Bernd, Jeroen K, Jaap, en Sjoerd. Ook aan alle collega's bij BIGR, bedankt voor alle input en gezelligheid tijdens de vele misere en/of structure-function vergaderingen in Rotterdam.

En volgens traditie, heb ik belangrijkste tot het laatst bewaard. Familie en vrienden, bedankt voor jullie steun. Lieve pap en mam, bedankt dat jullie altijd voor mij klaarstaan en dat ik thuis altijd welkom ben voor de nodige afleiding van mijn onderzoek. Xiaoxiao, thank you for your patience throughout my PhD and making my life more colorful, I am looking forward to start a new adventure with you.

# ABOUT THE AUTHOR

## Georgius Augustinus Maria ARKESTEIJN

Joor Arkesteijn was born in Pijnacker, The Netherlands, on 23 August 1988. In 2006, he obtained his Gymnasium diploma from the Sint-Maartenscollege in Voorburg and continued to study Applied Physics at Delft University of Technology. He obtained his BSc degree in Applied Physics in 2010 and his MSc degree in Applied Physics in 2013.

In 2013, he started as a PhD-student in the Quantitative Imaging group of Delft University of Technology and in the Biomedical Imaging Group of Erasmus MC in Rotterdam. His project was part of the Imaging Genetics (ImaGene) project of the Dutch technology foundation (STW), part of the Netherlands Organisation for Scientific Research (NWO). In his research he focused on the analysis of diffusion-weighted MRI data.